SCATTER CORRECTION AND 4D RECONSTRUCTION OF CONE BEAM COMPUTED

TOMOGRAPHY (CBCT) WITH A MOVING BLOCKER

by

CONG ZHAO

DISSERTATION

Submitted in partial fulfillment of the requirements

for the degree of Doctor of Philosophy at

The University of Texas at Arlington

August, 2018

Arlington, Texas

Supervising Committee:

Mingwu Jin, Supervising Professor
Jing Wang
Qiming Zhang
Wei Chen
Yujie Chi

Acknowledgements

I would first like to thank Dr. Mingwu Jin for his support, guidance and encouragement in carrying out this dissertation work. He has been supportive and has given me many insightful suggestions about the research.

I also thank the rest of my committee members Dr. Jing Wang, Dr. Qiming Zhang, Dr. Wei Chen and Dr. Yujie Chi for their time and help.

My thanks also go to my collaborators, Luo Ouyang, Yuncheng Zhong, Xi Chen, Xinhui Duan, You Zhang and Xiaokun Huang at University of Texas Southwestern Medical Center. It has been great to work together with them.

August 3rd, 2018

Abstract

SCATTER CORRECTION AND 4D RECONSTRUCTION OF CONE BEAM COMPUTED

TOMOGRAPHY (CBCT) WITH A MOVING BLOCKER

Cong Zhao, PhD

The University of Texas at Arlington, 2018

Supervising Professor: Mingwu Jin

Come-beam computed tomography (CBCT) is being widely used as an image guidance tool in radiation therapy nowadays. The quality of CBCT image is important to localize and delineate the tumor and to define relevant volumes when the patient is in the treatment position. However, there are several factors that can deteriorate the image quality of CBCT. The large amount of scatter signal due to the use of the flat panel detector (FPD) is a major factor and greatly degrades the quality of reconstruction images. Another major factor is the respiratory motion of the patient, which can cause severe motion blurring artifacts. Although four dimensional (4D) CBCT has been developed to reduce the motion artifacts, it increases the radiation dose in order to get satisfactory reconstruction images as the conventional phase-by-phase reconstruction for 4D CBCT requires more projection data than 3D CBCT. In this dissertation, we propose some methods to address these problems.

After the brief introduction of CBCT, the factors that deteriorate the CBCT image quality and the existing studies are reviewed. Next, the moving blocker scatter correction method for CBCT is introduced and its optimization using different deconvolution methods is investigated through a simulation study and a slanted-edge experimental study. A robust moving blocker scatter correction method is further developed, which

uses multiple adjacent projection views to estimate a more accurate scatter distribution. Finally, 4D CBCT with a moving blocker is developed for simultaneous dose reduction and scatter correction. The effectiveness of the proposed scatter correction and 4D reconstruction methods is demonstrated either by simulations of digital phantoms or real phantom and clinical CBCT data.

Table of Contents

List of Illustrations

List of Tables

Chapter 1

Introduction

1.1 Scatter correction for CBCT

Cone beam computed tomography (CBCT) has been widely used in radiation therapy for direct visualization of the target and relevant volume when the patient in the treatment position [1]. However, huge amount of scatter signal can reach the flat panel detector (FPD) and greatly reduce the image quality of CBCT. The shading artifacts caused by scatter contamination lead to decreased image contrast and inaccurate CT number, where the former makes it difficult to contour the target and organs at risk and the latter will result in inaccurate dose calculation. Therefore, scatter correction (SC) is critically important to overcome these problems of CBCT for more effective adaptive radiation therapy.

Various strategies have been investigated to correct the scatter signal in CBCT projection data, e.g. suppression of scatter signal during the acquisition using anti-scatter grids [2] and correction of scatter signal in projections using computational methods [3, 4]. There have been growing interests in developing measurement based scatter correction, such as blocker-based methods [5-11] because these methods derive the scatter signal from the attenuator-blocked regions within the projection data and do not suffer the computational intense of Monte Carlo simulation [3] or the inability of analytical methods for complex/heterogeneous structures [4]. The moving blocker methods [10, 11] overcome the limitations of previous developments, such as requirement of additional measurements and the reduced imaging volume etc., and are able to simultaneously estimate the scatter signal and reconstruct the entire volume within the field of view (FOV) from a single CBCT scan. The blocker-based SC methods are founded on the assumption that the signal in the blocked region on the FPD is purely scatter, at least for

12

the central part. However, this assumption is rarely satisfied for narrow lead strips in reality due to the signals spread from unblocked region. Thus, in practice, the width of blocked region to extract scatter signal has to be meticulously chosen to achieve satisfying SC results and the extracted signals often need to be carefully scaled to avoid under- or over-correction. These empirically adjustments will prevent this promising SC method from bringing real benefit for cancer patients.

1.2 4D CBCT

Four dimensional (4D) CBCT has been developed for imaging and modeling of patient's respiratory motion in radiation therapy [12-14]. It holds a great potential for a tumor motion-of-the-day model right before each treatment fraction for a precise image-guided radiotherapy (IGRT) of lung cancer. Cone beam CT dose index (CBDI) is usually used to measure imaging dose with CTDI phantoms. The CBDI for each CBCT scan ranges from several mGy to several tens mGy, depending on difffernt body parts [15]. Since there are many fractions along a treamtment course, the accumulated imaging dose from repeated CBCT scans beomes detrimental to healthy organs. Furthermoe, in order to obtain the similar image quality with 3D CBCT, 4D CBCT needs more exposure time to acquire more projections to assure the image quality if the conventional phase-by-phase 3D reconstruction methods, such as the Feldkamp Davis Kress (FDK) algorithm and simultaneous algebraic reconstruction technique (SART) with total variation (TV) minimization [16-19], were used. This dramatically increased radiation dose limits clinical application of 4D CBCT. Besides, the accuracy of the motion model (DVFs) of the 4D CBCT is limited by the phase-by-phase reconstruction [20]. Therefore, to acquire projections similar to 3D CBCT and to obtain more accurate DVFs are primary goals for 4D CBCT.

There are various strategies developed to improve the image quality of 4D CBCT using the same number of projections as in a 3D CBCT scan. The projections are binned into different phases by using motion tracking devices or data-driven methods. One way is to reconstruct a prior image from all the projections to obtain a high quality image for the static part and to update the motion part using the difference of the projections between the forward projection of prior images and the measured projections for each phase [22-25]. Another way is to combine the reconstruction and the motion estimation by iteratively updating two parts [21, 26, 27]. Over the years, new strategies have been developed to improve 4D CBCT. Some of them aimed to optimize the regularization terms [16-18], while others focused on new motion estimation methods [28-30]. We previously developed a simultaneous motion estimation and image reconstruction (SMEIR) method that utilizes all the projections for reconstruction with alternated motion estimation [21], to get high quality images and accurate motion fields. However, the moving blocker based method has not been investigated for 4D CBCT, despect that it holds the great potential for simultaneous dose reduction and scatter correction due to the partially blocked incident X-rays.

1.3 Outlook of the proposed methods to address aforementioned issues

In this dissertation, we propose several strategies for scatter correction and motion correction of 3D and 4D CBCT. We first introduce the moving blocker scatter correction method for 3D CBCT. Then we model the signal in blocked regions as convolution of the ideal scatter signal and a point spread function (as a combined effect of penumbra and veiling glare) and propose a blind convolution method to recover the true scatter signal. The proposed method is tested using the Catphan600 phantom. We next develop a robust moving blocker scatter correction method, which use scatter signals from multiple adjacent projection views to derive a more accurate scatter

distribution. Finally, we propose to use a moving blocker for 4D CBCT data acquisition with the aim of simultaneous dose reduction and scatter correction. A joint 4D spatiotemporal reconstruction method is used to solve the challenging reconstruction problem with severely incomplete projection data for each respiratory phase.

Chapter 2

Blocker-based scatter correction for CBCT

2.1 Introduction

CBCT technology has been a very important modality in the field of medical imaging over the last few years. CBCT provides additional information that the traditional X-ray radiography cannot provide. These kinds of information are helpful in radiotherapy treatment procedures. CBCT has several advantages: (1) The 3D image can provide more accurate anatomical information, especially the location of certain tissues; (2) radiation exposure to the patient is up to 10 times less than diagnostic fan-beam CT (FBCT); (3) much bigger field of view (yet slower scan time than FBCT); (4) lower cost than FBCT. However, the scatter contamination in CBCT decreases the reconstruction image quality by introducing artifacts and causing errors for CT numbers. The scatter signal has a 2D distribution and only a small portion can be received by FBCT because of the use of 1D detector arrays. In contrast, CBCT receives most of the scatter signal because of the use of 2D detector arrays.

Scatter contamination is one of the major sources of degradation of CBCT images. It degrades image quality by decreasing the contrast, introducing shading artifacts and causing inaccuracies in the reconstructed CT number. The degraded image makes it difficult to delineate the low-contrast soft tissues, and inaccurate CT number makes the dose calculation of adaptive therapy inaccurate [31-33]. Therefore, scatter correction is very important in CBCT imaging.

There are many methods that have been investigated to correct scatter contamination in CBCT, including suppression of scatter signal during the acquisition of projection data using anti-scatter grids and increasing the air gap [2, 34-39], and correction of scatter signal in projections using computational methods or special scanning protocols [40-55]. The low frequency distribution feature of the scatter signal [56, 57] makes it possible to use blockers to

estimate the scatter. Among scatter correction (SC) techniques, blocker-based methods derive the scatter signal from the blocked regions within the projection data [49-55] and do not suffer the computational intense of Monte Carlo simulation [40-43] or the inability of analytical methods for complex or heterogeneous structures [44-48]. However, the static blocker-based methods have some limitations, such as the requirement of additional measurements for each projection view [49, 54], the reduced imaging volume corresponding to the blocked region [50, 55], or the inaccuracy caused by the interpolation of primary signal in the blocked regions [53, 58]. The recent development by keeping the blocker moving during gantry rotation [10, 11] overcomes these limitations and is able to simultaneously estimate the scatter signal and reconstruct the entire volume within the field of view (FOV) from a single CBCT scan. Compared to the primary modulation method [51, 59, 60], not only the lead strip blockers are low-cost and easy to make, but also the radiation dose can be significantly reduced since about half of the incident x-ray intensity is blocked by moving blockers and statistical compressed sensing reconstruction can compensate for sparse view projections and elevated noise due to scatter subtraction.

In this study, we first investigated the moving blocker method [10, 11]. The detected signal in the blocked regions is assumed to be the scatter signal. The scatter signal in the unblocked regions was obtained by interpolating the detected signal from the blocked regions. Then the primary signal was obtained by subtracting the interpolated scatter signal from the signal in the unblocked regions. To avoid the inaccuracy caused by the interpolation of primary signal, only the primary signal in the unblocked regions was used to reconstruct the 3D image. Some improvements of CBCT reconstruction images have been obtained in our experiment using a simple phantom.

The excellent performance of this moving blocker method is based on the assumption that the signal in the blocked region is purely scatter signals, at least in the central part. However, this assumption is rarely satisfied for narrow lead strips in reality due to the penumbra

effect and the detector response effect. These effects make the signal spread from unblocked regions to the blocked regions. Therefore, the signal detected in the unblocked regions needed to be corrected before it was used to do the interpolation. Then we proposed to model the detector response function (DRF) in the blocked regions and several image deconvolution methods will be developed for recovering the true scatter signal in the blocked regions. We designed a slanted-edge simulation and a slanted-edge experiment to study these effects. This study will provide a theoretically sound and practically viable solution for the problems faced by the current moving blocker methods. By avoiding laborious parameter tuning, the final reconstruction with scatter correction can be more reliable and robust, which is an important component for its application in clinical practice.

2.2 Scatter correction using the moving blocker method

2.2.1 Moving blocker setup

The moving blocker system for CBCT imaging is shown in Figure 2-1 [10]. To simplify the process in this study, the blocker strips were shifted manually among 6 positions. The blocker system consists of equally spaced lead strips aligned along the v-direction of the detector. A beam attenuation blocker is inserted between the x-ray source and the phantom, and it moves back and forth along the u-direction of the detector as the gantry rotates around the z-axis. The signal measured in the blocked regions is assumed to be the scatter signal only, and the signal measured in the unblocked regions is the sum of the scatter signal and the primary signal. The scatter signal in the unblocked regions can be estimated from the blocked regions by using the cubic-spline interpolation. To avoid the penumbra effects of the strips, the region (about 10 pixels wide) adjacent to the edges of the strip are excluded from the scatter estimation in the experimental study. The primary signal is obtained by subtracting the interpolated scatter signal from the signal measured in the unblocked regions. A constrained-optimization-based TV minimization (CO-TV) algorithm is developed to reconstruct the entire volume within the FOV from the the primary signal in the unblocked region.

18
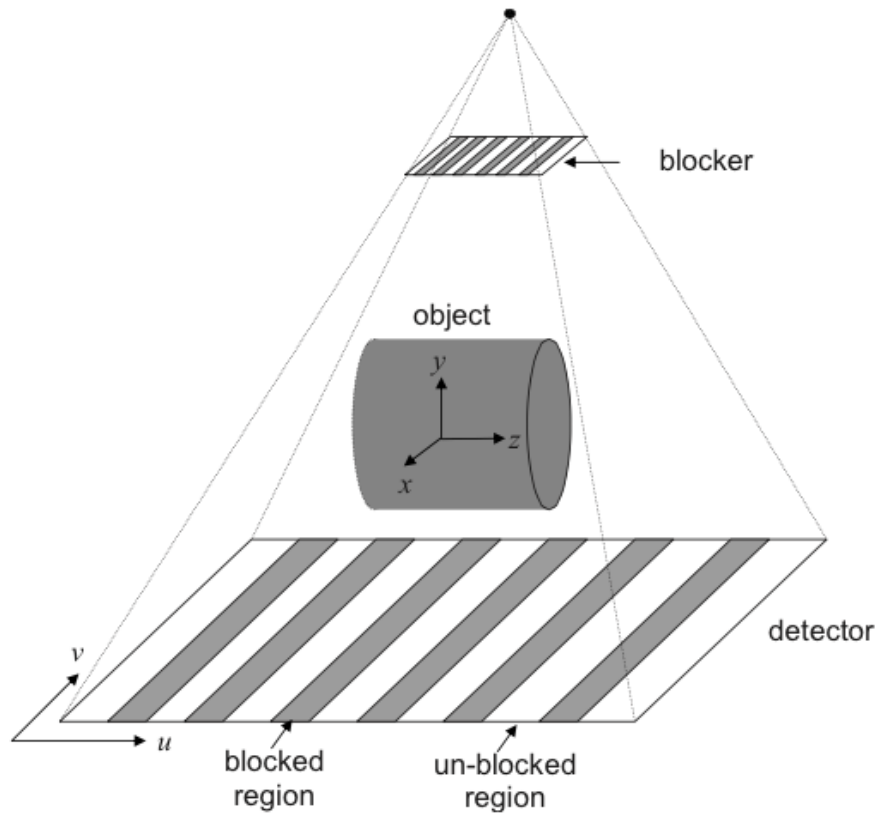
Figure 2-1 The moving blocker system [10]

2.2.2 Data acquisition

The blocker consists of 8 lead strips and the width of each lead strip is 3.2 mm. The lead strips are placed with a 3.2 mm pitch. The blocker is mounted on the F0 bow-tie filter of a CBCT machine. The lead strips of the blocker are aligned perpendicular to the rotation axis and cover the entire FOV all the time at a source-to-blocker distance of 310 mm. The source-to-axis distance is 1000 mm and the source-to-detector distance is 1500 mm. The number of projections for a full 360° rotation is approximately 678 and the total time for acquisition of one full circle of projection data is approximately 2 min. Each projection data contains 1024×768 pixels with a size of 0.388×0.388 mm^2. To save computation time during iterative reconstruction, projections were downsampled by a factor of 2 to yield a size 512×384 with pixel size 0.776

×0.776 mm^2. The tube voltage was 100 kVp and the tube current-time was 0.5 mA s per projection.

A commercial calibration phantom CatPhan® 600 (The Phantom Laboratory, Inc., Salem, NY) was used to evaluate the performance of the proposed method. Six CBCT scans were performed while the phantom was kept stationary. During each scan, the blocker was shifted 1 mm along the u-direction. To simulate continuous motion of the blocker during gantry rotation, the projection data of a single CBCT scan were selected from one of the six scans according to the following rule. For the nth projection data, let a denote the remainder after n is divided by 12. If a is smaller than 6, the nth projection data are chosen from ath of those six data sets; if a is larger than or equal to 6, the nth projection data are chosen from (12−a)th of those six data sets. By such a choice, the complete projection data set corresponds to a blocker moving at 1 cm/s.

2.2.3 Constrained-optimization-based reconstruction algorithm

When the blocker strips are used in projection data acquisition, the projection data are partially blocked at every projection and the total amount of projection data is smaller than in a normal CBCT scan. Iterative image reconstruction algorithms have the potential to substantially improve CBCT image quality from limited projection data. [19, 22, 61] Recent development of the compressed sensing theorem [62] has demonstrated that a signal can be exactly reconstructed from highly undersampled measurements. Several algorithms based [19, 22, 61] on the compressed sensing theorem have been proposed for CT image reconstruction from undersampled projections. In this work, image reconstruction from partially blocked projection data is formulated as a constrained optimization (CO) model under the framework of compressed sensing. Constrained optimization incorporates data fidelity and image constraints such as positivity, extreme values, and regularity measure. The constrained optimization generates a discrete image μ by minimizing certain functions of the image

$$\mu^* = arg\ min(f(\mu)) \qquad (2.2.1)$$

20

subject to the inequality constraints data fidelity and positivity:

$$|A\mu - p| \leq \varepsilon \qquad (2.2.2)$$

$$\mu \geq 0 \qquad (2.2.3)$$

where p is the vector of log-transformed projection measurements after scatter correction and μ is the vector of attenuation coefficients to be reconstructed. ε is the tolerance to enforce the data fidelity constraint which accounts for the inconsistency of the measured data such as noise and geometric deviation of the system matrix A. The element a_{ij} of the matrix A is the length of the intersection of projection ray j with pixel i and a_{ij} is calculated by Siddon's ray-tracing technique [63]. $f(\mu)$ is the prior knowledge imposed on the image and usually measures certain properties of the μ to be reconstructed. In this work, the total variation (TV) of the image is chosen as the regularity measure of μ

$$f(\mu) = \sum_{x,y,z} \sqrt{(\mu_{x,y,z} - \mu_{x-1,y,z})^2 + (\mu_{x,y,z} - \mu_{x,y-1,z})^2 + (\mu_{x,y,z} - \mu_{x,y,z-1})^2} \quad (2.\ 2.4)$$

In the following, we refer to the method described above as CO-TV. The constraint in Eq. (2.2.2) is enforced by the standard algebraic reconstruction technique (ART)

$$\mu_i^{(k+1)} = \mu_i^{(k)} + \lambda a_{ij} \left[\frac{p_j - \sum_i a_{ij}\mu_i^{(k)}}{\sum_i a_{ij}^2} \right] \qquad (2.2.5)$$

where k is the iterative step and λ is the relaxation factor which was chosen as 0.1 in this study. The objective function of Eq. (2.2.1) is minimized by the standard steepest gradient descent method

$$\mu^{(k'+1)} = \mu^{(k')} - \gamma \nabla f(\mu) \qquad (2.2.6)$$

where $\nabla f(\mu)$ is the gradient of function $f(\mu)$ and k' is the iteration step. γ is the step size and it is updated by steepest decent direction (line 15–19 in the pseudocode of [61]). To avoid a singularity in calculating $\nabla f(\mu)$, a small constant was added to the term inside the square root in Eq. (2.2.4). After each ART operation of Eq. (2.2.5), the resulting image is updated according to Eq. (2.2.6). The number of iterations for the steepest gradient descent step is set to 10 and the number of iterations for the ART step is set to 20 in this study [22, 61, 64].

2.2.4 Scatter correction scheme

This section shows some pre-processing steps and how the scatter correction method works. During the moving blocker CBCT acquisition, detected signal in the blocked regions is assumed to be attributed to scatter photons only, while the measured signal in the unblocked regions is contributed by both primary and scattered photons. Previous studies [56, 57] have showed that the scatter signal of CBCT projection is smooth and low-frequency signal. Here, the scatter signal detected in the blocked region was used to estimate the scatter fluence of the unblocked region using cubic-spline interpolation. To avoid the penumbra effect of the strips, data from regions adjacent to the edges of the strips were excluded, and only the central one-third of each blocked region was used in the scatter estimation in the experimental study. Before interpolation, a 3 × 3 median filter was applied to exclude extremity values of the measured scatters. A 1D 9-pixel moving average filter perpendicular to the lead strips was also used to further smooth the interpolated scatter maps [54, 76]. Primary signal in unblocked region was obtained by subtracting the estimated scatter signal. A line integral of each ray in unblocked region was then calculated by the logarithmic transform. To obtain accurate line integrals, a normalization scan (air scan) was acquired without the blocker. Image reconstruction was then performed on the corrected unblocked partial projection data.

Figure 2-2 and Figure 2-3 show an example projection image of air scan and Catphan scan respectively. The intensity of the projection image with blocker is decreased compared to the projection image without blocker, which can reduce the dose of radiation.
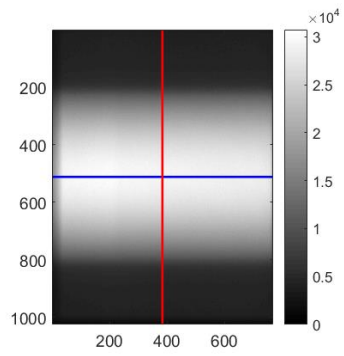
(a) Air scan without blocker
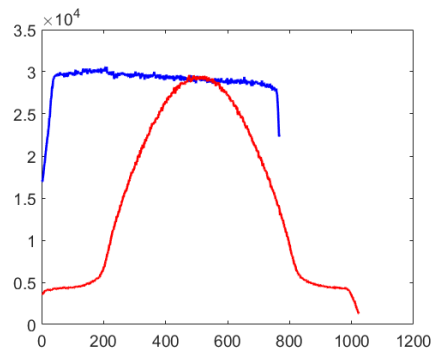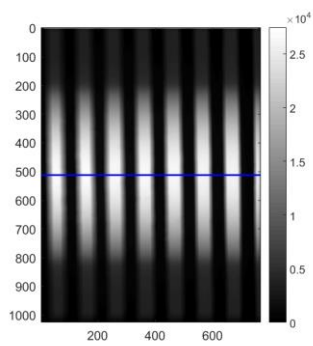
(b) Profile

(c) Air scan with blocker
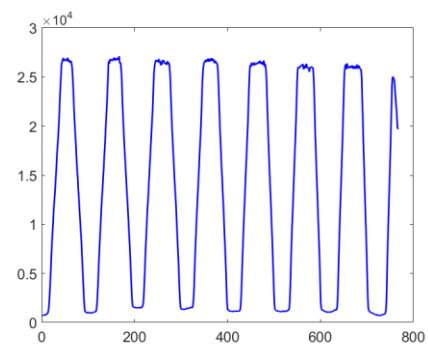
(d) Profile

Figure 2-2 Air scan

(a) Catphan without blocker

(b) Profile

(c) Catphan with blocker

(d) Profile
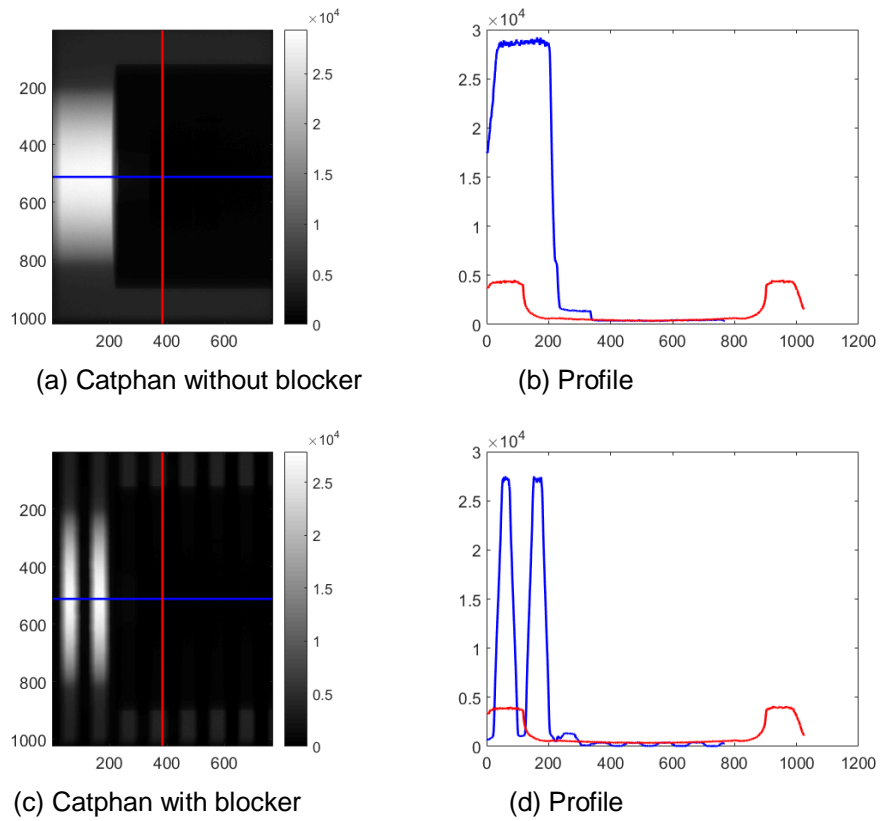
Figure 2-3 Catphan scan

Figure 2-4 shows how to estimate scatter signal from blocked regions. The blue line in (a) is the interest of region of measured signal, which is the sum of primary and scatter signal. The red line in (b) is the scatter signal we estimated in the blocked regions, and the estimated scatter signal in unblocked regions is interpolated in (c). Then the black line in (d) is the scatter corrected signal, which obtained by subtracting the red line from the blue line.
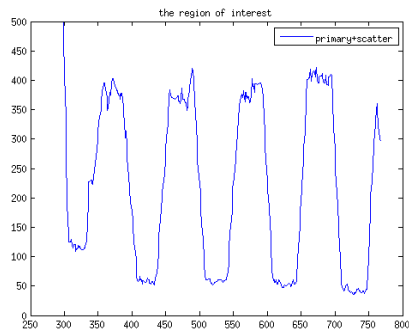
(a) Profile of measured signal   (b) Estimated scatter signal
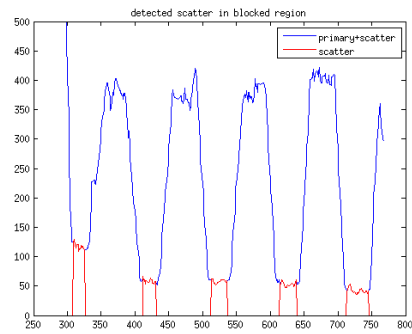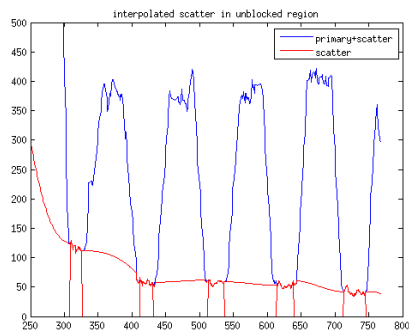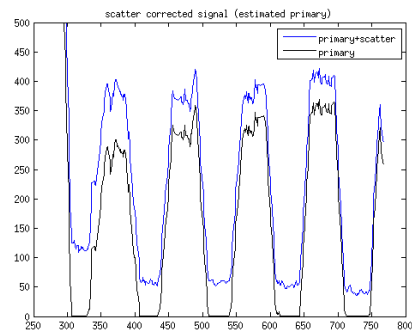
(c) Interpolated scatter signal   (d) Scatter corrected signal

Figure 2-4 Scatter correction

2.2.5 Reconstruction results

This section provides reconstruction results that illustrate the performance of the moving blocker method for scatter correction. We compare the axial images of the sensitometry module of moving blocker method to three competing methods in Figure 2-4. To evaluate the accuracy of the reconstructed CT number in the CBCT images, we calculated the mean CT number of seven ROIs within the sensitometry module. We also acquired fan-beam multi-detector CT (MDCT) images of the CatPhan[®] 600 phantom using a GE Discovery CT scanner (GE Medical Systems, Milwaukee, WI). The CT numbers from MDCT were used as the standard for comparison. The inaccuracy of CT number in CBCT was quantified by the root mean square error (RMSE) in the selected seven ROIs

$$RMSE = \sqrt{\Sigma_{k=1}^{7}(CT_{cone}^{k} - CT_{fan}^{k})^2} \quad (2.2.7)$$

where CT_{cone}^{k} and CT_{fan}^{k} denote the mean CT number of the kth ROI for CBCT and fan-beam CT, respectively. Table 2-1 lists the CT numbers of different ROIs in Figure 2-5. The CT numbers of different ROIs for eleven successive slices are shown in Figure 2-6 to Figure 2-12. Table 2-2 lists the RMSE of CT numbers of different ROIs for seven successive slices. The RMSE of the CT number in the CBCT images without scatter correction is 130. Using the proposed scatter correction strategy, the RMSE of the CT number is reduced to around 20 in all of the images reconstructed by different methods.
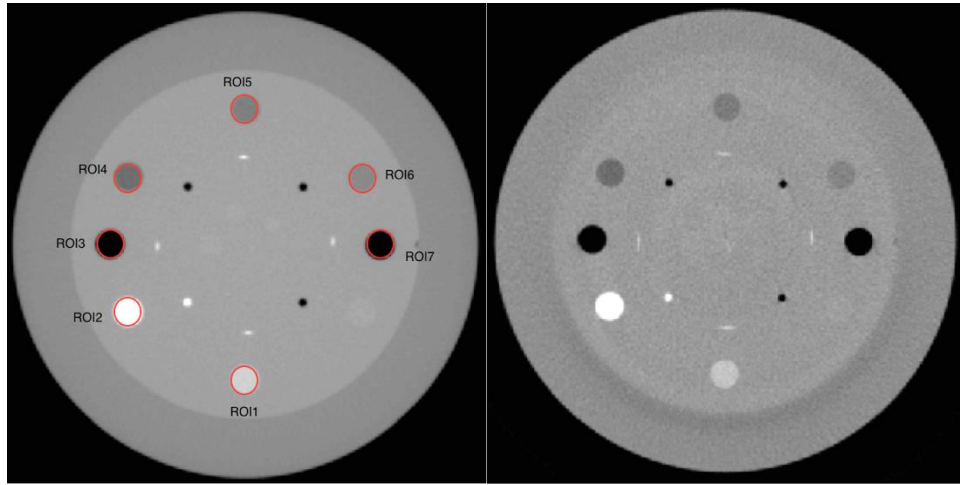
(a) MDCT	(b) CBCT
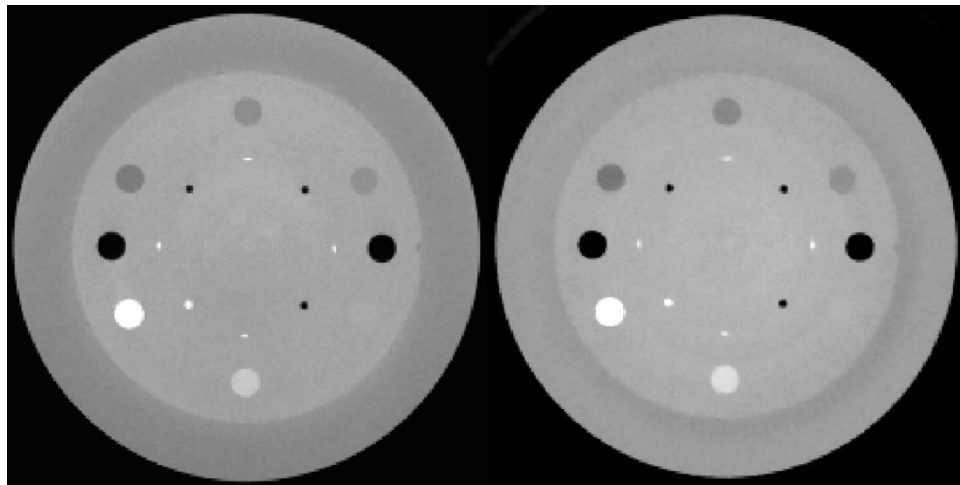
(c) No scatter correction	(d) Scatter correction

Figure 2-5 One axial slice of the Catphan 600 phantom sensitometry module

The selected slice image shown above: (a) benchmark fan-beam MDCT image, denoted as "MBCT";; (b) reconstructed image from CBCT machine (with some model-based scatter correction), denoted as "CBCT"; (c) CO-TV from unblocked projection data (no scatter correction), denoted as "No Scatter Correction"; and (d) CO-TV using both unblocked projection data and partially blocked projection data (with scatter correction) , denoted as "Scatter Correction";. ROIs labeled in (a) were used for evaluating CT number accuracy. Display widow [−800, 600] HU.
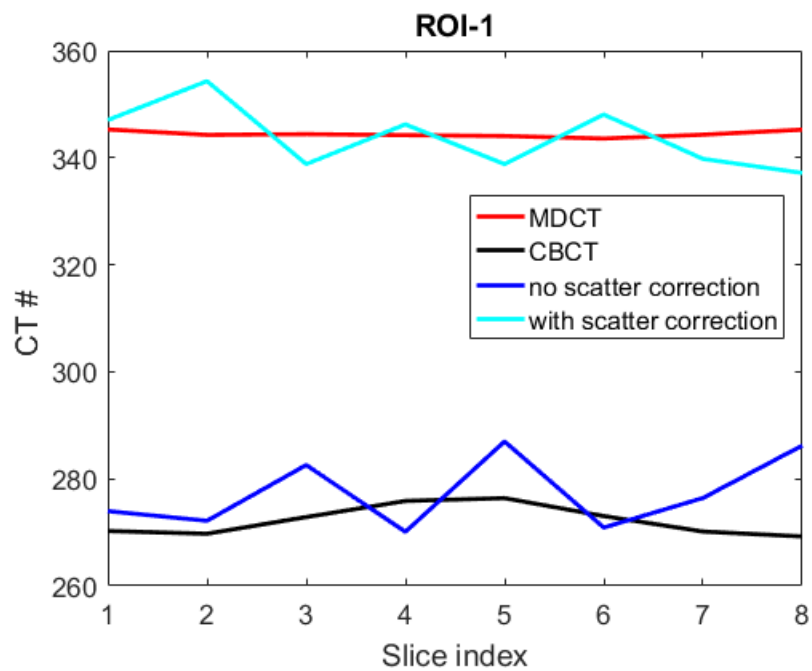
Figure 2-6 CT numbers of ROI-1
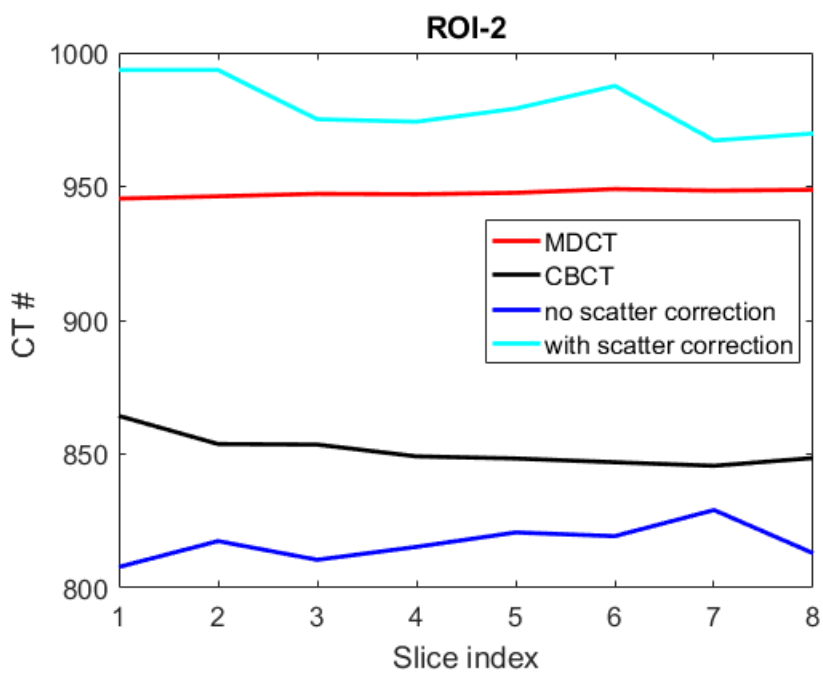
Figure 2-7 CT numbers of ROI-2
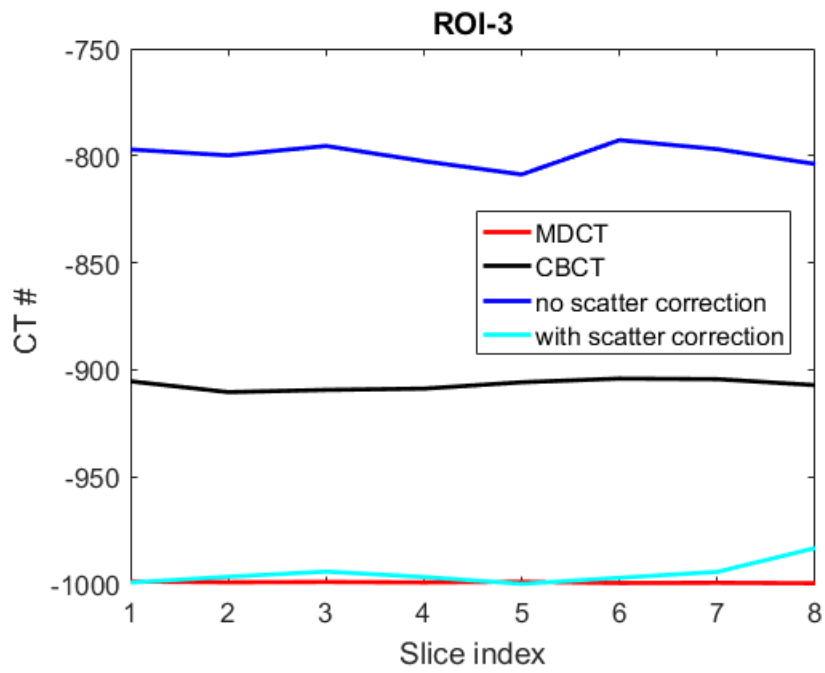
Figure 2-8 CT numbers of ROI-3
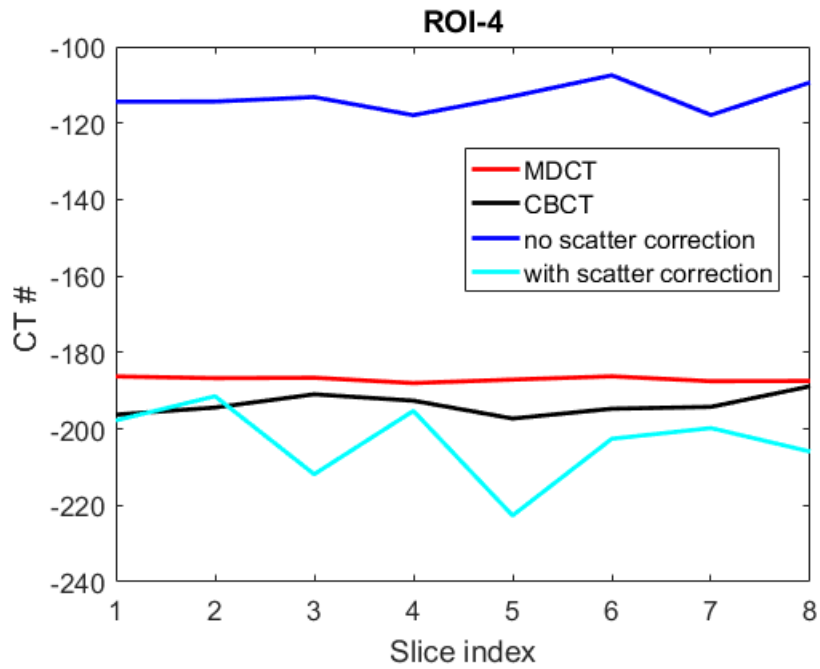
Figure 2-9 CT numbers of ROI-4
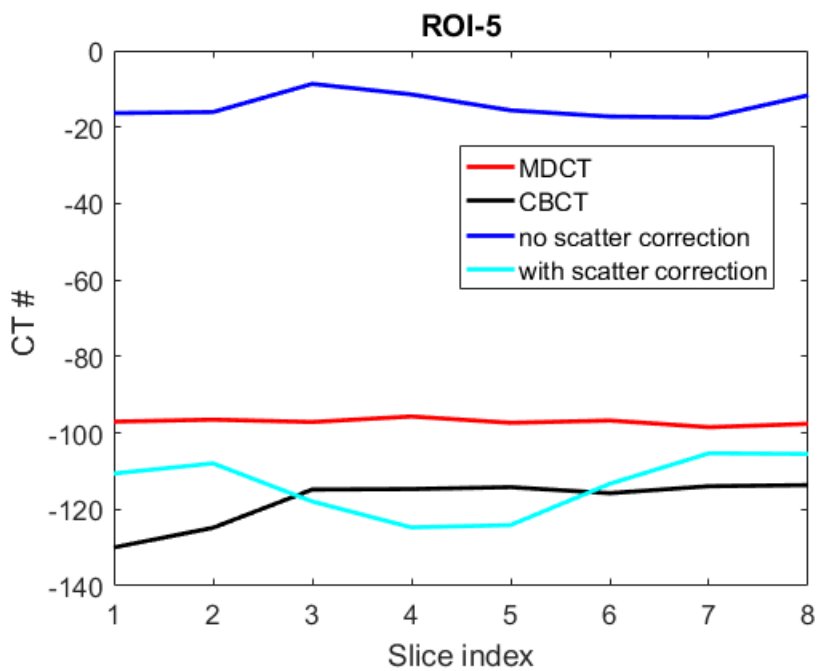
Figure 2-10 CT numbers of ROI-5
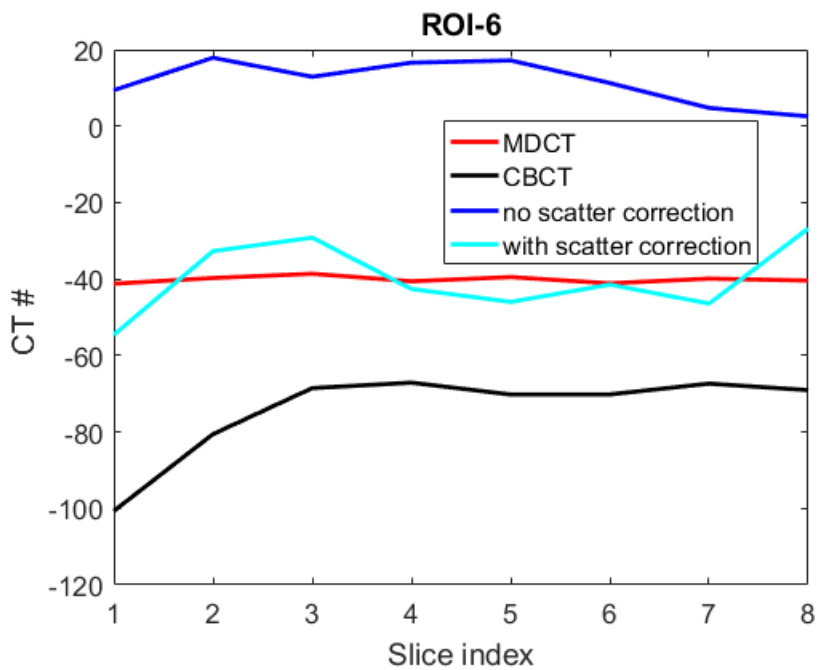
Figure 2-11 CT numbers of ROI-6
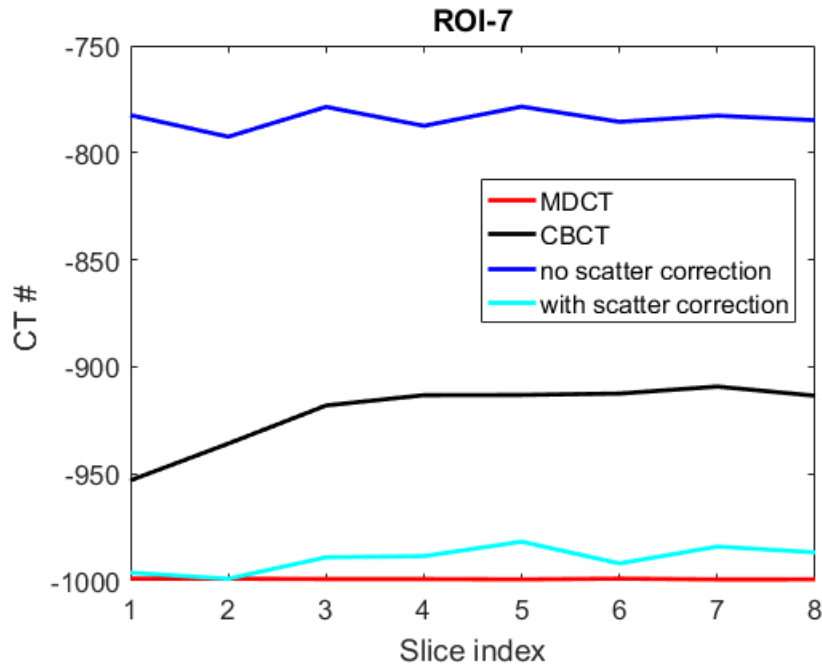
Figure 2-12 CT numbers of ROI-7

Table 2-1 Comparison of the CT number of seven ROIs of the Catphan 600

	ROI-1	ROI-2	ROI-3	ROI-4	ROI-5	ROI-6	ROI-7	RMSE
MDCT	344	948	-999	-187	-97	-39	-999	
CBCT	273	847	-904	-195	-116	-70	-913	70
No SC	270	820	-800	-124	-15	10	-780	130
SC	332	970	-991	-202	-111	-37	-993	20

Table 2-2 RMSE of CT numbers of different ROIs for seven successive slices

Slice number	1	2	3	4	5	6	7
CBCT	63	63	65	66	67	68	69
No SC	132	130	128	128	126	130	128
SC	17	20	19	17	19	16	12

2.2.6 Conclusion

The results of RMSE show that the moving blocker scatter correction method is effective. However, the scatter signal in this experiment had to be carefully extracted by

avoiding the edge pixels and a scaling was needed most time to compensate the spread of signal from unblocked regions for a good scatter correction performance. Therefore, we proposed a deconvolution method to avoid these drawbacks in next section.

2.3 Simulation study of deconvolution

2.3.1 Blocker-based scatter correction mathematical models

The fundamental assumption in blocker-based scatter estimation lies on:

$$S^{ideal}(u,v) \begin{cases} S_{p(u,v)} + S_{s(u,v)}, & (u,v) \in blocked\ region \\ S_{s(u,v)}, & (u,v) \in unblocked\ region \end{cases} \qquad (2.3.1)$$

where $S^{ideal}(u,v)$ is the "ideally" measured signal, $S_{p(u,v)}$ is the primary signal and $S_{s(u,v)}$ is the scatter signal. Since in the blocked regions the signal is deemed purely scatter and the scatter i-s a low-frequency signal at least in longitudinal direction [54], the scatter in blocked region can be estimated through interpolation of signals in blocked region. Then, the primary signal in unblocked region can be recovered by subtracting estimated scatter signal from measured total signal and used for reconstruction. However, the assumption of pure scatter in blocked regions is usually violated in reality. As demonstrated by the air scan of the blocker (without the object in Figure 1) in Figure 2-2, the edges between blocked and unblocked regions do not show a vertically straight transition from high intensity to low intensity. In addition, significantly amount of signal still exists in the blocked region, which should be (close to) zero by the assumption. Therefore, the scatter signal in the previous experiment had to be carefully extracted by avoiding the edge pixels and a scaling was needed most time to compensate the spread of signal from unblocked regions for a good scatter correction performance [10, 11].

In this study, we will investigate the sources for the contamination of scatter in blocked regions and propose several methods to extract more faithful scatter signals without empirical parameter tuning. If we assume an ideal point x-ray source and no detector veiling/scatter glare, the detect signal can be described as

$$S^{ideal}(u,v) = S_{p(u,v)} \sum_{i=1}^{k} \Pi(\frac{u-u_i}{w}) + S_s(u,v) \qquad (2.3.2)$$

32

where the primary signal is $S_{p(u,v)} = I_0 e^{-\int_L \mu(x,y,z)dl}$ with the uniform source intensity I_0 and the ray path L from the source to the point *(u,v)* on the detector, $S_{S(u,v)}$ is the object scatter signal that can be modeled as a convolution of incident fluence and the scatter kernel [46]. $\Pi(\bullet)$ is the standard rectangular function (1 inside the window and 0 outside) and $\sum_{i=1}^{k} \Pi(\frac{u-u_i}{w})$ represents the ideal projection image of *K* blockers (with the center μ_1 and the width *w*) on the detector. Note that blocked regions are outside the rectangular windows. This equation is equivalent to Eq. (2.3.1).

However, the real measured signal does not exactly follow Eq. (2.3.2) as can be seen in Figure 2-1. At least two major blurring factors have to be taken into account: 1) the response function of the flat panel detector (FPD); and 2) the penumbra effect due to the finite x-ray source distribution. (Note that the diffraction effects can be neglected because the x-ray wavelengths are very small ($\sim 10^{-11}$ m) and the width of the blocker is several millimeters. Thus, under the usual CBCT imaging setup, Fresnel number is much greater than one, which does not satisfy the condition to generate a bright spot behind the blocker.) Therefore, if assuming linear shift invariant (LSI) for both effects, the measured data can be expressed as:

$$S_{(u,v)} = S^{ideal}(u,v) \otimes PSF(u,v) + n(u,v) \qquad (2.3.3)$$

$$= S_p(u,v) \sum_{i=1}^{k} \Pi \left\{ \frac{u-u_i}{w} \right\} \otimes DRF(u,v) \otimes PEF(u,v) + n(u,v)$$

where $\otimes$ denotes convolution, DRF(u,v) is the point spread function of the FPD, PEF(u,v) models the blurring due to the penumbra effect, S_S^* *(u,v)* is the object scatter signal in Eq. (2.3.2) convolved by DRF(u,v) and PEF(u,v), and $n(u,v)$ is the detector electronic noise. It is straightforward to see that the signal reaching the FPD will be blurred by DRF. The blurring effect from PEF comes from the source distribution that can be modeled as convolution of an ideal point source (see Eq. (2.3.6)). Comparing Eq. (2.3.3) with Eq. (2.3.2), we can see that the primary signal can spread outside the rectangular windows and cause the contamination of the

scatter signal in unblocked regions. Although the blocker width may be increased to mitigate this contamination, practically this is not desired because it will compromise the primary signal coverage and deteriorate the reconstruction.

The primary goal of this work is to use deconvolution methods to recover the ideal signal $S^{ideal}(u,v)$ in Eq. (2.3.2) from the measured signal $S_{(u,v)}$ in Eq. (2.3.3). Consequently, the signal in the blocked regions (i.e. outside the window function) can better represent true scatter (at least in the central part of the region), which will lead to more accurate estimate of the primary signal for reconstruction.

2.3.2 Models of the detector response and the penumbra effect

A. Modeling detector response function (DRF)

An ideal point x-ray beam will generate a spread in the FPD due to the effects of radiation scatter, light diffusion, and charge sharing etc. Since the ideal point beam is hard to achieve, the slanted-edge method [65, 66] will be used to estimate the detector response function (DRF), i.e. point spread function [67]. A lead sheet with sharp and straight edge will be placed directly on the top of the FPD to avoid off-focal radiation and environmental scatter. A uniform incident fluence on the measured area will be assured by calibration. The angle of the edge is not parallel to the u or v axis, but slanted slightly (<5°). This allows the gradient of the edge to be measured at various phases relative to the detector element and generates an oversampled edge profile as shown in Figure 2-13, which will provide extra high frequency response information.
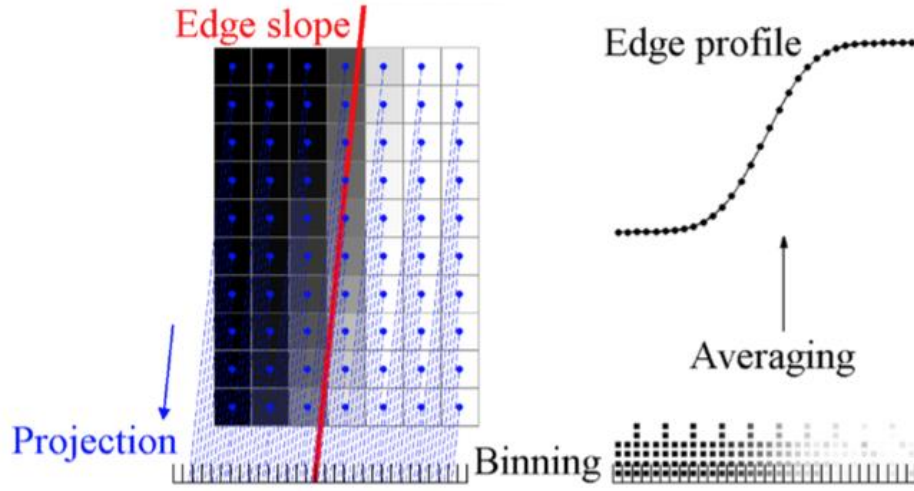
Figure 2-13 ESF estimation using the slanted edge method [68]

The empirical line spread function (LSF) can be obtained by taking the derivative of the edge profile. The empirical LSF will be further fitted to the following parametric function:

$$LSF^{fit}(u) = \frac{a_1}{\sqrt{2\pi b_1^2}} e^{-u^2/2b_1^2} + \frac{a_2}{\pi b_2^2} |u| K_1(\frac{|u|}{b_2}) + \frac{1-a_1-a_2}{\pi b_3} \frac{1}{1+u^2/b_3^2} \qquad (2.3.4)$$

where $K_1(\bullet)$ is a first-order modified Bessel function. This function is proposed to model the long tail of LSF and the weighted least squares can be used to find the parameters [67]. The LSF will be measured and calculated at multiple positions on the detector with both u and v directions to make sure that the DRF of FPD is spatial invariant and rotationally symmetric. Given rotational symmetry, the DRF can be expressed as:

$$DRF^{fit}(r) = \frac{a_1}{2\pi b_1^2} e^{-r^2/2b_1^2} + \frac{a_2}{2\pi b_2^2} e^{-r/b_2} + \frac{1-a_1-a_2}{2\pi b_3^2} \frac{1}{(1+r^2/b_3^2)^{3/2}} \qquad (2.3.5)$$

where r is equal to $\sqrt{u^2+v^2}$. In Eq. (2.3.5), it is tempting to attribute the three terms as modeling the distributions of the incident intensity in the scintillator, the diffusion of scattered optical

photons, and the scatter of x-ray photons in the detector panel and housing, respectively [67]. However, we treat them as a general description of a point spread function with variable tail effects, i.e. the short range for the first Gaussian term, the medium range of the exponential term, and the long range of the polynomial (Lorentzian) term.

B. Modeling penumbra effect function (PEF)

The finite size of x-ray focal spot (inside the full width half maximum (FWHM) of the source, <1 mm) and the off-focal-spot radiation (outside the FWHM of the source with non-negligible radiation, ~several mm) produce the penumbra effect of the blockers. This effect results in different I_0 values as shown in Figure 2-14, where the black region on the detector is totally blocked by the blocker (when ignoring the detector response in section 2.3.1), the green ones are unblocked, so called umbras, and the red ones are partly shun by x-ray, so called penumbras.
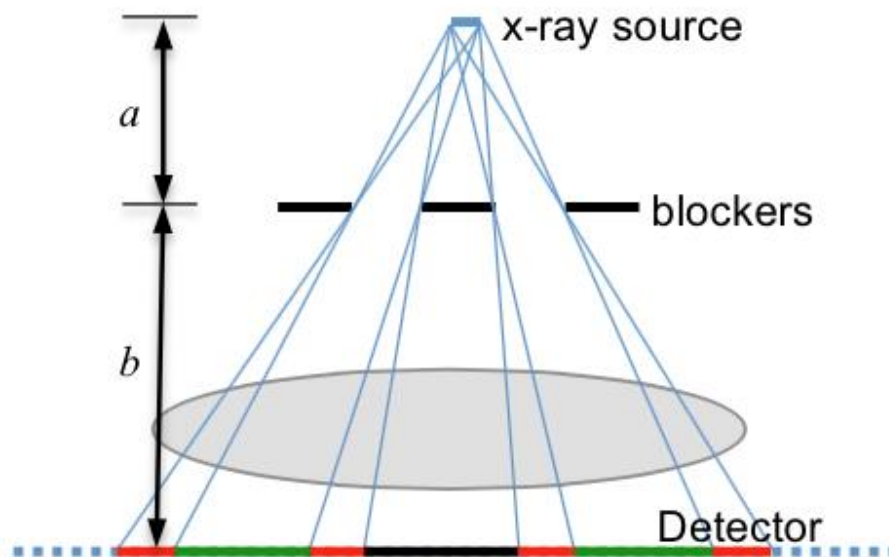
Figure 2-14 Penumbra effect

Given the focal spot length L_f , the source to the blocker distance a, and the blocker to the detector distance b, the penumbra size can be computed as $L_p = (bL_f)/a$. If the blockers

36

have the equal width and spacing, denoted as d, an ideal point source (i.e. an infinitesimally small source) would result in a uniform alternating pattern of the blocked and unblocked regions on the detector with the equal size of $L_I = d(a + b)/a$, which is the sum of one black (or green) region and one red region. Given a typical values of L_f=0.4 mm, a =300 mm, b = 1200 mm, and d =3 mm [11, 69], L_p is 1.6 mm and L_I is 15 mm. Therefore, the penumbra could take more than 10% of the ideally blocked region even by considering only the finite size of the focal spot. If taking the off-focal-spot radiation into account, which is in the same order of the size of the blocker, the penumbra effect region could be ten-fold greater and spread to the whole blocked region [69]. Following the recent study of penumbra effect of the collimator blades, we can model the actual incident intensity L_A as

$$I_A(u, v) = I_0 \otimes f(u \cdot a/b, \ v \cdot a/b) = I_0 \otimes PEF(u, v) \qquad (2.3.6)$$

I_0 has the uniform value inside the illuminated area and 0 outside, and f is the x-ray source distribution. The penumbra effect function (PEF) is then defined as the source distribution magnified on the detector by a factor of b/a. Note that the penumbra effect of the collimator blades is around the borders of FOV and can be ignored compared to that of the blockers in the regions of interest. Although the off-focal-spot radiation is generally small, it significantly contributes to the spread due the convolution on a large off-focal-spot area in Eq. (2.3.6).

The pinhole method will be used for the measurement of source distribution because it is easy to implement and able to provide 2D distribution [69, 70]. Briefly, a standard pinhole assembly is attached to the surface of the field collimator. After calibration, the focal spot, pinhole, and the center of detector are aligned, and a magnified image of the focal spot is projected onto the detector. The background signals measured by blocking the pinhole are subtracted from the pinhole measurement to get the clean distribution of the source on the detector by assuming a negligible DRF influence on PEF. The deconvolution methods

described in next section will be used to test the negligible DRF influence hypothesis. If the pinhole method cannot provide satisfying measure of PEF, advanced coded aperture methods can be used [71]. Assuming a rotational symmetry, a similar parametric function Eq. (2.3.5) can be used to break down PEF into different spread range factors.

2.3.3 Recovery of true scatter in blocked regions

Once we accurately estimate DRF and PEF based on Eq. (2.3.5), the deconvolution techniques can be used to recover true scatter in blocked regions, i.e. to reverse the effect of DRF and PEF in Eq. (2.3.3) so that Eq. (2.3.2) can be satisfied to a maximum extent and the estimation of scatter in unblocked region can follow the routine. In the following context, we denote $F(\bullet)$ as Fourier transform of the function from the spatial domain to the spatial frequency domain, and $F^{-1}(\bullet)$ as inverse Fourier transform. The multiplication, division and comparison involving an array (e.g. S, S^{ideal} and their Fourier transform) are element wise, unless otherwise stated.

A. Inverse and Wiener filtering

The most straightforward method is the inverse filtering. In this method, the derived DRF and PEF are transformed into the spatial frequency domain, denoted as $\mathcal{F}(\text{DRF})$ and $\mathcal{F}(\text{PEF})$, so is the measured signal S, $\mathcal{F}(\text{S})$. Then, the recovered signal can be expressed as $\tilde{S}^{ideal} = \mathcal{F}^{-1}(\frac{\mathcal{F}(\text{S})}{\mathcal{F}(\text{DRF})\mathcal{F}(\text{PEF})})$. It is well known that the direct inverse filtering will produce the high frequency ringing artifacts. Since the contamination in the central part of the blocked region can be only introduced by the long tails of DRF and PEF, which can be represented by the last two terms (exponential + Lorentzian) or the last one term (Lorentzian), denoted as DRF^{LT} and PEF^{LT}, the inverse filtering can be achieved by $\tilde{S}^{ideal} = \mathcal{F}^{-1}(\frac{\mathcal{F}(\text{S})}{\mathcal{F}(\text{DRF})\mathcal{F}(\text{PEF})})$ instead. As shown in [67], this process can effectively remove the long tail effect of the detector scatter without

introducing new artifacts. We expect the similar performance for the long tail effect of the penumbra.

The electronic noise term n(u,v) in Eq. (2.3.3) can be modeled as a Gaussian white noise and its power spectral function (PSF) can be estimated from either the flood field or the dark image. The Wiener deconvolution can be expressed as

$$\tilde{S}^{ideal} = \mathcal{F}^{-1}(\frac{\text{H}^* \bullet PSF(\text{S})}{|H|^2 \text{PSF(S)} + \text{PSF(n)}}) \qquad (2.3.7)$$

where $H = \mathcal{F}(DRF)\mathcal{F}(PEF)$ or $\mathcal{F}(DRF^{LT})\mathcal{F}(PEF^{LT})$, * denotes the complex conjugate, and PSF(S) and PSF(n) are power spectral functions of the signal S and n, respectively.

B. Maximum likelihood estimate using the Richardson-Lucy algorithm

From Eq. (2.3.3), the ideal signal S^{ideal} consists of both the primary and scatter signals, which follow Poisson distribution and is blurred by a known point spread function, $h = DRF \otimes ERF$. The maximum likelihood estimate of S^{ideal} given the measurements S and h can be obtained using the iterative Richardson-Lucy algorithm [48, 49] as follows

$$S^{ideal(t+1)} = S^{ideal(t)}(\frac{S}{S^{ideal(t)} \otimes h} \otimes \hat{h}) \qquad (2.3.8)$$

where $S^{ideal(t)}$ and $S^{ideal(t+1)}$ are estimate of S^{ideal} at t^{th} and $(t+1)^{th}$ iteration, respectively, and $\hat{h} = h(-u, -v)$. In case of high noise, e.g. the blocked region with low statistical counts, a regularization term, denoted R(S), can be added to the Richardson-Lucy algorithm [74, 75]. The iteration can be modified by adding a scaling factor, $(1 - \lambda \text{div}(R(S^{ideal(t)})))^{-1}$, to the right side of Eq. (2.3.8), where div is the divergence of the regularization function R(S). Different regularization functions, such as L_2 norm, total variation (TV) norm, and Huber-norm, will be

39

tested if the regularization is necessary although the use of heuristic parameter is generally avoided.

2.3.4 Model validation and evaluation of scatter recovery methods

To investigate whether deconvolution methods can improve the scatter estimation under different blurring and noise conditions for blocker-based methods for CBCT. An "ideal" projection image with scatter was first simulated for blocker-based CBCT data acquisition by assuming no blurring effect and no noise. The ideal image was then convolved with long-tail PSF with different width to mimic the blurring effect from the finite focal spot and detector response. Different levels of noise were also added. Three deconvolution methods: 1) inverse filtering; 2) Wiener; and 3) Richardson-Lucy, were used to recover the scatter signal in the blocked regions. The root mean square error (RMSE) of estimated scatter serves as a quantitative measure for the performance of different methods under different blurring and noise conditions.

2.3.5 Simulation results

The phantom we simulated is from one of the projection image of CBCT, and six black strips is applied as blocker strips in Figure 2-15 (b). The size of the phantom is 1024*768 with the 0.388 mm pixel size. Then we generated a 2D scatter signal (d), which is generated from a Gaussian function (sigma=600). By adding the scatter signal to the projection image, we obtained the profile with scatter contamination(e).
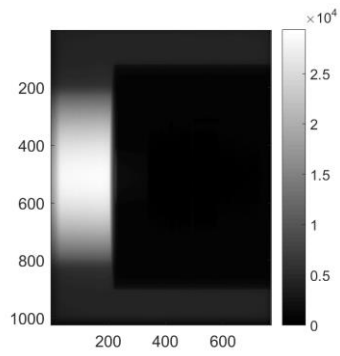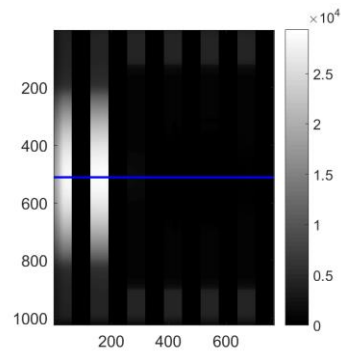
(a) Projection image   (b) Applied blocker
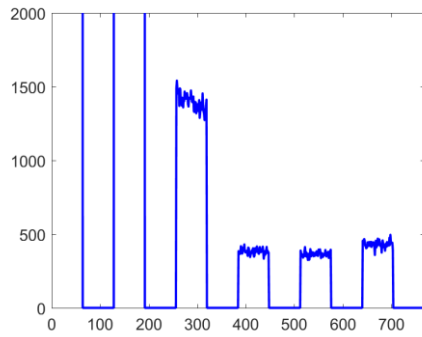
(c) Profile without scatter   (d) Generated scatter signal
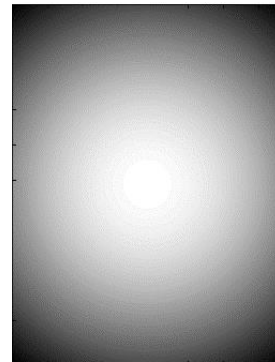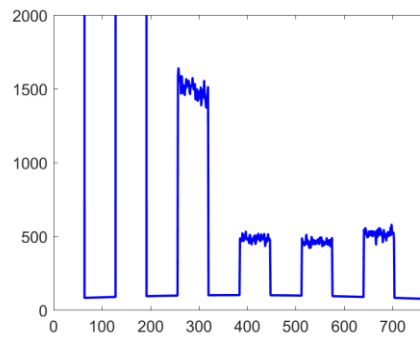
(e) profile with scatter

Figure 2-15 Simulated phantom and scatter signal

There are 5 different width of PSF that are simulated using Eq. (2.3.5). The size of the

PSF is 81*81 pixels (0.388 mm pixel size). We choose the full width tenth maximum (FWTM) as

the width of the PSF. The corresponding FWTM is 0.155mm, 6.2 mm, 12.4 mm, 18.6 mm and 24.8 mm respectively and first two of them are shown in Figure 2-16.

(a) PSF-1   (b) LSF

(c) PSF-2   (d) LSF
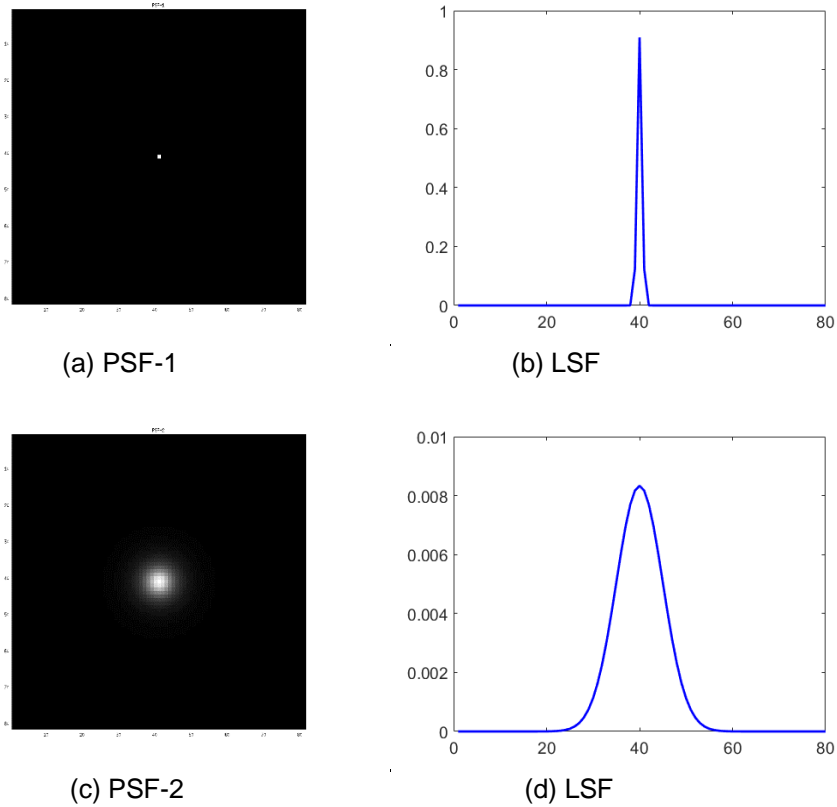
Figure 2-16 Two different PSF and the corresponding LSF

There are five different level of noise are added to the image after they convolved the five PSF. They are defined as signal-to-noise ratio (SNR) at 160dB, 80dB, 40dB, 20dB and 10dB (i.e. 0.0001%, 0.01%, 1%,10% and 20% noise).Two convolved image and selected profile are shown in Figure 2-17. The sharp edge became smooth because of the blur effect of the convolution.
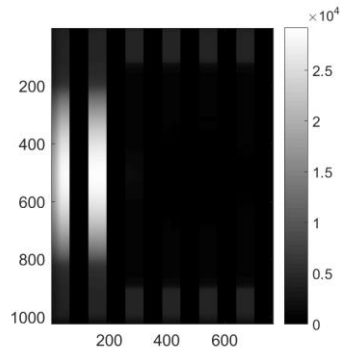
(a) Convolved with PSF-1   (b) Selected profile
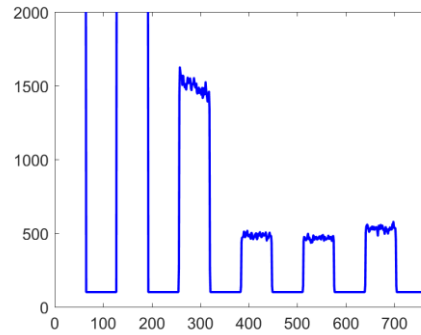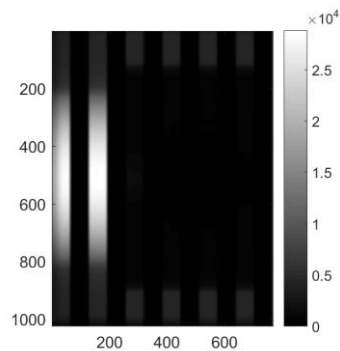
(c) Convolved with PSF-2   (d) Selected profile
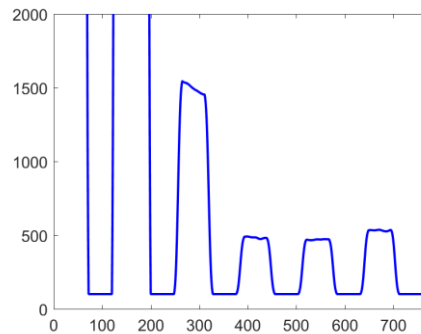
Figure 2-17 Convolved image

The final step is to deconvolve the blurred and noisy image using the corresponding PSF. The image can be restored to the original image when there is no noise added. However, the noise cannot be removed from the blurred image because we don't have a model of it. Using the Wiener and Richardson-Lucy deconvolution, the noise can be suppressed to some extent. Two typical line profiles are shown in Figure 2-18, low noise and medium noise. The root mean square error (RMSE) for different methods is shown in the Table 2-3.

(a) Low Noise (SNR=80dB)　　　　　(b) Medium Noise (SNR=40dB)
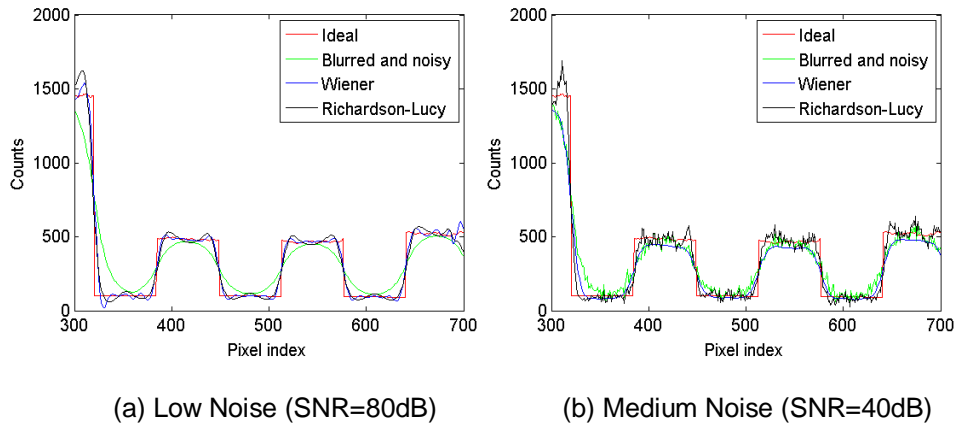
Figure 2-18 Deconvolved line profiles

The line profiles (perpendicular to the orientation of blockers) of the ground truth and for different scatter estimation methods are shown in above. The Ideal means ground truth without blur and noise, the Blurred and noisy means measured for direct scatter estimation, the Wiener means after Wiener deconvolution of the measured data and the Richardson-Lucy means after Richardson-Lucy deconvolution of the measured data.

Table 2-3 RMSE of the profile of blurred image

SNR (dB)	160	80	40	20	10
PSF-1	0	30	151	303	605
PSF-2	45	53	130	240	466
PSF-3	82	82	115	200	393
PSF-4	110	114	201	355	686
PSF-5	130	136	187	282	498

Table 2-4 RMSE of the profile of deblurred image (Wiener)

SNR (dB)	160	80	40	20	10
PSF-1	0	28	77	89	93
PSF-2	1	8	18	26	37
PSF-3	4	9	27	31	31
PSF-4	18	25	34	34	33
PSF-5	48	36	36	36	37

Table 2-5 RMSE of the profile of deblurred image (Richardson-Lucy)

SNR (dB)	160	80	40	20	10
PSF-1	0	30	113	216	431
PSF-2	0	30	114	214	422
PSF-3	0	30	96	130	343
PSF-4	0	30	90	128	275
PSF-5	0	30	91	177	308

The RMSE values of estimated scatter using different methods are summarized In Figure 2-19. The direct method suffers from the increased width of PSF and increased noise (Blue bars). After either Wiener or Richardson-Lucy deconvolution, the scatter estimation performance is significantly improved. In general, Wiener is robust to the change of noise levels and Richardson-Lucy seems to work well with the wide PSF. The deconvolution methods can achieve from as high as 20-fold improvement (Narrow PSF and Low noise) to a typical 4-fold improvement (Medium PSF and Medium noise).

(a) Narrow PSF   (FWTM = 6.2mm)   (b) Medium PSF (FWTM = 12.4mm)

(c) Wide PSF (FWTM = 24.8mm)
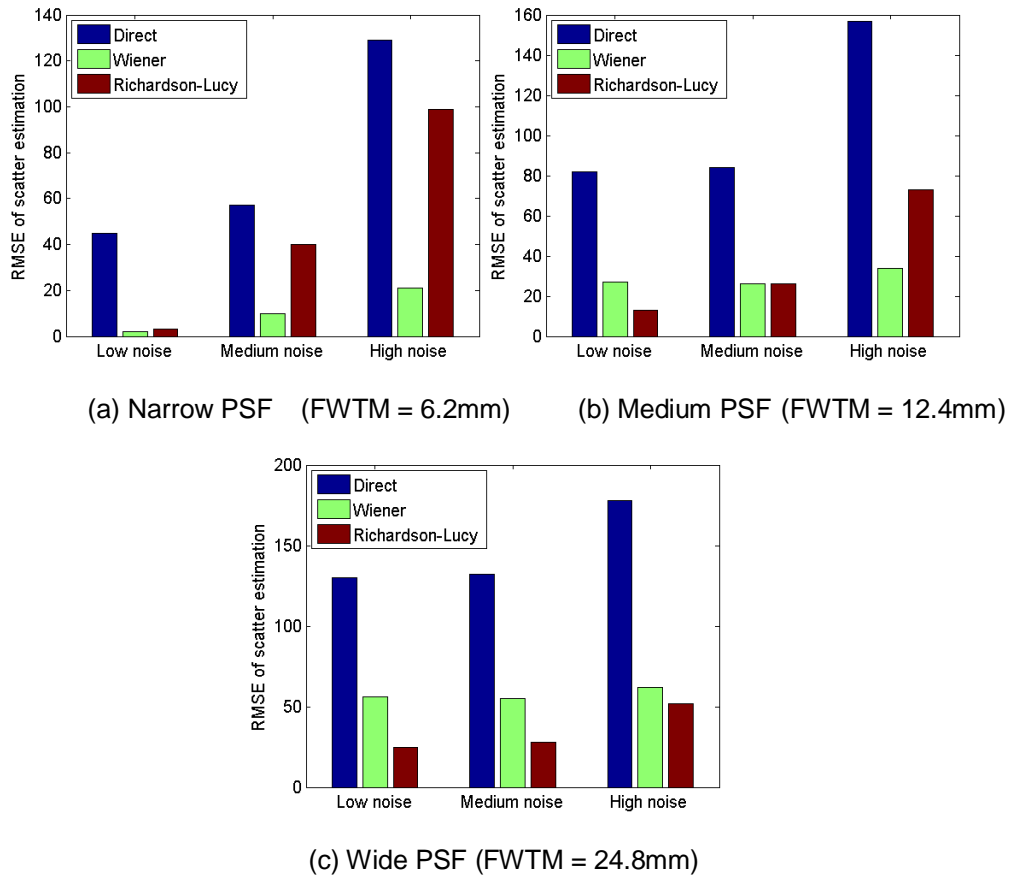
Figure 2-19 Root mean square error (RMSE)

The RMSE of estimated scatter using different methods are shown in above (Direct: using signal in the blocked region to estimate scatter directly; Wiener: Wiener deconvolution followed by direct scatter estimation; Richardson-Lucy: Richardson-Lucy deconvolution followed by direct scatter estimation; under different blurring and noise conditions. (Note the inverse filtering is very sensitive to noise and omitted here.)

2.3.6 Conclusion

We investigated several deconvolution methods to recover the scatter signal in the blocked region for blocker-based scatter correction for CBCT. Our simulation results demonstrate that Wiener and Richardson-Lucy deconvolution can significantly improve the scatter estimation compared to the direct method. Due to the blurring effect, the scatter signal in

the blocked region is contaminated by the primary signal in the unblocked region. The direct use of the signal in the blocked region to estimate scatter ("direct method") leads to large RMSE, whose values increase with the increased width of PSF and increased noise. The inverse filtering is very sensitive to noise and practically useless. The Wiener and Richardson-Lucy deconvolution methods significantly improve scatter estimation compared to the direct method. For a typical medium PSF and medium noise condition, both methods (~20) can achieve 4-fold improvement over the direct method (~80). The Wiener method deals better with large noise and Richardson-Lucy works better on large PSF.

2.4 Slanted-edge study for deriving the PSF

2.4.1 Introduction

We performed an slanted-edge experiment to model the detector response function (DRF) for a flat panel detector (FPD). The slanted-edge method [65, 66] can be used to estimate the detector response function (DRF), i.e. point spread function [67]. A lead sheet with sharp and straight edge will be placed directly on the top of the FPD to avoid off-focal radiation and environmental scatter. A uniform incident fluence on the measured area will be assured by calibration. The angle of the edge is not parallel to the u or v axis, but slanted slightly (<5°). This allows the gradient of the edge to be measured at various phases relative to the detector element and generates an oversampled edge profile as shown in Figure 2-13, which will provide extra high frequency response information. The novelty of this work is to investigate the effectiveness of deconvolution methods on improving blocker-based CBCT scatter estimation. Due to the blurring effect from the X-ray source distribution and the detector response, the scatter signal in the blocked region is contaminated by the primary signal in the unblocked region, which leads to incorrect estimate of scatter in the whole projection image if no empirically adjustments were conducted. This work will provide a theoretically sound and practical solution to this problem and preliminary evidence that to what extent deconvolution methods can work. The purpose of this experiment is to measure the line spread function (LSF)

47

and the modulation transfer function (MTF) of the projection image, then estimate the point spread function (PSF) and use them to deconvolve the original image to decrease the impact of the detector response effect.

2.4.2 slanted-edge method

Figure 2-20 and Figure 2-21 show the projection image of a slanted lead plate and its edge profile. The ideal edge profile has a sharp corner but the real edge profile doesn't (shown in Figure 2-20(c)). Our goal of this experiment is to process the projection image to make the edge profile of the image sharp at the corner.

(a) slanted edge

(b) detected edge

(c) estimated ESF
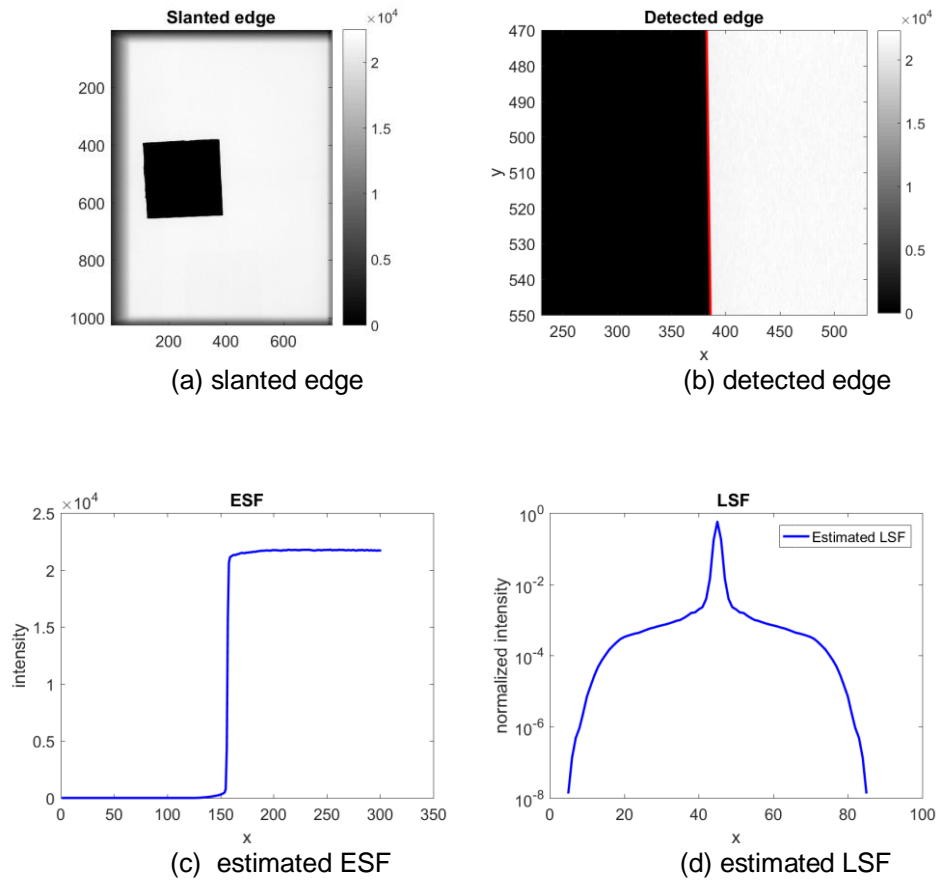
(d) estimated LSF

Figure 2-20 Modeling LSF
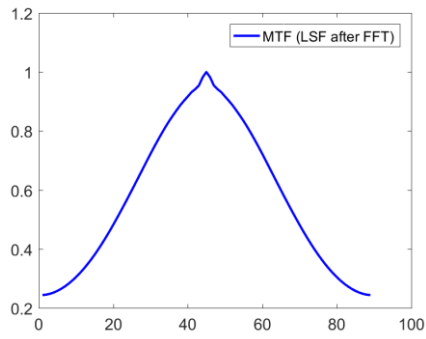
(a) estimated MTF
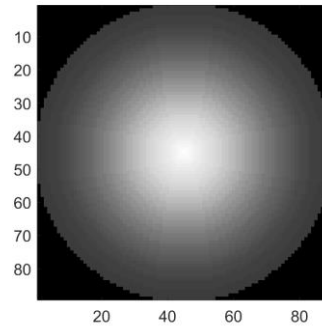
(b) estimated 2D MTF
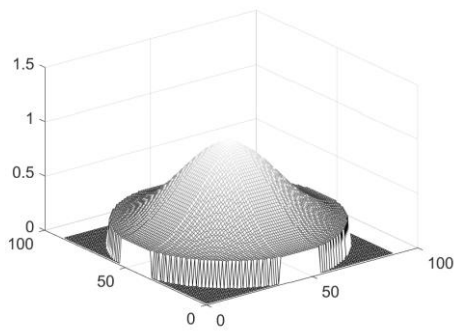
(c) estimated 2D MTF
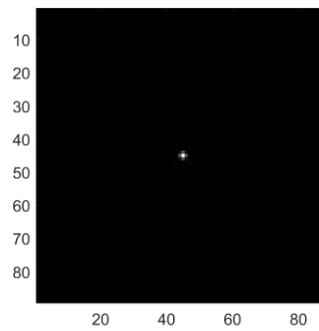
(d) estimated 2D PSF
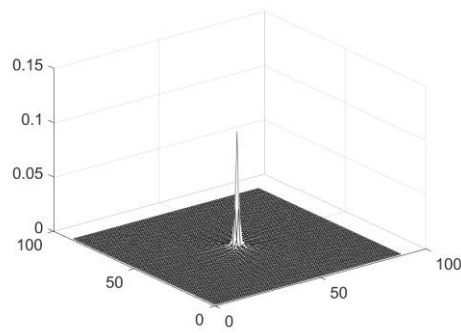
(e) estimated 3D distribution of 2D PSF

Figure 2-21 Caculation of PSF

2.4.3 Results of different LSF

      We compared three kinds of methods to drive the LSF and PSF. The estimated LSF and PSF were obtained from the experiment as shown in Figure 2-22. The fitted LSF and PSF were obtained by fitting the estimated LSF to the Eq. (2.3.4) and Eq. (2.3.5). The parametric LSF and PSF were obtained from the the Eq. (2.3.4) and Eq. (2.3.5) using the parameters in the reference [22]. The dotted lines are the corresponding LSF derived from the PSF. From the Figure 2-23, we conclude that the estimated LSF is close to the parametric LSF. The fitted LSF has some differences from the esimtaed LSF, which is caused by the fitting method we use. The results of the deconvolution for the three kinds of PSF are shown in the Figure 2-23. (a) and (b) are estimated PSF. (c) and (d) are parametirc PSF. (e) and (f) are fitted PSF. The RMSE for the profile of blurred image is 575. It became 1000, 55, 57 for the three PSF.
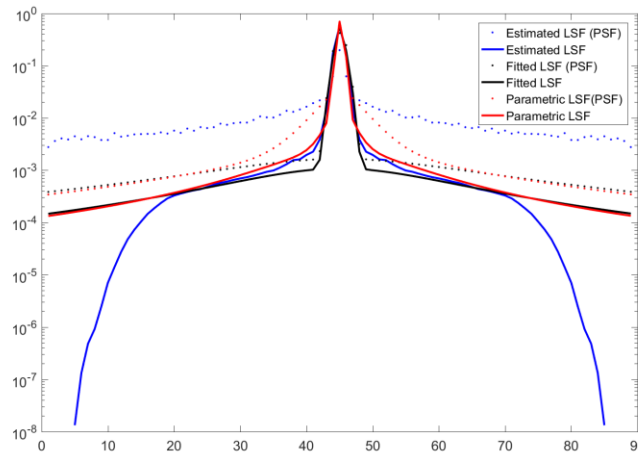
Figure 2-22 Comparison of LSF and PSF
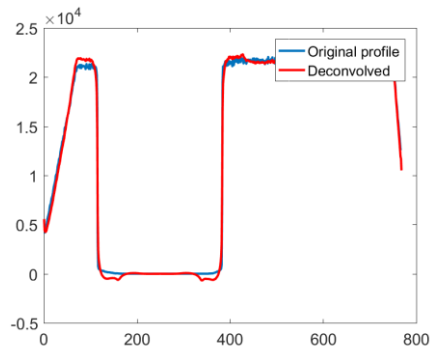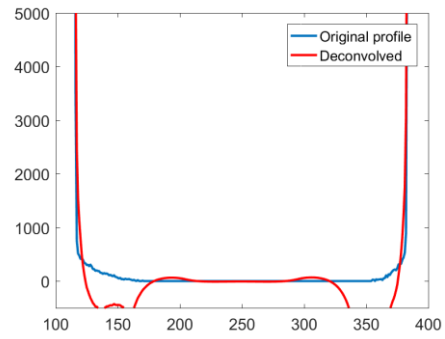
(a) deconvolved image   (b) region of interest
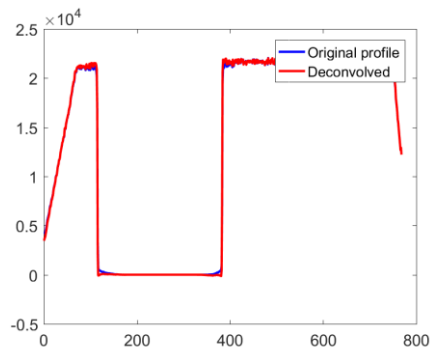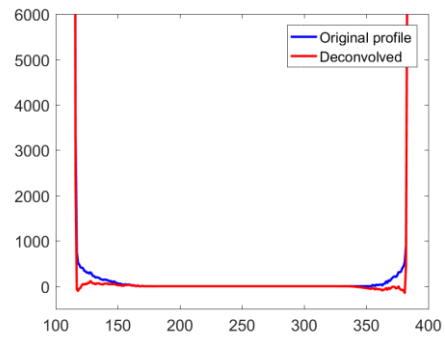
(c) deconvolved image   (d) region of interest
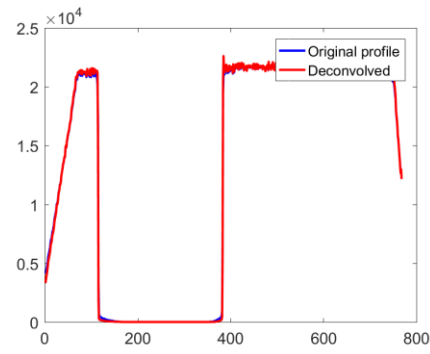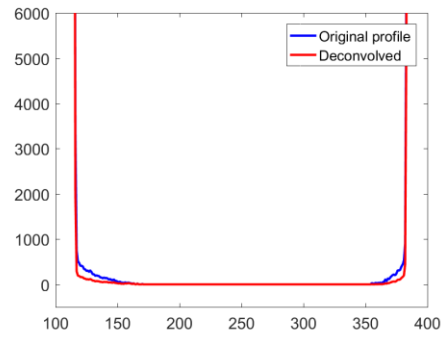
(e) deconvolved image   (f) region of interest

Figure 2-23 Comparison of profile after deconvolution

2.4.4 Conclusion

In this section, we investigated the deconvolution method to remove the detector response effect in the slanted-edge experiment. The PSF are derived from the slanted image using parametric model and then deconvolve the original projection image. Our results show

that the slanted-edge method is effective to derive LSF and PSF for the flat panel detector, and the deconvolution method can significantly eliminate the detector response effect.

The penumbra effect is magnified by the blocker, which is also an important effect for blurring the image. We also tried to get the PSF of the projection image from the moving blocker method. However, the width of the lead strips is too small to contain the full information of PSF. A blind-deconvolution method have been proposed and will be implemented to see the performance.

2.5 Summary

In summary, the results of reconstruction image and the CT number demonstrated that the moving blocker method can estimate the scatter signal in projection data, reduce the imaging dose, and simultaneously obtain complete volumetric information within the FOV. In the moving blocker methods, the signal detected in the blocked region is deemed scatter through an ideal blocking assumption and used to estimate scatter in the unblocked region. The image reconstructed by the scatter corrected projection data from the unblocked regions.

However, the accuracy of the scatter correction using the moving blocker method is limited by the detector response effect and the penumbra effect. Then we proposed several deconvolution methods to improve the accuracy of the scatter correction and implemented a simulation study. The results of the simulation demonstrated that the deconvolution method can be used to deblur the projected scatter image. To implement the deconvolution method, we proposed a slanted-edge experiment to derive the LSF and PSF using a parametric model. The results of the experiment showed that with good PSF estimation, the deconvolution method can significantly eliminate the detector response effect. Therefore, the moving blocker system with deconvolution method can generate high quality CBCT image. The high quality image can improve anatomical visualization and dose calculation accuracy in the treatment position, which are essential for the adaptive radiation therapy.

Chapter 3

Robust MB-SC for CBCT using multiple-view information

3.1 Introduction

Come-beam computed tomography (CBCT) is being widely used as an image guidance tool in radiation therapy nowadays. The quality of CBCT image is important to localize and delineate the tumor and to define relevant volumes when the patient is in the treatment position [1]. However, due to the use of the flat panel detector (FPD), the large amount of scatter signal deteriorates the projection images and greatly reduces the quality of CBCT images [38]. The manifest shading artifacts can lead to decreased image contrast and inaccurate CT number, which makes it difficult to contour the target and other volumes and to calculate the correct dose [34]. Therefore, scatter correction (SC) is critically important to overcome these problems of CBCT for a precise adaptive radiation therapy.

Different strategies have been investigated to correct the scatter contamination in CBCT projection data, e.g. suppression of scatter signal during the acquisition using anti-scatter grids [2, 39, 77, 78] and correction of scatter signal in projections using computational methods, such as analytical models or Monte Carlo simulations [3, 4, 47, 79-81]. There have been growing interests in developing measurement-based scatter correction, such as blocker-based methods [5-11, 53-55, 76, 82, 83]. These methods assume that the scatter is a low frequency signal and derive the scatter signal from the attenuator-blocked regions within the projection images, thus avoiding the computationally intensive Monte Carlo simulation [3, 77, 79, 84] or the oversimplification of analytical methods [4]. The fixed-blocker methods suffer the problems of the requirement of additional scans or the reduced imaging volume. The moving blocker method [10, 11] overcomes these limitations of fixed-blocker methods and is cable of simultaneously estimating the scatter signal and reconstructing the entire volume within the field of view (FOV) from a single CBCT scan. As an extra benefit, the radiation dose can be greatly reduced, e.g. by half if the same blocker width and pitch were used. The moving blocker method

was further advanced recently by a deconvolution method with an aim to improve the scatter signal estimation in the blocked regions by reducing the primary signal contamination [85]. Nevertheless, there are still a couple of issues with the moving blocker method, namely the large estimation errors in the regions with large scatter signal transition and/or insufficient scatter samples in the projection images (called "boundary effect" as follows) and the vulnerability to blocker detection errors (called "robustness" as follows). These errors can cause significant artifacts in corresponding regions in reconstructed images and possibly make them useless.

In our previous study [11], we constructed a moving blocker system to show the effectiveness of simultaneous SC and volumetric reconstruction [10]. The original moving-blocker SC method uses scatter measures in the blocked regions to estimate the scatter signal for unblocked regions for each individual projection view (which is called "single-view" SC method in the following context). Such a treatment has achieved much improved image quality and more accurate CT numbers compared to CBCT without SC in most cases. However, there are a couple of issues arose from the single-view SC method: 1) boundary effect: image slices near the boundary of the object that are deteriorated by severe artifacts because the scatter signal is changing fast in these regions which violate the low-frequency assumption of scatter signal or an extrapolation is needed when the blocked regions (scatter samples) do not cover one end of the axial FOV; and 2) robustness: the SC performance is prone to the blocked and unblocked region detection errors and thus the accurate blocker position is required for the success of the moving-blocker SC method. However, for CBCT projection data, especially for half-fan scan for a big-size object, it could be challenging to find the blocker edge because the projection image has very limited contrast at the phantom regions. The wrong edge detection can lead to unacceptable reconstruction results with severe artifacts. To address these issues and make the moving-blocker SC method for a wider and more robust application, in this study, we propose a multi-view SC method, which combines the adjacent projection views to jointly

estimate the scatter signal for the current projection view. As long as the projections are densely acquired around the object (e.g. 670 projections for a full 360° rotation used in this study), the scatter signal in adjacent projection views does not change much, because the angular difference among adjacent projection views is very small and the scatter signal contains little high-frequency information. We hypothesize that these adjacent projection views can provide complementary scatter signal in different regions along the rotation axis when the blocker is moving with the gantry rotation. Thus, a more accurate estimate of the scatter signal in large intensity transition regions can be achieved as the sampling rate is significantly increased (3~5 times depending on the number of adjacent views used). In order to overcome the adverse effect of the blocker detection errors, the estimated scatter from adjacent projection views can also be used for more accurate and robust edge detection in low contrast regions.

Both the Catphan phantom and an anthropomorphic pelvis phantom were used to test our multi-view SC method. We compared the quality of reconstructed images and CT numbers for different SC methods (no SC, single-view SC, and multi-view SC) using multi-detector CT (MDCT) images and CT numbers as a benchmark. This study aims to make the moving blocker-based SC method more robust and extend its effectiveness for the target near the boundary of the field of view or with sharp intensity changes in the projection images.

3.2 Methods and Experiments

3.2.1. Moving-blocker based SC method

The moving-blocker based SC method has been proposed to simultaneously estimate scatter signal and reconstruct the complete volume within the FOV from a single CBCT scan [10, 11]. A moving blocker system consists of several lead strips inserted between the X-ray source and the object. These lead strips are aligned perpendicularly to the gantry rotation axis and move back and forth along it while the source and detector rotating as shown in Figure 3-1. The method assumes that the blocked regions only receive the scatter signal, while the unblocked regions contain the sum of the primary and scatter signal ("total signal"). A flow chart

of the moving blocker scatter correction process is shown in Figure 3-2. As the scatter signal is generally a smooth low-frequency signal, the scatter signal in the unblocked regions can be estimated by interpolating the scatter signal in the blocked regions. Then the primary signal in the unblocked regions can be recovered by subtracting the estimated scatter signal from the total signal. As the blocker is moving along the gantry rotation axis, the missing data (in blocked regions) are different in different projection views, which is equivalent to a fewer view projection data acquisition, and the reconstruction can be effectively solved by the compressed sensing techniques. Accordingly, a total variation (TV) constrained iterative method can be used to reconstruct scatter corrected images for the full volume in the FOV [10, 16, 61, 86-89] Specifically, the discrete CBCT image of the linear attenuation coefficient μ is solved by minimizing the TV function $f(u)$:

$$\mu = \arg\min(f(\mu)), \tag{3.1}$$

$$f(\mu) = \sum_{x,y,z} \sqrt{\left(\mu_{x,y,z} - \mu_{x-1,y,z}\right)^2 + \left(\mu_{x,y,z} - \mu_{x,y-1,z}\right)^2 + \left(\mu_{x,y,z} - \mu_{x,y,z-1}\right)^2},$$

where x, y, and z are the three-dimensional coordinates of each voxel of the reconstructed image. Eq. (3.1) is enforced by the standard steepest descent algorithm and subjected to the data fidelity and the non-negativity constraints:

$$|A\mu - \tilde{p}| \leq \varepsilon , \tag{3.2}$$

$$\mu \geq 0 , \tag{3.3}$$

where $\tilde{p}$ is the log-transformed projection after scatter correction, A is the forward projection system matrix and ε is an error bound determined by the data noise and imaging model error. The constraint in Eq. (3.2) is enforced by the standard algebraic reconstruction technique (ART):

$$\mu_i^{(k+1)} = \mu_i^{(k)} + \lambda a_{ij} \left[\frac{p_j - \sum_i a_{ij}\mu_i^{(k)}}{\sum_i a_{ij}^2} \right], \tag{3.4}$$

where a_{ij} is the intersection length of projection ray j with pixel i, calculated by fast ray-tracing technique [63], k is the iterative step and λ is the relaxation factor. After each ART update of Eq.

(3.4), the resulting image was updated according to Eq. (3.1). More details of reconstruction can be found in Ref. [10, 11].
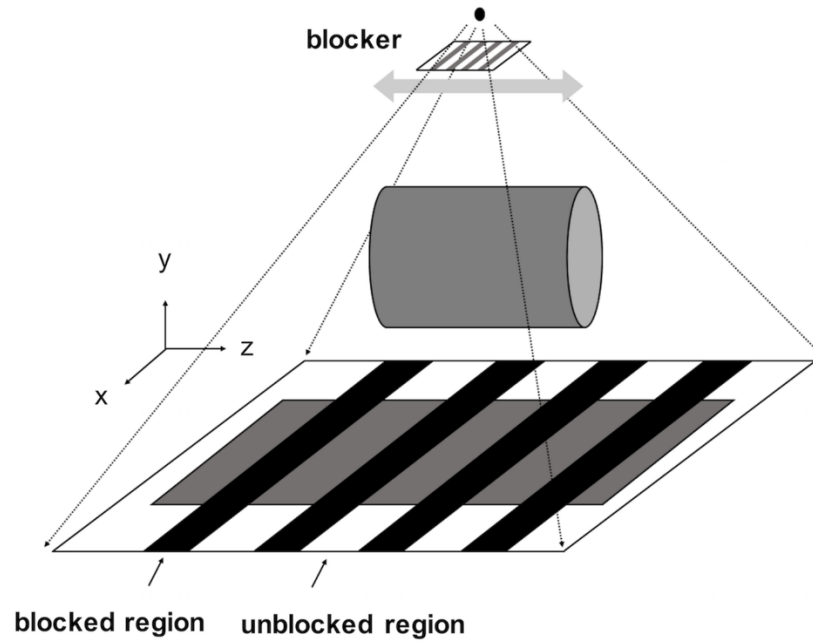
Figure 3-1 Moving blocker CBCT system

The rotational axis of the gantry is z and the blocker is moving back-and-forth in z direction. The blocked region detects the scatter signal and the unblocked region detects the total signal, i.e. the sum of the primary and scatter signals.
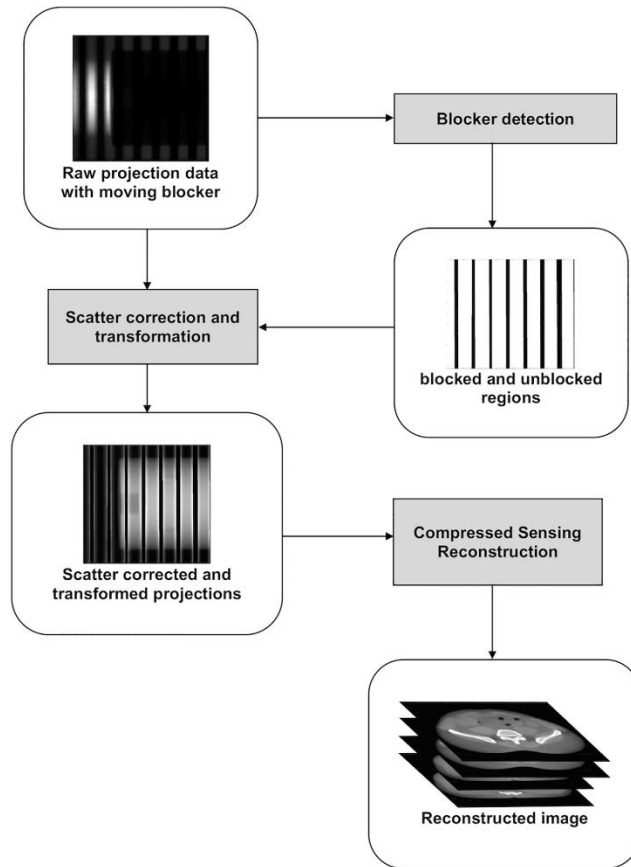
Figure 3-2 Work flow of moving blocker scatter correction

3.2.2. Issues with single-view moving-blocker SC method (SVSC)

A. Boundary effect

If the low-frequency smooth condition of scatter signal is violated, such as at the boundaries between the object and the air or between bone and soft tissues inside body where the scatter signal changes fast, the current scatter estimation method using a single projection view may cause scatter estimation errors in the unblocked regions. In the projection data of these regions, some views may contain accurate scatter information if they are blocked, while some views are lack of direct measurements as they are unblocked. For these (unblocked) views, the interpolation has to be applied to estimate the scatter signal. However, the limited sampling points in a single projection view are not sufficient to recover the transition of the

scatter signal. As shown in Figure 3-3 for a line profile of projection data of CatPhan (red line: true scatter signal; blue dots: sampling points from the blocked region; green line: estimated signal by cubic B-spline interpolation of blue dots), there are two kinds of problems due to the boundary effect. In region 1, the insufficient sampling points cause the interpolation to overestimate the scatter signal. In region 2, the extrapolation has to be used due to the lack of sampling points at the end and can introduce large estimation errors. Consequently, these significant scatter estimation errors will lead to inaccurate SC and severe artifacts in the reconstructed images.
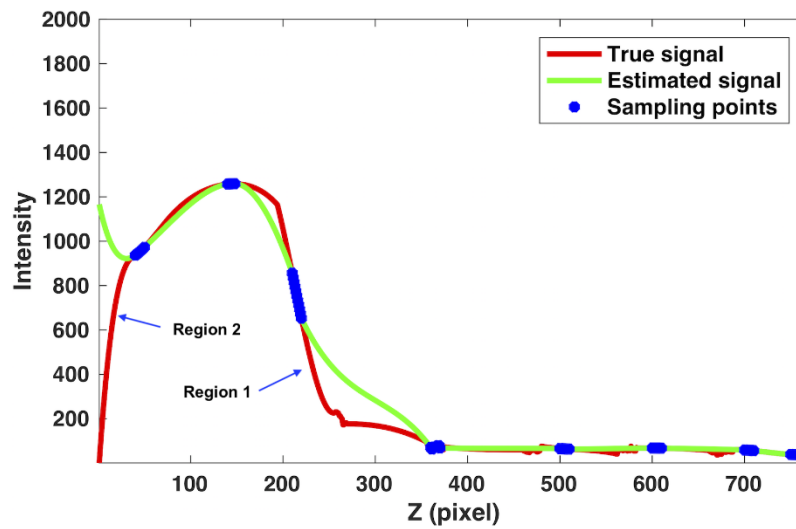
Figure 3-3 Boundary effect

The boundary effect is caused by the interpolation and extrapolation using limited sampling points in the single view SC (SVSC) method for the Catphan phantom.

B. Robustness

In the SVSC method, the blocker edges have to be determined for each view so that the blocked regions and unblocked regions can be separated for scatter estimation and reconstruction, respectively. Therefore, the success of the moving-blocker SC method highly depends on the accuracy of the detection of the blocker edges. Ideally, the edges of blockers

59

can be detected in each line profile along the z direction by intensity thresholding. However, this can cause erroneous detection in areas with low contrast. In practice, by assuming a straight line of the blocker edge, edge detection can be performed at two z lines to get the straight-line edge, so called "two-point method". This two-point method is easily achievable for a high contrast projection image (Figure 3-4 left), where two edge points far away from each other along one blocker edge. In Fig 4 left, the full-fan mode was used, suitable for the small size of the phantom (Catphan). Two points, one on the top and the other at the bottom, can be used to calculate the blocker edges and result in very accurate edge detection. In this case, both the true edges (solid red lines) and estimated edges (dashed red lines) overlapped with each other. However, when imaging a large-size object, the blocker edge detection can be erroneous due the large area of low image contrast (Figure 3-4 right). In Figure 3-4 right, due to the large size of the phantom (Pelvis phantom), the half-fan mode was used, and consequently only few rows on the top of the projection image provide sufficient contrast for reliable blocker edge detection as the bottom part's contrast is too low to identify the blocker edge reliably. Since the two edge points are too close, a little error can propagate along the rest part of the straight line and generate large blocker edge estimation errors (Figure 3-4 right, red dashed lines) from the true edges (Figure 3-4, red solid lines). This erroneous blocker edge detection caused by the two-point method can lead to artifacts in reconstructed images since both scatter signal and primary signal are estimated incorrectly.
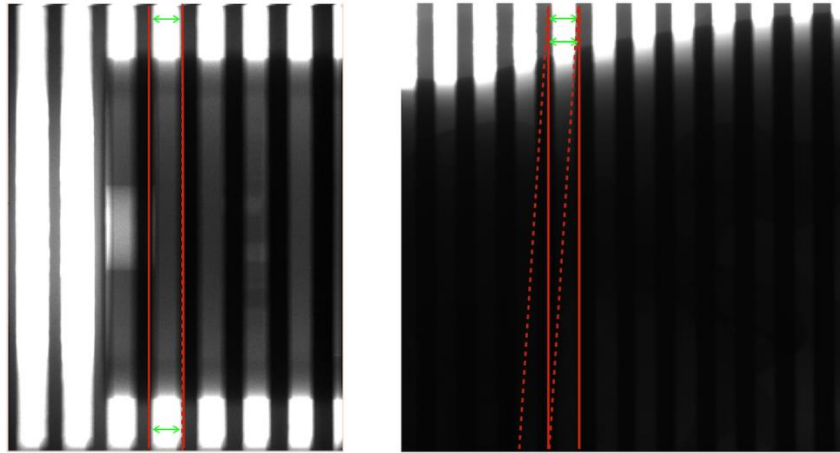
Figure 3-4 Blocker edge detection for a small object (left) and a large object (right).

The green arrows denote the position for reliable edge point detection in high-contrast regions. The edge is estimated as the line connecting two edge points. The red solid lines represent the true blocker edges and the red dashed lines are the estimated edges.

3.2.3 Multi-view moving blocker SC method (MVSC)

The multi-view SC (MVSC) method is proposed to address the issues with the single-view SC (SVSC) method using the moving blocker. The MVSC is to use adjacent projection views to jointly estimate the scatter for the current projection view. Should the angles be small among the neighboring projection views used for this joint scatter estimation, the change of the scatter profile can be negligible. The location change of the blocked regions in these projection views due to the axial blocker movement can be exploited to boost the sampling rate of the scatter signal, which is only sparsely sampled in the SVSC method due to the limited lead strip width and pitch of the blocker. As more samples are used for the interpolation of the scatter signal, more accurate scatter estimation can be achieved by MVSC than that by SVSC. This is particularly beneficial for the regions with large scatter signal transition. In addition, the complimentary scatter information from the neighboring views can be used to cross check for the wrong blocker detection and mitigate the scatter estimation errors. On the other hand, the

61

reconstruction process is kept intact in MVSC so that more accurate and robust reconstruction can be achieved through more accurate and robust scatter correction. The estimated scatter signal for ith projection view through interpolation can be expressed as:

$$S_i^{SE}(z) = \sum_{k=1}^{K} a_k W_k(z) \, , \tag{3.5}$$

where Wk(z) and ak are the basis functions and corresponding weights and the lateral dimension is omitted for clarity. The smoothness of estimated signal is enforced by the choice of the basis functions. In this work, the cubic B-spline functions were used. For the proposed MVSC method, the optimal weights can be found by minimizing the following least-squares objective function:

$$\mathbf{a}^* = \arg\min_{\mathbf{a}} \sum_{j \in \aleph(i)} \sum_{n=1}^{N} \left\| S_j^{SS}(z_{jn}) - \sum_{k=1}^{K} a_k W_k(z_{jn}) \right\|^2 \, , \tag{3.6}$$

where $\aleph(i)$ is the neighboring projection views for the ith view (including i), $S_j^{SS}(z_{jn})$ is the observed scatter signal in the nth blocked region of the jth projection view, and a is the vector of all weights ak. In this work, the third order polynomials were used for the basis functions Wk(z) and the weights ak were estimated using Newton's method. When $\aleph(i) = \{i\}$, the MVSC method is collapsed down to SVSC as only one projection image is used for the scatter estimation. In contrast, the MVSC method uses more than one projection image, e.g. $\aleph(i) = \{i-1, i, i+1\}$ if three adjacent views are used. The caveat is that these adjacent project views shall span only a small angle to avoid any significant scatter signal changes among these views. It is worth noting that the proposed multi-view scatter correction (MVSC) method still uses projections from a single rotation acquisition, thus the imaging dose and the acquisition time are the same as the single-view scatter correction (SVSC) method. Essentially, the MVSC method does not change the CBCT data acquisition of the SVSC method, using the same total number of projection views for reconstruction and scatter correction. The key difference of two methods is that the SVSC method uses only one projection view for scatter estimation, while the MVSC method uses several adjacent projection views for scatter estimation.

In addition, the scatter signal can be estimated from multiple projection views directly so that the wrong blocker edge detection (Figure 3-4) by the two-point method can be avoided. By composing the signal profiles from several neighboring views, the scatter profile can be readily estimated without the need of the blocker edge detection at first. The procedure is shown in Figure 3-5a-f with the signal profiles (vertical axis) along the axial direction (horizontal axis): 1) compare signal profiles from two adjacent views (blue and black lines in Figure 3-5a) and keep the lower signal in each position to get the derived signal profile (red line in Figure 3-5b); 2) compare the derived signal profile from the first step (black line in Figure 3-5c, same as red line in Figure 3-5b) with that from the third adjacent view (blue line in Figure 3-5c) and keep the lower signal in each position to get the derived signal profile (red line in Figure 3-5d); 3) repeat step 2) by comparing a couple of more adjacent views (Figure 3-5e) to get the final scatter profile (red line in Figure 3-5f) without detecting the blocker edges in the first place. Once the scatter signal (red solid line in Figure 3-5g) was estimated, an adaptive threshold (red dash line in Figure 3-5g) can be used to detect the blocker edges for the determination of the unblocked region, and then subsequent scatter correction and reconstruction. The fixed threshold (green dashed line in Figure 3-5g) derived from the mean of the intensity fails to detect all blocker edges in the cases, where the intensity profile has a large fluctuation. Note that the valley point detection using a single signal profile for scatter estimation is not reliable due to the large signal fluctuation and noise.
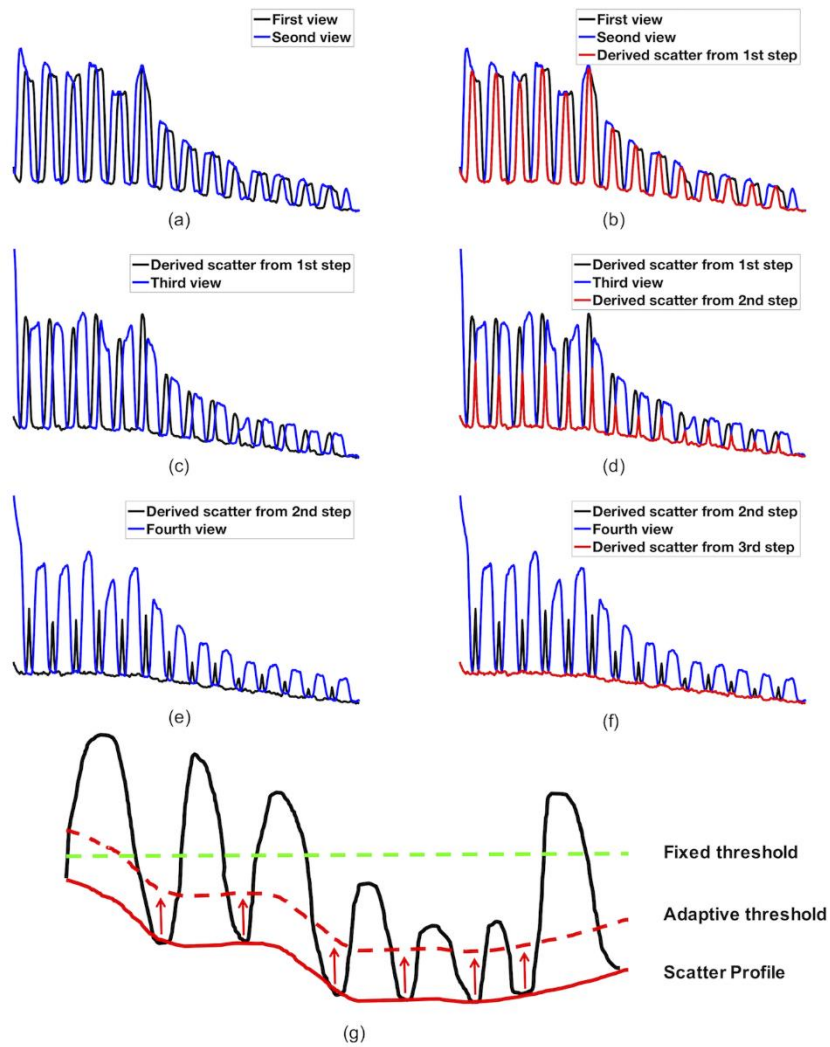
Figure 3-5 Multi-view scatter estimation and adaptive threshold

Figure 3-5 is showing an example of multi-view scatter estimation and adaptive threshold method for blocker edge detection. (a)-(f): the procedure to get the scatter profile (vertical axis) using the lowest signal in the signal profiles along the axial direction (horizontal axis) from multiple adjacent views (4 in this case); and (g) adaptive threshold (dashed red line) is derived from the scatter profile (red line) for more accurate and robust blocker edge detection, while the fixed threshold (green dashed line) fails to detect some edges in this case.

3.2.4 Experimental data and processing

To evaluate the MVSC method, we acquired the CBCT projection data of a commercial calibration phantom CatPhan® 600 (ThePhantom Laboratory, Inc., Salem, NY) using a Varian TrueBeam OBI system (Varian Medical Systems, Inc., Palo Alto, CA) (with a manual shift to mimic the moving blocker acquisition) and an anthropomorphic pelvis phantom CIRS 801-P (Computerized Imaging Reference Systems Inc., Norfolk, VA) using an Elekta Synergy XVI system (Elekta AB, Stockholm, Sweden) both with and without the moving blocker. The source-to-axis distance is 1000 mm and the source-to-detector distance is 1500 mm with a full 360° coverage in approximately 1 minute for the Varian TrueBeam OBI system. The source-to-axis distance is 1000 mm and the source-to-detector distance is 1536 mm with a full 360° coverage in approximately 2 minutes for the Elekta Synergy XVI system. There are 660~680 projection views acquired and each projection contained 512 × 512 pixels with a pixel size of 0.8 × 0.8 mm. We use full-fan scan for Catphan phantom (120kVp and 20 mA/10 ms) and half-fan scan for the pelvis phantom (120kVp and 80 mA/20 ms). The multi-detector CT (MDCT) (Philips Healthcare, Nevada, US) images of both phantoms were also acquired to serve as the evaluation benchmark.

The blocker is inserted between the x-ray source and the phantom and moves back and forth during CBCT gantry rotation. The moving blocker consists of equal-width lead strips embedded on a 3 mm thickness acrylic board (120 × 180 mm) are aligned along the detector face. The lead strips are 3.2 mm in thickness, 3.2 mm in width and are placed with a 3.2 mm pitch for the Catphan phantom and a 9.6 mm pitch (for boundary effect) and the 3.2mm pitch (for robustness) for the pelvis phantom. To investigate the performance of the MVSC method on the boundary effect, we used the both the Catphan data and the anthropomorphic pelvis phantom data. The pelvis phantom data was used to demonstrate the robustness of the MVSC method to the blocker detection errors (exist in most of the views) since it is more challenging to

detect the blocker edge for the half-fan scan of a large object (e.g. the pelvis phantom), while the full-fan scan of a small object (e.g. Catphan) is hardly a problem as detailed in Section 2.2.2 and Figure 3-4.

3.2.5 Evaluation metrics

To evaluate the performance of the different SC methods, we compare various reconstructed image slices of CBCT with SVSC and MVSC with the corresponding MDCT images, served as a gold standard. We also calculate the CT numbers in Hounsfield Unit (HU) in several regions of interest (ROIs) for a quantitative evaluation of reconstruction accuracy using different SC methods for the pelvis phantom data. Both the mean and standard deviation (STD) of CT numbers in the ROIs are presented. The overall accuracy in each ROI is measured by the root mean square error (RMSE) following the equation:

$$RMSE_{ROI} = \sqrt{\sum_{i=1}^{N}\left(CT_{CBCT}^{i} - CT_{MDCT}^{i}\right)^{2}/N}, \qquad (3.7)$$

where CT_{CBCT}^{i} and CT_{MDCT}^{i} denote the CT number of the ith pixel in the selected ROI for CBCT and MDCT, respectively, and N denotes the total number of pixels in the selected ROI.

3.3 Results

3.3.1 Scatter estimation and correction for the Catphan

Shown in Figure 3-6 are the typical estimated scatter signal profiles using the SVSC method (green line) and the MVSC method (red line) using adjacent five views along with the observed total raw signal (black line) for the Catphan phantom. The SVSC method using only the current projection view for scatter estimation overestimated the scatter signal for the unblocked region between 200 and 300 along the horizontal axis (green line), thus leading to the underestimated primary signal. The MVSC method corrected this overestimation by utilizing more sample points from adjacent projection views and led to more gradual scatter transition

(red line). It will be evident from the reconstructed images that this scatter estimation is more accurate.

In Figure 3-7, the projection images (the line integral of attenuation coefficients by taking logarithm of inversely normalized X-ray fluence) in a particular projection view are shown for: a) without moving blocker; b) SVSC; and c) MVSC. Severe bright strip artifacts can be observed in the unblocked region near the phantom boundary (the leftmost unblocked region, Figure 3-7b), where the overestimated scatter signal results in largely reduced primary signal, and thus much greater values of the line integral of attenuation coefficients. The MVSC method effectively eliminates these artifacts (the leftmost unblocked region, Figure 3-7c).

One transverse slice (first row) close to the phantom axial left boundary (Figure 3-8e, red dashed line) and one center coronal slice (second row) using different methods are shown in Figure 3-8. The reconstructed image without the moving blocker (Figure 3-8b, f) shows no significant artifacts, but suffers low contrast due to scatter shading effect, which is more obvious in the line profile of Figure 3-9. The overestimated scatter signal in the SVSC method results in severe streaking artifacts (Figure 3-8c), which is anticipated from the artifacts in the corresponding projection image (Figure 3-7b). These artifacts are effectively suppressed by the MVSC method using five adjacent views (MVSC, Figure 3-8d, h). The line profiles along the middle of the transverse slice of Figure 3-8 are shown in Figure 3-9. MVSC (red line) improved the contrast compared to that without SC (black line). However, SVSC (green line) suffers not only high noise due to the streaking artifacts, but also overcorrected CT numbers, especially for the center air part (30~50% less than -1000 HU). MVSC method significantly improved the contrast without introducing notable noise.
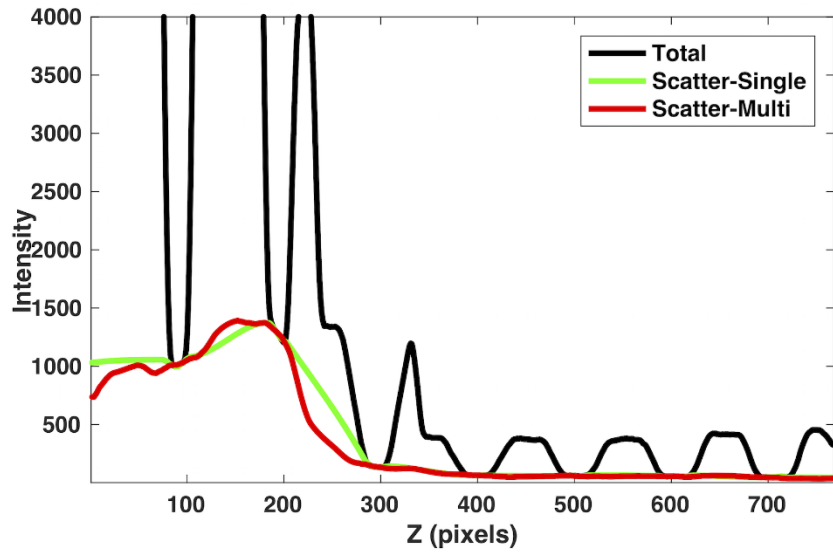
Figure 3-6 Comparison of profile

Figure 3-6 is showing the comparison of scatter signal estimated from the single-view scatter correction (SVSC) method (green line) and the multi-view scatter correction (MVSC) method (red line) for the Catphan phantom (3.2 mm pitch blocker). The observed total raw signal is in black.

(a)   (b)   (c)
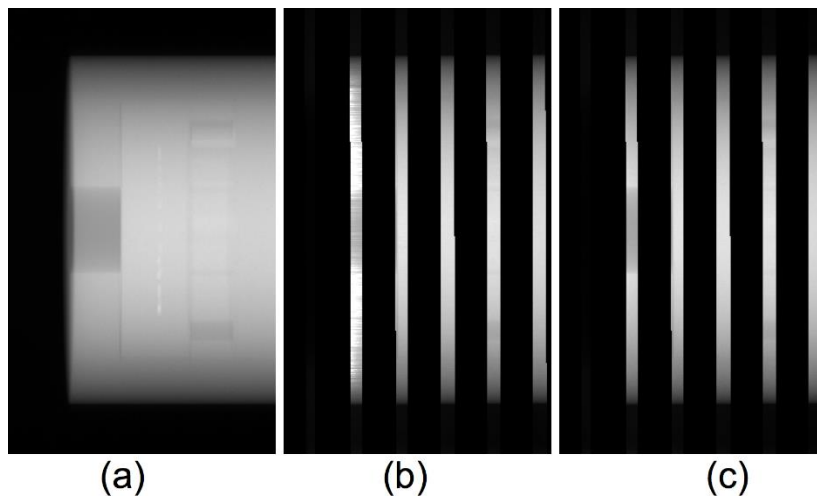
Figure 3-7 Projection images

Figure 3-7 is showing the projection images of the Catphan phantom (the line integral of attenuation coefficients by taking logarithm of inversely normalized X-ray fluence): a) without blocker; b) with SVSC; and c) with MVSC. Each image was normalized to its maximum intensity value, respectively.

(a)   (b)   (c)   (d)

(e)   (f)   (g)   (h)
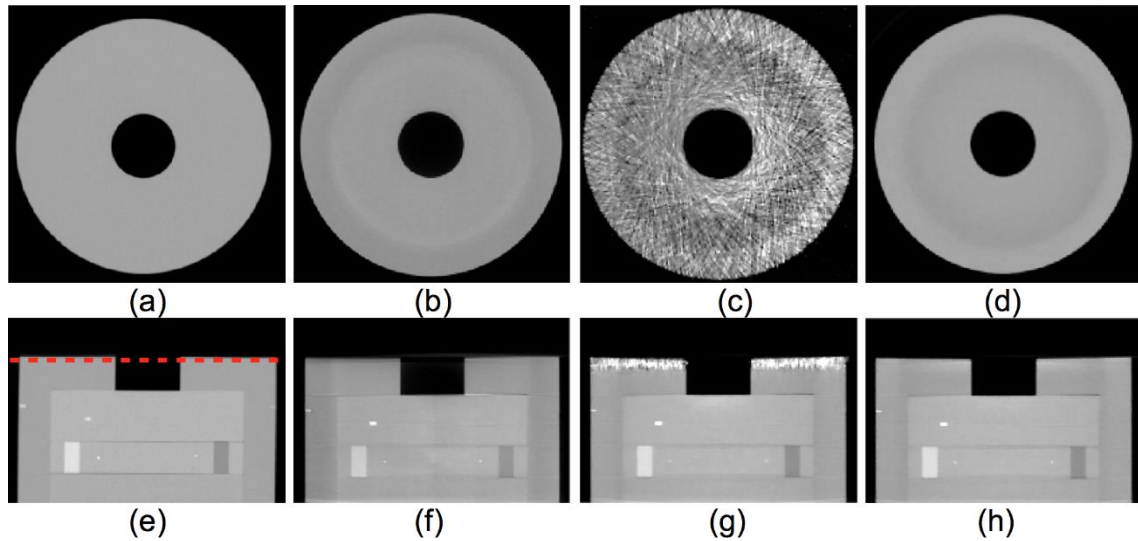
Figure 3-8 Reconstructed images

Figure 3-8 is showing the reconstructed images for CBCT of the Catphan phantom (close to the axial left boundary in Figure 3-7): (a, e) benchmark fan-beam MDCT; (b, f) without SC; (c, g) SVSC; and (d, h) MVSC. The red dashed line in (e) labels the transverse slice location. The difference between without SC and MVSC can be better discerned through the line profiles in Figure 3-9. (Display window [−900, 500] HU)
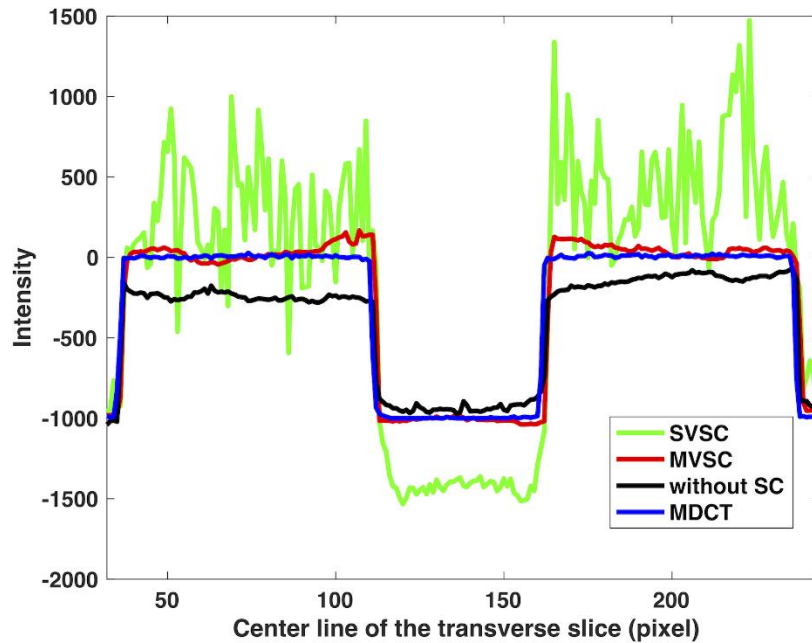
Figure 3-9 Line profile

Figure 3-9 is showing the line profile through the middle line of the transverse slice in Figure 3-8. The middle part is air and the CT number should be around -1000.

3.3.2 Scatter estimation and correction for the Pelvis phantom

A. Boundary effect

Figure 3-10 shows the estimated scatter profiles in one row of a projection image using the SVSC method (green line) and the MVSC method using 5 adjacent views (red line) along with the observed total signal (black line) for the pelvis phantom. The scatter signal is underestimated for the SVSC method in the leftmost unblocked region due to the lack of scatter signal samples to the left. The similar erroneous scatter estimation is also observed for other rows in the same projection image as well as other projection images in this region.

In Figure 3-11, two transverse slices (the top and middle rows) and one coronal slice (the bottom row) are shown for MDCT (Figure 3-11a, e, i), CBCT without SC (Figure 3-11b, f, j), CBCT with SVSC (Figure 3-11c, g, k), and CBCT with MVSC (5 views) (Figure 3-11d, h, l) from

left to right (display window [-600 800] HU). The locations of the transverse slices are labeled as the red dashed lines 1 and 2 on the coronal slice of MDCT (Figure 3-11i). The scatter shading artifacts, especially at the central soft tissues, can be seen in CBCT without SC (Figure 3-11b, f, j) and lead to greatly reduced image contrast. The erroneous scatter estimation at the boundary can introduce severe streaking artifacts for the slices in these regions in the reconstructed image with SVSC as shown in Figure 3-11c. The proposed MVSC method effectively eliminates these artifacts and largely recovers the image contrast lowered by scatter contamination in CBCT (Figure 3-11d). For both SVSC and MVSC, the middle transverse slices (Figure 3-11g and 11h) show improved contrast compared to CBCT without SC. In addition, the MVSC image (Figure 3-11l) seems to be less noisy than the SVSC (Figure 3-11k) in the coronal view. Note that achieving a larger FOV of MVSC at the same radiation dose of SVSC is clinically significant.
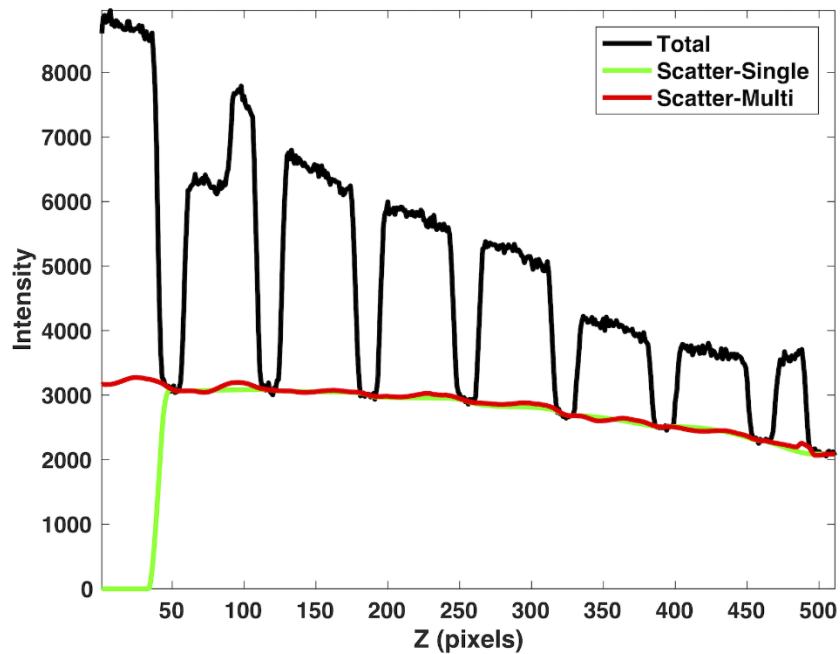
Figure 3-10 Comparison of profiles

Figure 3-10 is showing the comparison of the scatter signal profiles estimated from SVSC (green line) and MVSC (red line) when the left marginal region is lack of scatter samples for the anthropomorphic pelvis phantom (9.6 mm pitch blocker). The observed total signal is in black.
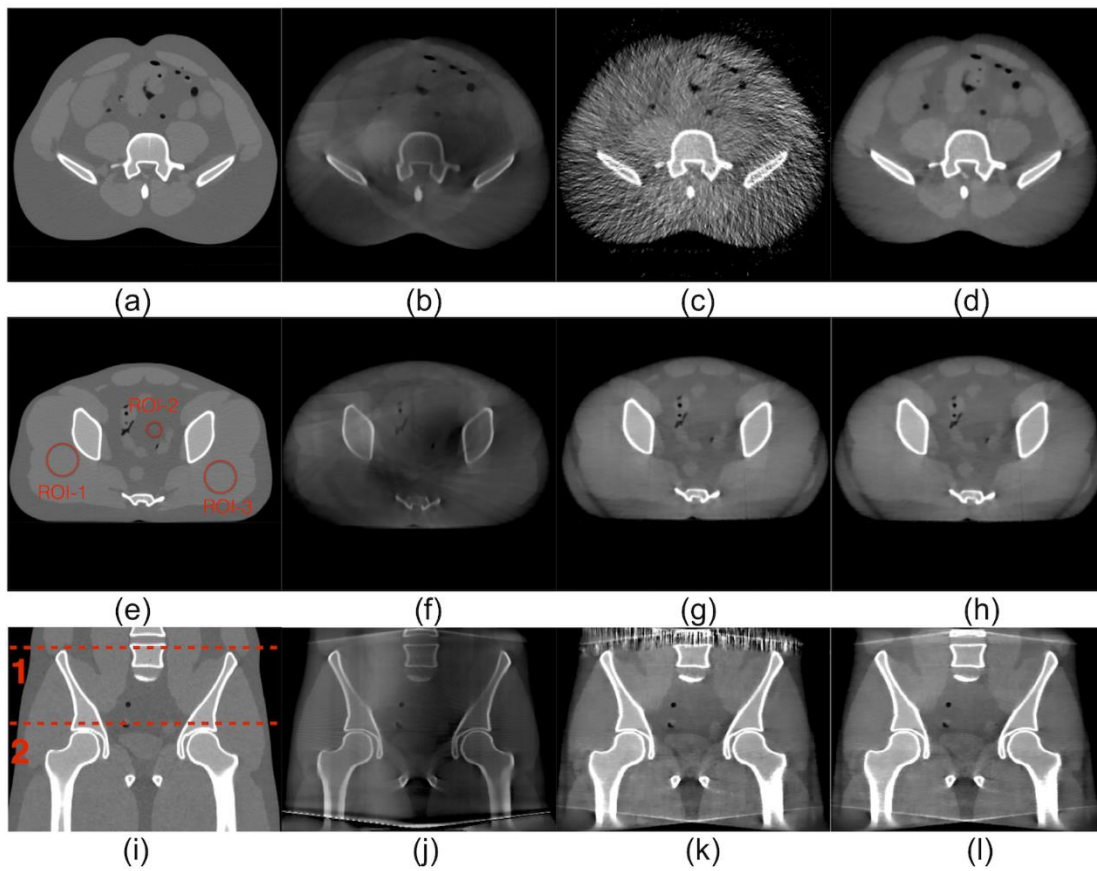
Figure 3-11 Reconstruction images

Figure 3-11 is showing the reconstruction results. Edge effect: two transverse slices (in the top and middle row) and one coronal slice (in the bottom row) of the anthropomorphic pelvis phantom. First column (a, e, i): MDCT; second column (b, f, j): CBCT without SC; third column (c, g, k): CBCT with SVSC; fourth column (d, f, l): CBCT with MVSC. The locations of the transverse slices are labeled in (i) (1 for the top row and 2 for the middle row). Regions of

interest (ROIs) labeled in (e) were used for measuring the reconstruction accuracy quantitatively. (Display window [−600, 800] HU)

The mean and standard deviation (STD) of CT numbers in the ROIs delineated in Figure 3-11e are shown in Table 3-1 as well as the RMSE values between different CBCT reconstructions (without SC (WOSC), SVSC, and MVSC) and MDCT. Both SVSC and MVSC greatly reduce the bias (the deviation of the mean from that of MDCT) in all ROIs (with only a little STD increase in ROI-1 and ROI-3). Consequently, the RMSE values are largely reduced from 379 (WOSC) to 29 (SVSC) and 29 (MVSC) for ROI-1, from 304 (WOSC) to 32 (SVSC) and 31(MVSC) for ROI-2, from 305 (WOSC) to 35 (SVSC) and 34 (MVSC) for ROI-3. These results demonstrate that MVSC not only eliminates the artifacts caused by the lack of scatter signal samples in the boundary region, but also maintains the superior scatter correction performance of the original SVSC method for the other regions.

Table 3-1 Comparison of the CT number (HU) of three ROIs

	ROI-1			ROI-2			ROI-3		
	Mean	STD	RMSE	Mean	STD	RMSE	Mean	STD	RMSE
MDCT	72	15		-48	18		70	19	
WOSC	-308	23	379	-348	47	304	-234	19	305
SVSC	71	26	29	-46	30	32	67	35	35
MVSC	71	26	29	-44	29	31	71	34	34

B. Robustness

Figure 3-12 shows one estimated scatter profile using the SVSC method (green solid line) and the MVSC (5 adjacent views) method (red solid line) along with the observed total signal (black line). The erroneous blocker edge detection in one projection view caused that the signal in the unblocked regions was counted as the scatter signal. It thus introduced large errors in the estimated scatter signal by the SVSC method (green solid line in Figure 3-12). In contrast, if the neighboring views are taking into account, the MVSC method can utilize signal profiles from these views to robustly estimate the scatter signal as shown as red dashed line in Figure 3-12 without the need of blocker detection. It is important to note that the MVSC method can

utilize the derived scatter profile to generate adaptive threshold (red dashed line) and to achieve more accurate edge detection. Thus, the primary signal in unblocked regions can be recovered more reliably.

Two transverse slices (the top and middle rows) and one coronal slice (the bottom row) are shown in Figure 3-13 for MDCT, SVSC, MVSC (using five adjacent views) from left to right (display window [-600 800] HU). The locations of the transverse slices are labeled as the red dashed lines 1 and 2 on the coronal slice of MDCT. Both primary signal and scatter signal estimation errors in SVSC resulted in severe streak artifacts and underappreciated contrast (Figure 3-13b, 13e, 13h). The MVSC (Figure 3-13c, 13f, 13i) effectively corrected such errors and greatly improved the image quality with less streaking artifacts and enhanced contrast. It is noted that this set of data using the small pitch value (large spatial sampling rate) so that the boundary effect has been avoided.
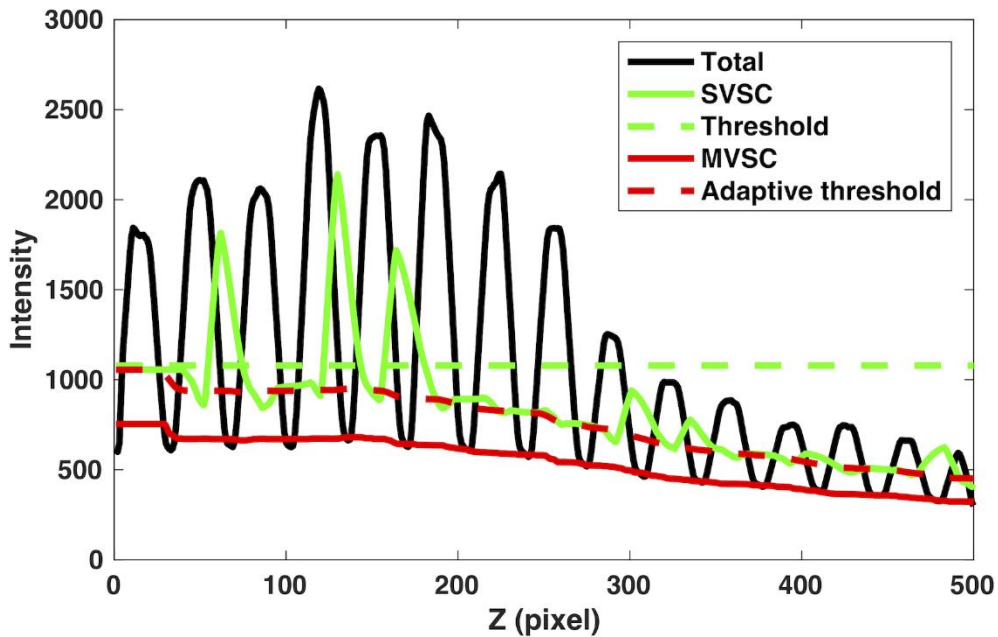
Figure 3-12 Comparison of profiles

Figure 3-12 is showing the comparison of scatter signal profiles estimated from SVSC (solid green lines) and MVSC (solid red lines) when the blocker edge detection error occurs for the anthropomorphic pelvis phantom (3.2 mm pitch blocker). The red dashed line and green dashed line are the derived adaptive threshold and the fixed threshold (mean of the profile) for blocker detection, respectively. The observed total signal is in black.
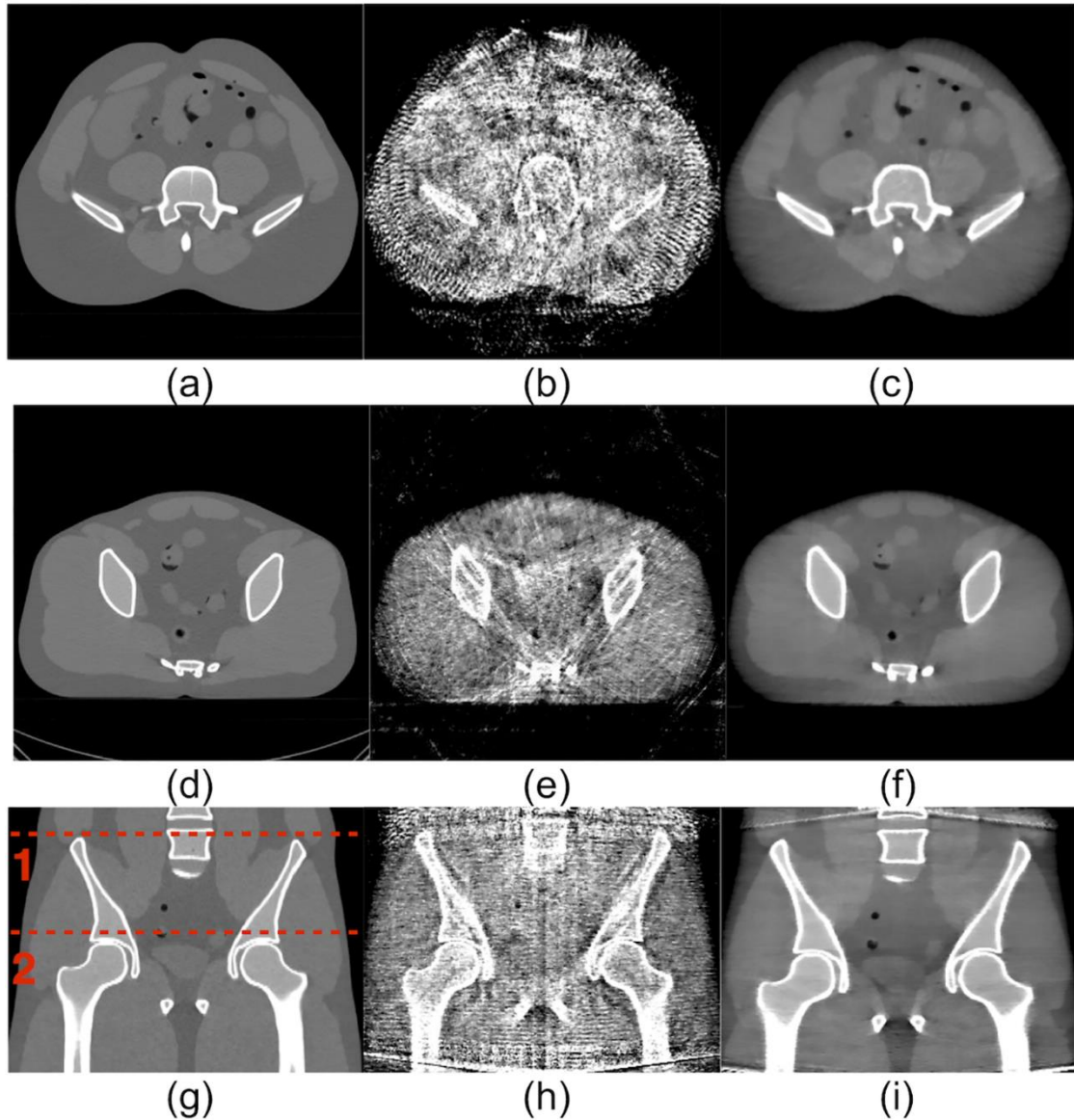
Figure 3-13 Reconstruction images

Figure 3-13 is showing the reconstruction results. Robustness: two transverse slices (in the top and middle row) and one coronal slice (in the bottom row) of the anthropomorphic pelvis phantom. First column (a, d, g): MDCT; second column (b, e, h): CBCT with SVSC; third column (c, f, i): CBCT with MVSC of five adjacent views. The locations of the transverse slices are labeled in (g) (1 for the top row and 2 for the middle row). (Display widow [−600, 800] HU)

3.4 Discussion

In this study, we investigated the scatter estimation errors caused by single-view SC (SVSC) used in the moving-blocker SC method for the regions with fast scatter signal changes or lack of scatter samples and the blocker detection errors. To make the moving blocker SC method suitable for these regions and robust to the blocker detection errors, we proposed a multi-view SC (MVSC) method using several neighboring views.

The scatter estimation and corresponding reconstruction results show that the MVSC method can eliminate the scatter estimation errors in the regions with fast scatter signal changes (Figure 3-6) or lack of scatter samples (Figure 3-10) and maintain the superior scatter correction performance for other regions (Table 3-1). In the regions with fast scatter signal changes or missing scatter samples at the margin, the scatter signal is hard to be recovered accurately with limited sampling points by using just one projection view in SVSC. The MVSC method uses the adjacent projection views, which can provide more information of the scatter signal in different locations along the blocker moving direction because of the blocker movement during the gantry rotation. The scatter signal is recovered more accurately with the MVSC method and result in a reconstructed image with reduced artifacts and more accurate quantitative results (CT numbers).

Furthermore, the accurate blocker detection is required in SVSC not only for accurate scatter signal estimation in the blocked regions, but also for the accurate primary signal estimation in the unblocked regions. However, the blocker detection error may occur in certain views, especially for large objects where the projection image contrast is low. A robust blocker

76

edge detection and scatter estimation method is in need to improve the clinical translation of the moving-blocker SC method. The proposed MVSC method can use multi-view information to achieve accurate scatter profile estimation without edge detection at first. Consequently, the estimated scatter profile can be used for an adaptive thresholding for more accurate and robust edge detection for primary signal estimation, thus leading to much improved reconstruction image quality. In order to make the proposed method work as shown in Figure 3-5, the detected scatter signal from several adjacent projection views shall not have much difference and must overlap with each other, which is often the case for a slow moving blocker with a small pitch.

The number of adjacent projection views that can be used in the MVSC methods was also investigated in this study. For the data acquired in this study, if the angle spanned by the adjacent views is less than 3º (corresponding to maximum 5 adjacent views in a 0.5 º gantry angular sampling), negligible scatter difference is observed among the adjacent projections and leads to superior MVSC performance as shown in Figure 3-11, Figure 3-13 and Table 3-1. As more adjacent views were used, the MVSC performance deteriorates due to the increased discrepancy of the scatter signals in these views. The optimal blocker pitch and speed were investigated in another study for SVSC [90] and will be further studied for MVSC in future.

In this study, we mainly focus on improving the conventional moving blocker method and compare between SVSC and MVSC. Although it would be an interesting topic to investigate the performance of different SC methods, such as analytic modeling and Monte Carlo simulation, it is out of the scope of this work. To shed light on how the moving blocker based method compared to the clinical routine, kernel-based scatter correction (K-SC) used on Varian TrueBeam OBI (125kVp, 60mA/20ms) and uniform scatter correction (U-SC) used on Elekta XVI (120 kVp, 40 mA/40 ms), we show a set of images in Figure 3-14. (At this point, the moving blocker can be only mounted on the Elekta system). All these images have less shading artifacts than that without SC (Figure 3-11(j)). The proposed MVSC method and the K-SC method outperform the U-SC method. The images from Varian using K-SC seem to have better

contrast than MVSC on Elekta, partially due to the use of anti-scatter grid and additional image processing employed by Varian OBI, such as analytical beam hardening correction, additional noise suppression technique and ring artifacts correction [46, 91, 51]. More importantly, heavier spatial regularization is deployed in the MVSC method to alleviate the missing data problem caused by ~50% of the incident X-ray blocked by the moving blocker in this example. The MVSC method is indeed beneficial to the patient since the radiation dose is greatly reduced. With additional image processing and increased mAs to compensate the loss of the detected photon flux due to the blocker (without increasing the radiation dose), it is envisioned that the MVSC method can produce comparable images to Varian with K-SC, if not better. Nevertheless, the shading artifact is effectively removed in both Varian with K-SC and the proposed MVSC method as shown in the line profiles of Figure 3-15.
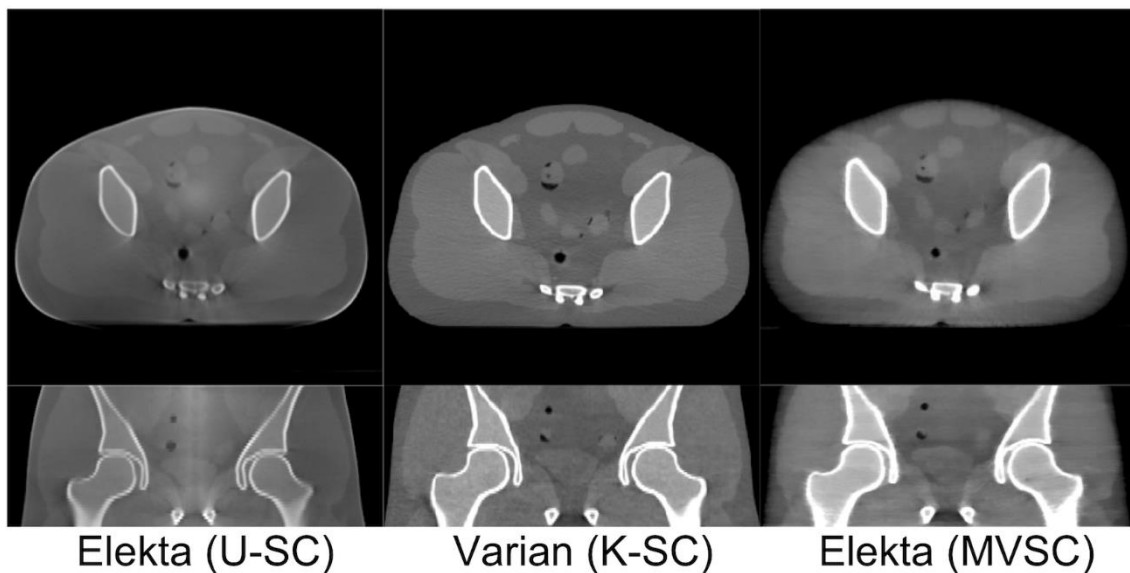
Figure 3-14 Comparison of different SC method

Figure 3-14 is showing the comparison between the proposed MVSC method and the clinical SC methods (U-SC: uniform scatter correction; K-SC: kernel-based scatter correction).

78
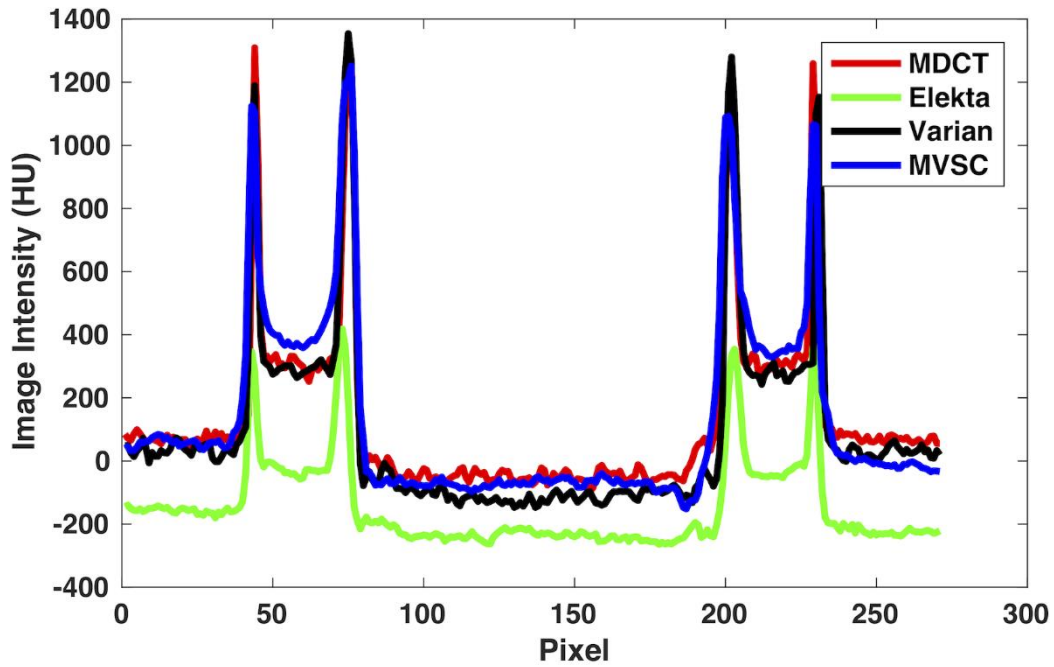
Figure 3-15 Comparison of line profile

Figure 3-15 is showing the comparison of the horizontal line profile (red line in Figure 3-14) for Elekta with U-SC, Varian with K-SC and MVSC. The MDCT profile serves as the ground truth.

Finally, the MVSC method is performed in the projection domain. The increased computational time due to use of multiple views instead of a single view is negligible compared to the reconstruction time. Thus, it is a practical SC method in terms of the computational complexity.

3.5 Conclusions

The results from the phantom studies show that the proposed MVSC method allows the moving blocker SC method to estimate the scatter signal more accurately in the regions with fast scatter signal changes or lack of scatter samples in the current view and to correct blocker detection errors caused by the two-point method. This development will expand the utility of moving blocker-based SC for the target with sharp intensity changes in the projection images and make it more robust to blocker detection errors. The further investigation is planned to test the MVSC method on the phantoms, such as the chest and the head, where the bone/lung and body/air interfaces may manifest its benefit.

Chapter 4

4D CBCT with a moving blocker

4.1 Introduction

X-ray Cone-beam computed tomography (CBCT) has been widely used in radiation therapy for image-guided radiation beam delivery with accurate tumor localization and holds the potential for calculation of the actual dose on the treatment day for an adaptive therapy [1]. Since there are multiple fractions in each treatment course and CBCT scan may be repeatedly conducted at each treatment fraction. Lowering the radiation dose of CBCT, while maintaining or improve image quality, is important to realize the full potential of CBCT as the repetitive ionization radiation becomes a concern for patients [92, 93].

New data acquisition strategies combined with hardware and software advances have been vigorously pursued and shown the great potential to substantially lower the CT radiation dose without compromising the image quality [94-96]. There are two main strategies for CT dose reduction in data acquisition: 1) the X-ray flux reduction by lowering the operating current, potential and exposure time of an X-ray tube, which have been adapted in some clinical practices; and 2) the sparse sampling including fewer projection views, limited coverage angle, and interior scan, which are still in active research stage. They could also be combined to achieve the maximum dose reduction. In 4D CBCT for radiation therapy, CT numbers for dose calculation and the tumor location and motion for beam delivery are of clinical interests. The performance of these clinical tasks, different from diagnostic purposes, may be well maintained even if the dose reduction, such as sparse sampling, is applied. In this work, in addition to dose reduction using fewer projection views, a moving blocker inserted between the X-ray source and the imaging subject, whose main purpose is to achieve the measurement based scatter correction, can lead to the subsampling in each projection view for further radiation dose reduction. To our best knowledge, this is the first study to investigate dose reduction potential

through subsampling of both the view numbers and the projection images, particularly for 4D CBCT.

There are many factors that deteriorate the CBCT image quality. The inferior image quality as compared to the planning multi-detector CT (MDCT) becomes the major hurdle for CBCT to fulfill aforementioned dose calculation tasks. Among them, scatter is one of major problems due to the use of large-area flat panel detector (FPD). Various scatter correction (SC) methods have been proposed to address this problem and achieved notable success. These methods generally fall into three categories: 1) hardware scatter suppression methods, e.g. anti-scatter grids [2, 39, 77, 78]; 2) computational methods, either analytical modeling or Monte Carlo simulation [3, 4, 47, 79-81]; and 3) measurement-based methods using various kinds of blockers or modulators [5-11, 53-55, 76, 82, 97, 98]. Although there is lack of a comprehensive comparison of these SC methods, using moving-blockers between the X-ray source and the image subject has achieved excellent SC performance with one conventional CBCT scan, which can reduce the CT number error less than 100 HU, satisfying less than 2% dose calculation error requirement [97]. An added benefit of use of the moving blocker is that the blocked X-ray intensity effectively reduced the radiation exposure to the patient as aforementioned subsampling of each projection image.

Another degrading factor for CBCT is the patient motion since the acquisition speed is not fast enough to yield motion-frozen images with complete data. This is particular troublesome for the radiation therapy of lung cancer as the respiratory motion can be as high as 40 mm along superior-inferior direction and 20 mm along anterior-posterior direction [99, 100]. If only one 3D CBCT volume image was reconstructed from the whole data, the motion blur would introduce severe artifacts in the reconstructed image. It has been shown that respiratory motion gated 4D CBCT can greatly reduce these artifacts and improve image quality [12, 13, 15, 21, 101, 102]. Furthermore, 4D CBCT provides an opportunity to generate a tumor motion-of-the-day model right before each treatment fraction for a more precise treatment than using a

universal motion model. Motion-compensated 4D reconstruction methods have been actively pursued to yield a series of images depicting tumor motion [17, 21, 103-117]. Among them, a simultaneous motion estimation and image reconstruction (SMEIR) algorithm has been shown to yield high-quality respiratory phase images and a tumor motion model [21]. Nevertheless, the scatter problem has not been addressed in these previous studies, although some computational methods may be adapted [84].

In this work, we propose to use moving blockers in a respiratory motion gated 4D CBCT acquisition and to develop an effective reconstruction method. This work is founded on our previous developments on moving blocker SC for 3D CBCT [10, 11, 97] and SMEIR for 4D CBCT [21]. In this novel imaging method, there are two challenges for the highly incomplete data reconstruction: 1) for each of total K phases of a respiratory cycle, there are only approximately 1/K^{th} projection views are available for reconstruction; and 2) for each projection view, the data is not complete (i.e. partially blocked). By adapting the techniques of compressed sensing reconstruction, motion-compensated reconstruction (particularly SMIER in this study), and moving-blocker based SC, we develop a 4D moving-blocker (4D-MB) CBCT method that can overcome these challenges and serving both dose reduction and scatter correction purposes. In this feasibility study of the proposed 4D-MB CBCT method, we demonstrated that high quality 4D images could be reconstructed at substantially reduced radiation dose (30% lower) with much reduced scatter artifacts using both non-uniform rotational B-spline-based cardiac-torso (NCAT) [118] phantom simulation and pseudo-real patient data.

4.2 Methods

4.2.1 Moving-blocker based 4D (4D-MB) CBCT acquisition

The moving-blocker based 4D (4D-MB) CBCT acquisition is illustrated in Figure 4-1 (transverse view). A blocker made of parallel lead strips is placed between the X-ray source tube and the image subject and holds in the plane parallel to the FPD plane. During the data acquisition, the blocker is moving along the axial direction (perpendicular to the plane shown in

Figure 4-1) as the gantry rotates around the subject (more details about moving blocker setup can be found in our previous work [10, 11, 97]). In the meantime, the projection data is binned with respect to different phases of the respiratory motion of the subject based on the motion amplitude gating. Therefore, at any projection angle, the projection data corresponding to a particular respiratory phase is partially blocked (determined by the blocker position). Given non-synchronized respiratory motion and blocker motion, for each phase, the projection views are sparse around the subject with each projection data randomly sampled as lateral strips locate at different positions. Both compressed sensing techniques, e.g. total variation (TV) constraints exploiting the image gradient space sparsity, and motion-compensated reconstruction techniques, such as SMEIR, utilizing the temporal correlation can be adapted to reconstruct 4D images using these highly undersampled data.

The blocker serves two purposes here: 1) to provide scatter information in the blocked region; and 2) to lower the radiation dose by blocking substantial amount of X-ray flux. As long as the movement of the blocker is not synchronized with the respiratory motion so that the sampling data for each respiratory phase will randomly span the whole projection domain, which can be effectively reconstructed by compressed sensing techniques. In addition, the scatter signal can be estimated from the blocked regions. Thus, the primary signal in the unblocked regions for scatter-corrected reconstruction can be recovered by subtracting the scatter signal from the total signal. As we showed in our previous work [8], TV-based iterative reconstruction can effectively suppress the scatter artifacts and produce high-quality CBCT images using the primary signal only in the unblocked regions. It is important to note that the proposed 4D-MB will have much less projection data for each 3D phase volume compared to moving-blocker based 3D CBCT (3D-MB). Indeed, if the number of respiratory phases is K, the projection views for each phase in 4D-MB are only approximately $1/K^{th}$ of 3D-MB. The temporal redundancy must be taken into account to maintain high quality reconstruction. As a proof of concept study, we

will adapt our previously developed SMEIR method [21], although other motion-compensated reconstruction methods can be equally applied [17, 103-114].
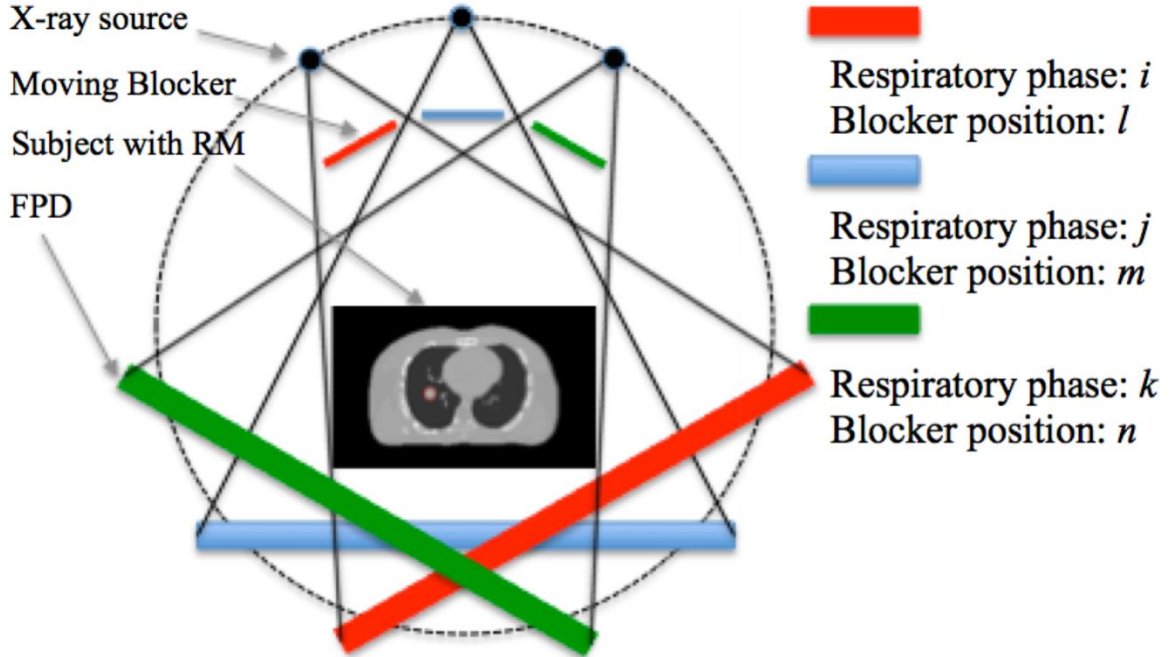
Figure 4-1 MB based 4D CBCT with respiratory gating (transverse view).

Figure 4-1 is showing the moving-blocker based 4D CBCT with respiratory gating (transverse view). Different colors of blockers and FPDs denote that the projection data at a particular angle (view) is a combination of a particular respiratory phase and a particular blocker position. (RM: respiratory motion; FPD: flat panel detector. Illustration only, not to scale.)

4.2.2. Scatter correction and image reconstruction

From Figure 4-1, we have the total signal received at phase k of a respiratory motion gated acquisition (of a total of K phases) as follows,

$$S_k^{Total} = S_k^{Primary} \sum_{i=1}^{B} \prod_i + S_k^{Scatter}, \qquad k\text{=1, 2, ..., } K, \quad (4.1)$$

where the element of $S_k^{Primary}(j) = I_0 e^{-\int_{L_j} \mu_k(x,y,z)dl}$ is the primary signal detected in the detector

bin j from an incident source intensity I_0 through the ray path L_j, $\prod_i$ is the ith rectangle

window function (1 inside and 0 outside) for i=1, 2, …, B blockers, $S_k^{Scatter}$ is the scatter signal

and S_k^{Total} is the total signal that is the sum of the primary and scatter signals. The scatter

signal $S_k^{Scatter}$ can be determined from the blocked regions and then be interpolated and

subtracted from the total signal S_k^{Total} to recover the primary signal $S_k^{Primary}$ in the unblocked

regions. Afterward, the normalized logarithm can be taken on the estimated primary signal

$S_k^{Primary}$ to obtain line integrals p_k to have the following linear forward projection model,

$$p_k = A_k \mu_k, \text{ for } k\text{=1, 2, …, } K, \quad (4.2)$$

where A_k is the projection matrix for phase k, whose element is the intersection length of a

particular voxel with the ray reaching a particular detector bin. Note that A_k is different for

different phases due to different view angles and blocker positions. The phase-by-phase 3D

reconstruction can be achieved by using constrained TV minimization,

$$\mu_k^* = \arg\min_{\mu_k} \|\mu_k\|_{TV} \text{ , s.t. } \|A_k \mu_k - p_k\|_2^2 \le \varepsilon \text{ , for } k\text{=1, 2, …, } K, \quad (4.3)$$

where $\|\mu_k\|_{TV} = \sum_{x,y,z} \sqrt{(\mu_{x,y,z} - \mu_{x-1,y,z})^2 + (\mu_{x,y,z} - \mu_{x,y-1,z})^2 + (\mu_{x,y,z} - \mu_{x,y,z-1})^2 + \delta}$ with a

small constant δ (10^{-6}) to avoid zero in the denominator in the gradient of TV and ε is an error

bound for the quadratic data fidelity constraint. The alternated update methods can be used to

solve Eq 4.3, i.e. the data fidelity enforced by simultaneous algebraic reconstruction technique

(SART) [17] and the TV minimization achieved by the steepest descent method (with an initial

step size of 0.2 and a relaxation factor 0.8) [21] are optimized in an interleaved fashion to

update μ_k. However, this phase-by-phase 3D reconstruction will suffer from substantially

undersampled data and can be improved by 4D reconstruction that utilizing the motion correlations among the phase volumes.

If a motion model is available to describe the transformation from phase to phase, an image at any phase k can be derived from a reference phase, say phase 1 for convenience,

$$\mu_k = D_{1\to k}\mu_1 \text{, for } k=1, 2, \ldots, K, \qquad (4.4)$$

where $D_{1\to k}$ is the deformation matrix to transform the image at phase 1 to that at phase k. Then Eq 4.2 can be re-written as

$$p_k = A_k D_{1\to k}\mu_1 \text{, for } k=1, 2, \ldots, K. \qquad (4.5)$$

letting $p = [p_1^{'}, p_2^{'}, \ldots, p_K^{'}]^{'}$ denote the projections for all phases and $A = (A_1 D_{1\to 1}, A_2 D_{1\to 2}, \ldots, A_K D_{1\to K})$ denote the 4D projection matrix, the 4D-MB model can be expressed as:

$$p = A\mu_1 \qquad (4.6)$$

Thus, the projections from all phases can be used to reconstruct the image at the reference phase 1, whereas the image at phase k can be obtained by using Eq 4.5 if the deformation matrix $D_{1\to k}$ is available.

Since the deformation matrix $D_{1\to k}$ is not known beforehand, the motion model has to be estimated and updated with the image reconstruction. Here we adapt the motion estimation method used in SMEIR [21] by matching the forward projections at each phase. For the convenience of expression of motion estimation, we define a deformation vector field (DVF) $d_{1\to k}$ as the displacement vector from phase 1 to phase k, which leads to the following equivalency,

$$D_{1\to k}\mu_1 = \mu_1(d_1 + d_{1\to k}) \text{, for } k=1, 2, \ldots, K, \qquad (4.7)$$

where d_1 is the coordinate vector. To obtain the inverse consistent forward $(d_{1\to k})$ and backward $(d_{k\to 1})$ DVFs required by 4D-MB reconstruction, a symmetric energy function is used as,

$$d^*_{1\to k} = \arg\min_{d_{1\to k}} \left\| p_k - A_1\mu_1(d + d_{1\to k}) \right\|_2^2 + \beta R(d_{1\to k})$$
,

$$d^*_{k\to 1} = \arg\min_{d_{k\to 1}} \left\| p_1 - A_k\mu_k(d + d_{k\to 1}) \right\|_2^2 + \beta R(d_{k\to 1})$$
,

$$\text{s. t. } d_{1\to k} \circ d_{k\to 1} = d_{k\to 1} \circ d_{1\to k} = 0, \qquad (4.8)$$

where $R(\bullet)$ is a smoothness regularization function for DVFs, β is a parameter balancing the first data fidelity term and the second smoothness regularization term, and $\circ$ is a composition operation defined as $d_{1\to k} \circ d_{k\to 1} = d_{1\to k}(d + d_{k\to 1}) + d_{k\to 1}$ that is equal to zero to enforce the inverse consistent constraint of DVFs. An interleaved optimization can be used to solve Eq 4.8, where a nonlinear conjugate gradient algorithm with back-tracking line search is used for two regularized minimizations and the inverse-consistency of DVFs is automatically enforced by using the solution of one minimization as the initialization of the other minimization. The β value was set as 0.05 for the phantom data and 0.5 for the patient data through the trial-and-error test. More details of SMEIR can be found in [21].

4.2.3 NCAT phantom simulation

A 4D NCAT phantom [118, 119] was used to simulate and to quantitatively evaluate the 4D-MB method. Ten respiratory phases of a male phantom were generated with a respiratory period 4 s. The maximum diaphragm motion of 20 mm and the maximum anterior-posterior motion of 12 mm were used to model the respiratory motion. Three orthogonal views for phase 1 are shown in Figure 4-3a. A spherical 3D tumor with a diameter of 10 mm was also included and indicated by a red arrow in Figure 4-3a. The dimension of the phantom and the reconstructed images were 256 × 256 × 100 with a voxel size of 2 × 2 × 2 mm^3 and the source

to detector distance and the source to isocenter distance was 750 mm and 500 mm, respectively, same as our previous work [21]. The Siddon's ray-tracing algorithm [63] was used to generate projection images with a detector matrix of 384 × 150 and a detector pixel size 2 × 2 mm². The distance between the blocker and the X-ray source is 75 mm. The moving blocker is made of lead strips with 2 mm width and 4 mm pitch (i.e. 4 mm gap between two strips). The ideal block of X-ray by the lead strips is assumed in the simulation so that the X-ray incident intensity is reduced by 1/3 when the blocker (blocked region : unblocked region = 1 : 2) is used. The noise was added as the sum of Poisson-distributed counting noise (1 × 10⁵ counts/incident ray) and Normal-distributed electronic noise (variance of 10) [21, 120]. The blocker motion is simulated to have six positions with a step-and-shoot mode. The blocker position related to the view angle is shown in Figure 4-2, where the blocker stays in the same position for each respiratory cycle (with 10 phases). Although in this ideal simulation case the position of the blocker has a repetitive pattern, the randomness arises from that these positions occur at the different projection view angles. It is important to note that the blocker positions are evenly distributed for each phase so that there is no missing projection area or overexpressing of a certain area. Both 4D-CBCT with and without the moving blocker were simulated for comparison. We name the acquisition with the moving blocker as "MB" and that without the moving blocker as "Conventional".
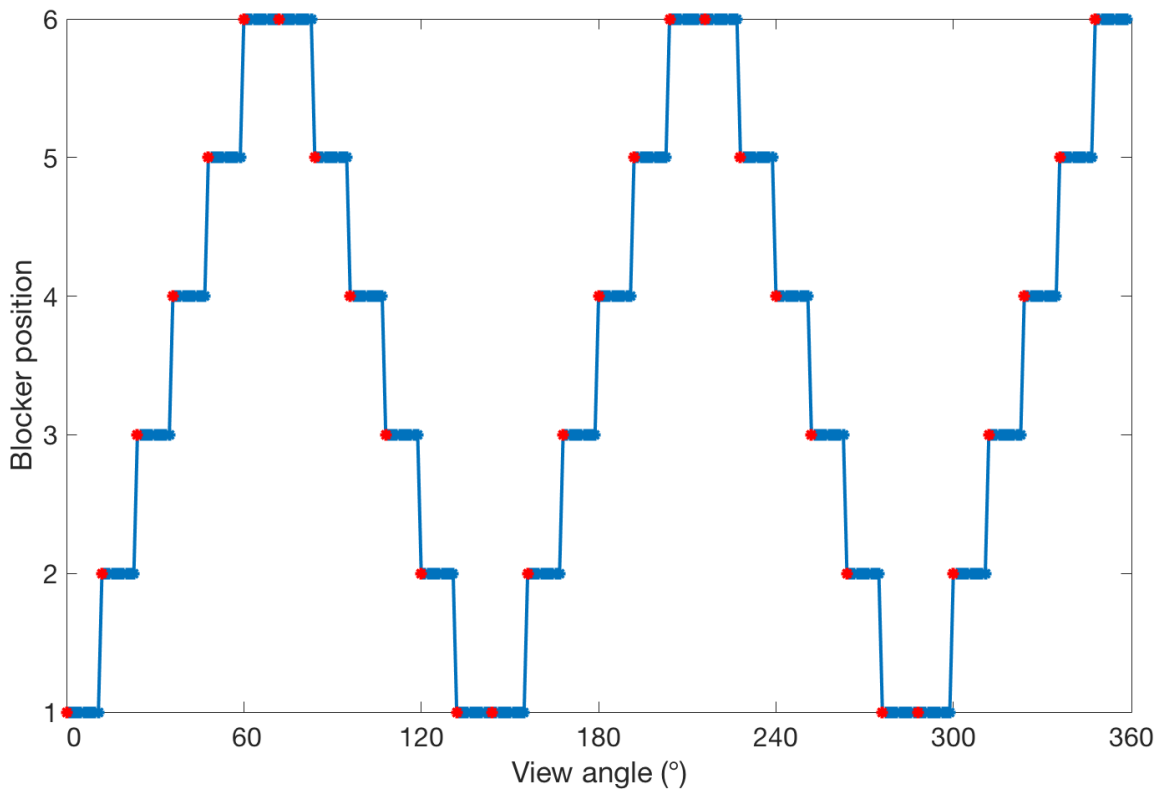
Figure 4-2 The blocker position versus the projection view angle in the simulation.

Figure 4-2 is showing the blocker position versus the projection view angle in the simulation. The red dot denotes the blocker position of the phase 1, where each blocker position has five occurrences. The other phases have the same blocker position distribution.

In the first experiment, the scatter was not included. Two cases were simulated: one with 300 projection views (i.e. 30 projections for each respiratory phase) and the other with 200 projection views (i.e. 20 projections for each phase), both evenly distributed around the phantom for 360°. This experiment will be used to compare the reconstruction performance using two different dose reduction methods for 4D CBCT: 1) lowering the number of the projection views (sparse view); or 2) reducing the X-ray fluence in each projection view (4D-MB). The moving blocker will be used for the simulation using 300 projection views and be compared with the results using 300 and 200 projection views without the moving blocker. Note

that the dose level using 300 projection views with each view blocked by 1/3 is equivalent to that using 200 views without the moving blocker (=300 × 2/3).

In the second experiment that used 300 projection views, we investigate the effect of the scatter correction rendered by 4D-MB. Specifically, the scatter signal within each projection image is simulated by convolving the primary signal with a point spread function derived from an experimental study (Gaussian function, sigma = 0.8 mm, size 141 × 141) [4]. The total observed signal becomes the sum of the scatter signal and the projection (primary) signal generated in the first experiment [10]. Two 4D CBCT acquisitions were simulated: one with the moving blocker (4D-MB) and the other without. In 4D-MB, the blocked regions record the scatter signal that will be used for scatter correction (See Section 2.B.).

In summary, we simulated the following three cases for the first experiment without including the scatter effect: 1) total 300 views for 10 phases without the moving blocker ("Conventional 30 views/phase"); 2) total 200 views for 10 phases without the moving blocker ("Conventional 20 views/phase"); and 3) total 300 views for 10 phases with the moving blocker ("MB 30 views/phase"). For the second experiment with the scatter effect, we simulated two cases: 1) total 300 views for 10 phases without the moving blocker ("Conventional 30 views/phase"); and 2) total 300 views for 10 phases with the moving blocker ("MB 30 views/phase"). Two reconstruction methods were used for the simulation data: 1) phase-by-phase 3D iterative reconstruction with a TV constraint ("3D TV"); and 2) 4D reconstruction combining both spatial TV minimization and motion compensated regularization ("4D SMEIR").

Structural similarity index (SSIM) [121] and root mean square error (RMSE) in Hounsfield unit (HU) are used as quantitative evaluation criteria. SSIM measures the similarity between two images on three aspects: intensity, contrast and structure and RMSE measures the overall absolute reconstruction error. The SSIM index and the RMSE are calculated in a volume of interest (160 × 90 × 50) centered at the NCAT phantom including the tumor of the

first phase (Figure 4-3a), unless otherwise stated. Specifically, the SSIM index is calculated on the VOIs (denoted as x for the ground truth and y for the estimate) of two images as follows:

$$SSIM(x, y) = \frac{(2\mu_x\mu_y + C_1) + (2\sigma_{xy} + C_2)}{(\mu_x^2 + \mu_y^2 + C_1)(\sigma_x^2 + \sigma_y^2 + C_2)},$$

where μ's are the average of VOIs, σ's are variance and covariance, and C_1 and C_2 are two variables to stabilize the division with weak denominator. In this work, C_1 is calculated as the square of 0.01 times of the dynamic range of the estimated image and C_2 is calculated as the square of 0.03 times of that. The RMSE is defined as:

$$RMSE = \sqrt{[\sum_i^n (x_i - y_i)^2]/n},$$

where i denotes the voxel index and n is the total number of voxels in the VOI.

In addition, the maximum and mean deviations from the tumor motion trajectory of the phantom for different methods are used to measure the motion recovery performance.

4.2.4 Patient study

To demonstrate the proposed method in a more clinically relevant setting, we generated the moving-blocker data from a set of real patient data. This patient underwent radiotherapy for lung cancer. CBCT was acquired using an Elekta Synergy® XVI system (Elekta AB, Stockholm, Sweden) with a M20 collimator and a F1 bow-tie filter. The acquisition protocol parameters were: 120 kVp and 1.6 mAs per projection, a total of 631 projection (512 × 512 pixels with a pixel size of 0.8 × 0.8 mm2) views evenly distributed in 360º, and acquisition time of 2 min. The source to detector distance was 1536 mm and the source to isocenter distance was 1000 mm. The CBCT projections were grouped into eight phases based on the diaphragm position at each projection and further downsampled by half, which results in around 49 projections for each phase. The reconstructed images are 300 × 300 ×150 with a voxel size of 1.6 × 1.6 × 1.6 mm3. A moving blocker blank acquisition was simulated using the same acquisition protocol of the

patient data so that the blocked regions in each projection of the real patient data can be identified. The pseudo-real moving blocker patient data were obtained by setting the intensity in the blocked regions of the real patient projection data as zero. The removed data (i.e. those with intensity set as zero) is about 1/3 of the original data, which leads to about 1/3 dose reduction for the pseudo-real moving blocker patient data. Since the real moving-blocker data is not available at this point, it is not possible to evaluate the scatter correction effect, but will be investigated in future work. In this work, we aim to demonstrate the feasibility of 4D-MB with 1/3 dose reduction on real patient data. It will be compared with reconstruction results at the regular dose with and without motion compensation.

4.3 Results

4.3.1 Results of 4D NCAT phantom

A. Results without scatter included

Figure 4-3 shows the reconstructed images of phase 1 NCAT phantom in three orthogonal views: transverse (left), coronal (middle) and sagittal (right). In all cases, the tumor is visible, but clearer for 4D reconstruction. Figs. 3b-d illustrate the images reconstructed by 3D TV for conventional 30 views/phase, conventional 20 views/phase, and MB 30 views/phase, respectively. The latter two acquisitions (Figure 4-3c and 3d) have 1/3 dose reduction compared to the first one (Figure 4-3b). With the number of projection views decreased from 30/phase to 20/phase, the images in Figure 4-3c suffers more blurring and blocky artifacts than that in Figure 4-3b because the stronger TV regularization has to be applied to address the streak artifacts caused by the missing-data. Some fine structures in the lungs are missing due to this effect (e.g. yellow and blue arrows in Figure 4-3c). It is interesting to see that, at the equivalent dose level, 3D TV with MB 30 views/phase (Figure 4-3d) recovered this fine structure to a better extent than that with conventional 20 views/phase, likely attributing to the effect of different undersampling methods. However, some horizontal streak artifacts can be seen in the coronal and sagittal views (e.g. green arrow in Figure 4-3d), likely due to use of the blocker. With 4D

motion-compensated reconstruction (4D SMEIR), the reconstructed images are less blurred and maintain better fine structures than those with 3D TV. The images of 4D SMEIR with conventional 30 views/phase (Figure 4-3e) achieve the closest similarity to the original phantom (Figure 4-3a). The reduction of 1/3 of the number of projection views suffers notable blocky artifacts and lowered contrast in the reconstructed images (Figure 4-3f). At the equivalent dose level, the proposed method of MB 30 views/phase with 4D SMEIR (Figure 4-3g) seems to suffer less blocky artifacts and to maintain more fine structures compared to that in Figure 4-3f. The tumor contrast is also notably higher in Figure 4-3g than Figure 4-3f. In addition, the horizontal streak artifacts in the coronal and sagittal views in MB 30 views/phase with 3D TV (Figure 4-3d) are effectively suppressed in MB 30 views/phase with 4D SMEIR (Figure 4-3g).

The quantitative measures are listed in Table 3-1. The rankings using SSIM are generally the same as that using RMSE, i.e. a higher SSIM value leads to a lower RMSE value. It can be seen that the best quantitative results are obtained with conventional 30 views/phase with 4D SMEIR, followed by MB 30 views/phase with 4D SMEIR (2/3 dose of the former). It is worth noting that 4D SMEIR at reduced dose level through either a reduced view number or the moving blocker can achieve higher quantitative accuracy than conventional 30 views/phase with 3D TV reconstruction. This demonstrates that 4D motion-compensated reconstruction is crucial to improve or maintain image quality at lowered imaging dose for 4D CBCT. In summary, both the reconstructed images and the quantitative results in this experiment seem to favor undersampled projection rays (30 views/phase with MB) over undersampled view angles (20 views/phase without MB) for a fixed dose level. Further investigation on these two undersampling strategies is needed to generalize this finding.

94
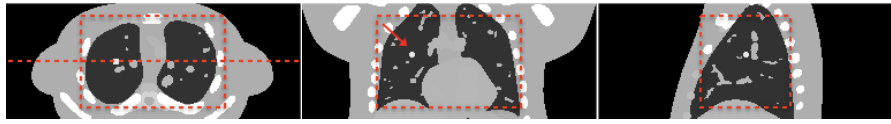
(a) NCAT phantom
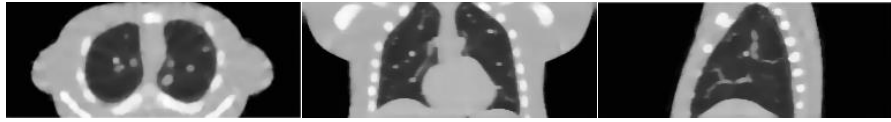
(b) Conventional 30 views/phase – 3D TV
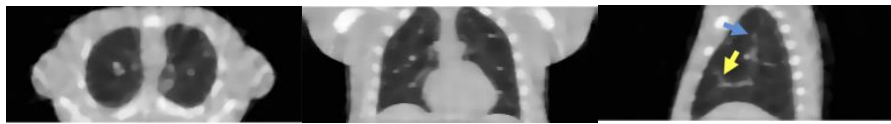
(c) Conventional 20 views/phase – 3D TV
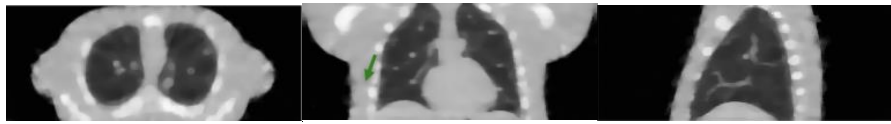
(d) MB 30 views/phase – 3D TV

(e) Conventional 30 views/phase – 4D SMEIR

(f) Conventional 20 views/phase – 4D SMEIR

(g) MB 30 views/phase – 4D SMEIR

Figure 4-3 Reconstruction results comparison without scatter

Figure 4-3 is showing the NCAT phantom and reconstructed images using different 4D

CBCT acquisition methods (Conventional acquisition and MB acquisition) and reconstruction

methods (3D TV and 4D SMEIR). No scatter was included in simulation. (Left: transverse; middle: coronal; right: sagittal). The red dashed line in (a) transverse view is the profile position of Figure 4-5. The red arrow in (a) coronal view indicates the tumor. The three dot squares in (a) are the volume of interest (VOI) for quantitative measures of SSIM and RMSE. The yellow and blue arrows indicate the fine structures lost in 3D TV with fewer views and the green arrow points the artifact likely due to use of the blocker. Table 4-1 is showing the structure similarity index (SSIM) and the root mean square error (RMSE) in HU for different acquisition and reconstruction methods, both calculated on the volume of interest (VOI) centered at the phantom.

Table 4-1 SSIM and RMSE results

	3D TV			4D SMEIR		
	Conventional 30 views/phase	Conventional 20 views/phase	MB 30 views/phase	Conventional 30 views/phase	Conventional 20 views/phase	MB 30 views/phase
SSIM	0.78	0.65	0.67	0.90	0.81	0.86
RMSE	70	91	89	50	62	59

B. Results with scatter included

Results in this section are with 30 projection views/phase and scatter signal included in the CBCT simulation. Figure 4-4 illustrates the reconstructed images with conventional and MB acquisitions and different reconstruction methods. Without scatter correction (SC), both 3D TV (Figure 4-4a) and 4D SMEIR (Figure 4-4b) suffer the shading artifacts and low contrast, although 4D SMEIR images are much better than 3D TV (in the middle region of the field of view). With the MB acquisition, the scatter signal can be effectively removed from the projection data, which results in greatly improved image quality as shown in Figure 4-4c using 3D TV and Figure 4-4d using 4D SMEIR, in addition to the benefit of 1/3 reduction of the radiation dose.

Similar to the findings in the simulations without scatter, images reconstructed by 4D SMEIR show improved tumor contrast and preserve more structural details than that reconstructed by independent phase-by-phase 3D TV reconstruction.
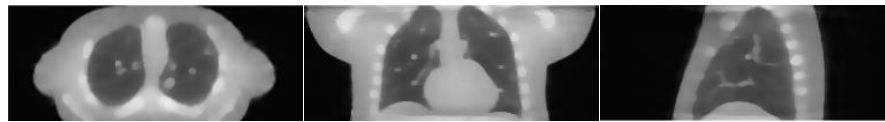
(a) Conventional 30 views/phase – 3D TV (no SC)
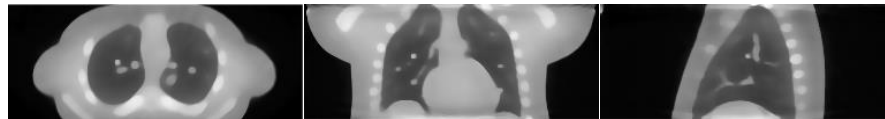
(b) Conventional 30 views/phase – 4D SMEIR (no SC)
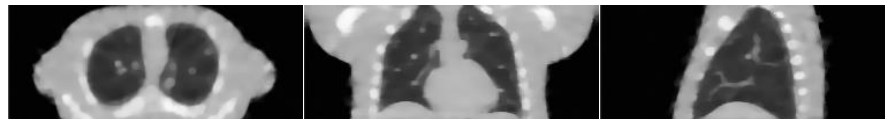
(c) MB 30 views/phase – 3D TV (with SC)

(d) MB 30 views/phase – 4D SMEIR (with SC)

Figure 4-4 Reconstruction results comparison with scatter

Figure 4-4 is showing the reconstructed NCAT images using different 4D CBCT acquisition methods (conventional acquisition and MB acquisition) and reconstruction methods (3D TV and 4D SMEIR) with scatter included in the simulation (SC: scatter correction). Note that the radiation dose in (c) and (d) is 1/3 lower than that in (a) and (b) because of use of the moving blocker.

The line profiles (the red dashed line in Figure 4-3a) across the tumor in the transverse slice in Figure 4-4 are shown in Figure 4-5 to compare the different acquisition and reconstruction methods. Both 3D TV and 4D SMEIR with scatter correction recover the attenuation coefficient profile much better than those without scatter correction, even though the

radiation dose with the MB acquisition is just 2/3 of the conventional one. Although 4D SMEIR without scatter correction outperforms 3D TV without scatter correction, it is inferior to 3D TV with scatter correction in general (except at the tumor location indicated by the arrow). The proposed 4D MB with motion-compensated reconstruction (MB-SMEIR) yields the closest profile to the phantom as it takes the advantages of both spatiotemporal 4D reconstruction and moving-blocker based scatter correction. It is important to note that this substantial reconstruction accuracy improvement of MB-SMEIR is accompanied with the dose reduction benefit of 1/3, compared to SMEIR with the conventional acquisition.
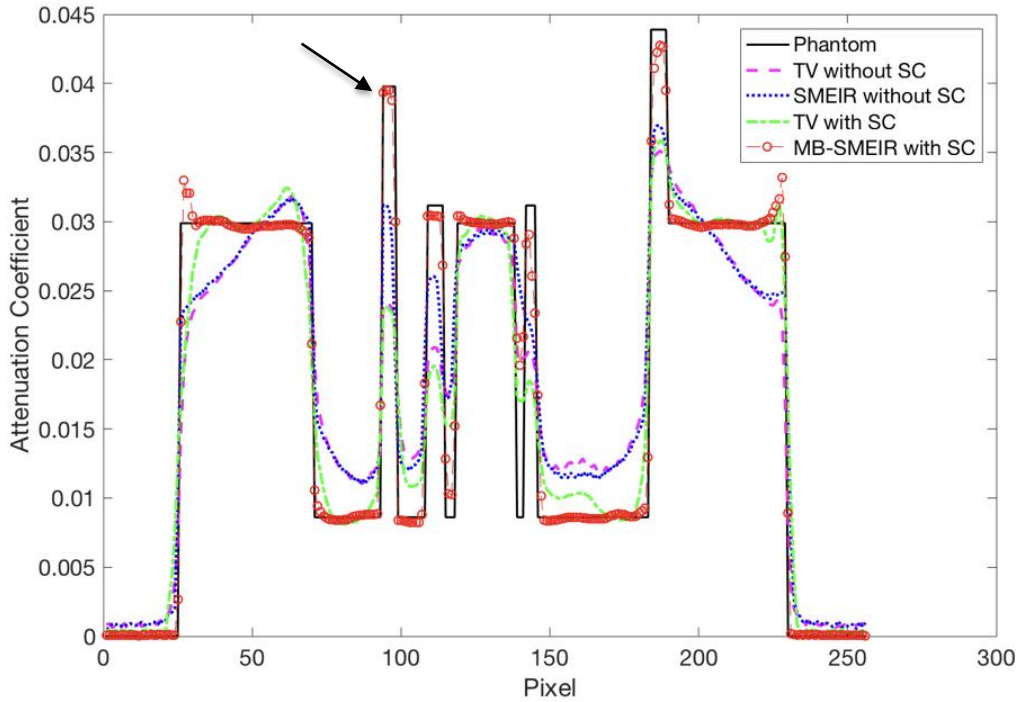
Figure 4-5 Line profiles comparison

Figure 4-5 is showing the line profiles across the tumor in a transverse slice (denoted by a red dashed line in Figure 4-3a) for different methods shown in Figure 4-4. The arrow indicates the tumor location. Table 4-2 is showing the SSIM and RMSE values for different acquisition methods (conventional acquisition and MB acquisition) and reconstruction methods

(3D TV and 4D SMEIR) with/without scatter correction (SC). Note that the radiation dose of the MB acquisition is only two thirds of the conventional acquisition.

The quantitative measures are listed in Table 4-2. It can be seen that 4D SMEIR outperforms their counterpart using phase-by-phase 3D TV reconstruction under the same condition of data acquisition and scatter treatment. Although SMEIR without scatter correction improved the SSIM metric to the similar level of 3D TV with the moving-blocker based scatter correction, it suffers a much large absolute reconstruction error (131 HU vs. 89 HU). With 1/3 dose reduction, the proposed 4D MB method with SEMIR improves the SSIM measure by 37% and the RMSE measure by 55% compared to the conventional SMEIR without the moving blocker based scatter correction. At the same dose level, SMEIR with the MB acquisition and scatter correction outperforms 3D TV under the same condition by 28% on SSIM and 34% on RMSE.

Table 4-2 The SSIM and RMSE values for different acquisition methods

| | Without MB and SC | | With MB and SC | |
	3D TV	4D SMEIR	3D TV	4D SMEIR
SSIM	0.58	0.63	0.67	0.86
RMSE (HU)	136	131	89	59

C. Tumor motion recovery

The tumor motion trajectories of all respiratory phases are calculated for each method and compared with the tumor motion trajectory of the 4D NCAT phantom (serving as the true tumor motion). Specifically, the deformation vectors in a small volume (2 × 2 × 2 voxels) at the tumor center are averaged to get the motion from the reference phase (i.e. phase 1) to the target phases (i.e. phase 2~10). The deviations from the true tumor motion for different methods are plotted in Figure 4-6. The tumor motion recovered by 4D SMEIR with MB and SC ("MB-SMEIR with SC", green lines) matches well with the true motion with deviations generally less

than 2 mm, except for phases 8 and 9. TV with SC (blue lines) also achieves good motion recovery performance with deviations more than 2 mm only for three phases (3, 4, and 8). Although SMEIR without SC (magenta lines) recovers the tumor motion much better than TV without SC (red lines), their deviations are worse than the methods with SC. The maximum and mean deviations over all phases are listed in Table 4-3. The maximum and mean deviations from the true tumor motion (from the phantom) for different acquisition methods (conventional acquisition and moving-blocker (MB) acquisition) and reconstruction methods (3D TV and 4D SMEIR) with/without scatter correction (SC). The proposed MB-SMEIR method outperforms other methods in both criteria, with a maximum deviation of 3.01 mm and a mean deviation of 1.48 mm.
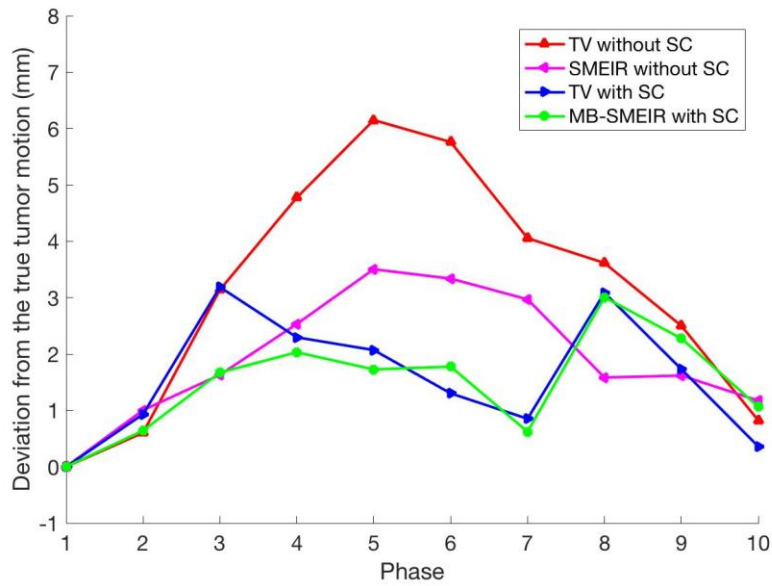
Figure 4-6 The deviations of reconstructed tumor motion

Table 4-3 The maximum and mean deviations

	Without MB and SC		With MB and SC	
	3D TV	4D SMEIR	3D TV	4D SMEIR
Max (mm)	6.15 mm	3.50 mm	3.19 mm	3.01 mm
Mean (mm)	3.14 mm	1.94 mm	1.58 mm	1.48 mm

D. Reconstruction convergence

The objective function to be minimized for $d_{1 \to k}$ at phase 5 (k=5 in the first objective function in Eq 4.8) is used to show the convergence of 4D-MB reconstruction. As shown in Figure 4-7, 4D-MB reconstruction indeed converges with continuous decreasing of the objective function values. It can be seen that the first 50 iterations, there is a slight jump of the objective function value because the SART and TV minimization used for image reconstruction update the images after every 10 DVF estimation. This jump diminishes as the iteration goes on beyond 100. It is worth noting that different view angle and projection ray undersampling patterns, which result in different system matrices, may influence the convergence. This topic is out of the scope of the current work and will be investigated in future work.
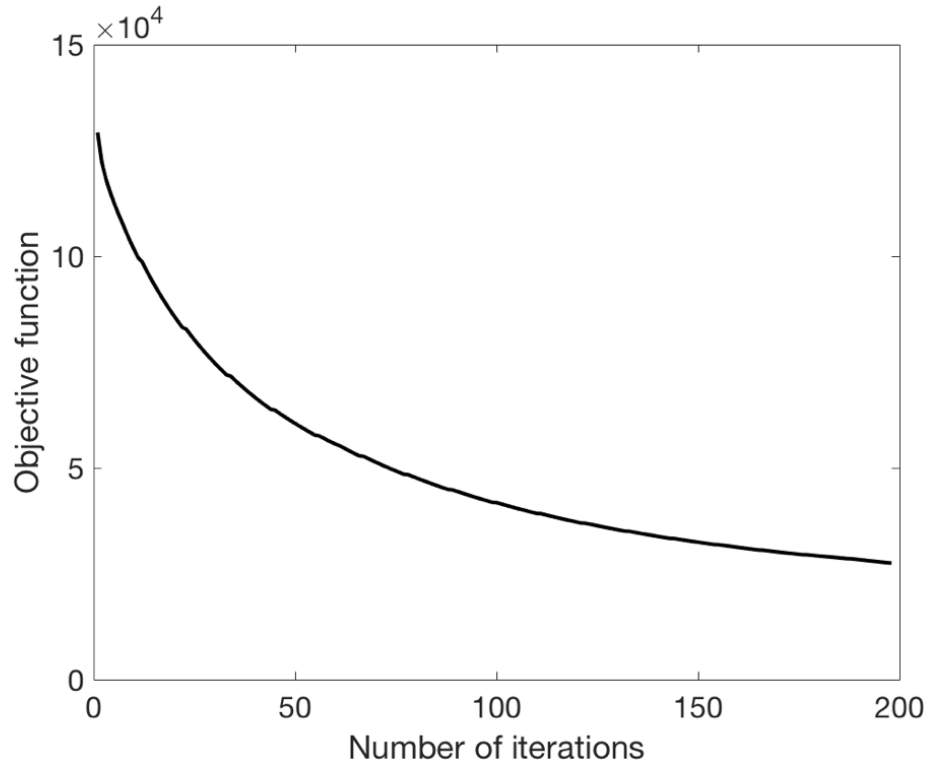
Figure 4-7 Convergence of 4D MB reconstruction (objective function in Eq 4.8)

4.3.2 Results of the lung cancer patient

In Figure 4-8, we show the images reconstructed from the real patient data and the pseudo-real moving blocker patient data for two respiratory phases. The first two columns are the coronal view and the last two columns are the sagittal view. It can be seen that 4D SMEIR effectively suppresses the noise compared to 3D TV. In both cases of with and without moving blocker, 4D SMEIR achieves less noisy and higher contrast images, thus leading to better-defined structures. Comparing 4D SMEIR at the regular dose and at 2/3 of the regular dose with the moving-blocker, the reconstructed images look similar except that the latter suffers slight more noise due to the reduced imaging dose. This is consistent with the findings in the NCAT simulation study without scatter (Section 3.A.1. and Figure 4-3). This preliminary patient study indicates that the substantial dose reduction without compromising the image quality may be

achievable. The proposed 4D MB method provides a promising way to achieve the dose reduction goal through random sparse sampling in each projection view and advanced 4D reconstruction.

There is generally no ground truth in real patient images, which is why the phantom study was conducted in the first place. To quantify the performance of different methods in patient study, we use SMEIR without MB as the ground truth and calculate the SSIM and RMSE of the VOIs (shown in red dashed boxes in Figure 4-8) for other methods. The results using phase 1 as the reference phase for SMEIR are shown in Table 4-4. It can be seen that 4D SMEIR can produce better quantitative results than 3D TV. It is interesting to note that 3D TV without MB and with MB have the similar performance, which may implicate the data redundancy. Also, the results for phase 3 seem to deteriorate a bit, particularly for 3D TV methods. It is likely due to the fact that the ground truth of phase 3 was deformed from phase 1 using the estimated DVF in 4D SMEIR, which may not be perfect. To further characterize the motion influence, 4D SMEIR without MB using phase 3 as the reference is used as the ground truth and the corresponding results are shown in Table 4-5. The phase 3 results using phase 3 as the reference are in the similar range as the phase 1 results using phase 1 as the reference. The improvement of the current SMEIR method will be investigated in future studies as detailed in Discussion.
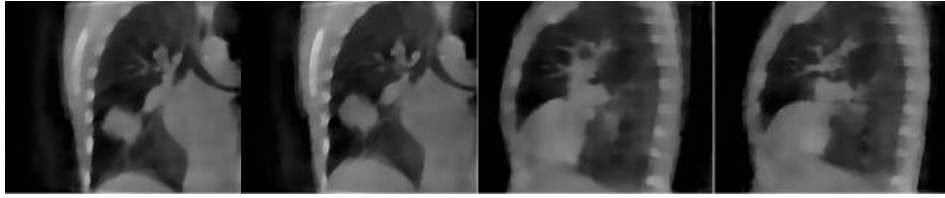
(a) 3D TV for real patient data
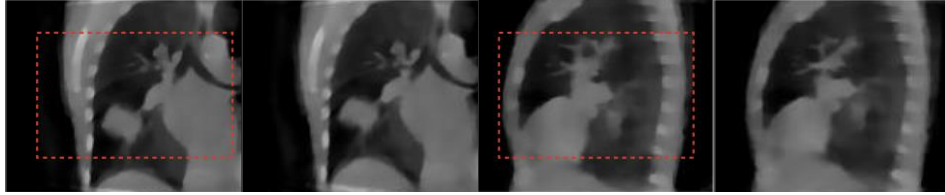
(b) 4D SMEIR for real patient data
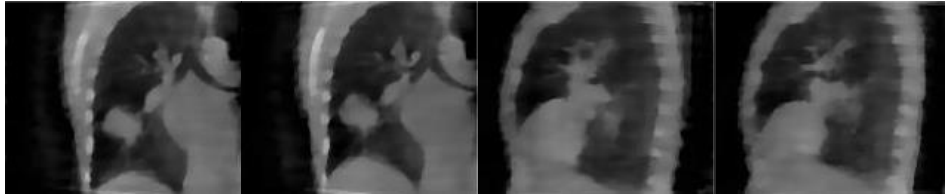
(c) 3D TV for pseudo-real moving-blocker data
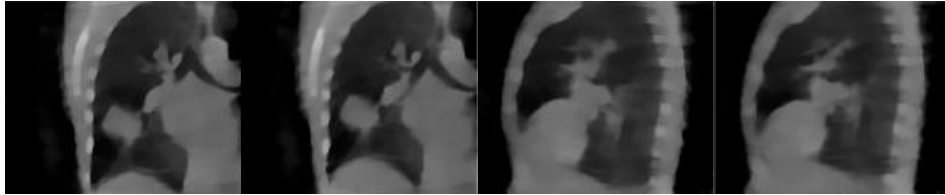
(d) 4D SMEIR for pseudo-real moving-blocker data

Figure 4-8 Reconstruction results of patient

Figure 4-8 is showing the reconstructed images (from left to right: coronal phase 1, coronal phase 3, sagittal phase 1, and sagittal phase 3) from different reconstruction methods for real patient data at the regular dose and pseudo-real moving blocker data at 2/3 of the regular dose. The red dashed boxes are for quantitative measures in Table 4-4 and 4-5.

Table 4-4 SSIM and RMSE (Phase 1 as the reference phase for SMIER)

| | Without MB | | With MB | | | |
| | 3D TV | | 3D TV | | 4D SMEIR | |
	Phase 1	Phase 3	Phase 1	Phase 3	Phase 1	Phase 3
SSIM	0.949	0.900	0.940	0.900	0.978	0.967
RMSE (HU)	38	62	42	59	34	44

Table 4-5 SSIM and RMSE (Phase 3 as the reference phase for SMEIR)

| | Without MB | With MB | |
	3D TV	3D TV	4D SMEIR
SSIM	0.947	0.938	0.981
RMSE (HU)	34	41	31

4.4 Discussion

In this work, we demonstrated the working principle of a novel 4D moving blocker method, which is the first time, to our best knowledge, to combine a moving blocker with 4D CBCT to achieve simultaneous dose reduction and scatter correction. Although there were a few studies using blockers/modulators for scatter correction in 3D CBCT [7, 10, 11, 122] or using moving multi-slit collimator (MSC) for dose reduction in MDCT [123, 124], all of them are limited to 2D or 3D reconstruction. The current study is the first study that utilizes the random under-sampling in each projection view for imaging and reconstruction of a moving object (lung here), which can be modeled as a 4D signal in nature. With advanced compressed sensing (i.e. image gradient sparsity enforced by TV constraints) and motion-compensated 4D (SMEIR) reconstruction, the satisfactory reconstruction images with 1/3 dose reduction were obtained for

both simulation and pseudo-real patient data. In addition, the proposed 4D MB method can provide a simple observation based scatter correction for CBCT, which is demonstrated by a simulation study with large improvement in reconstruction accuracy (31% on SSIM and 58% on RMSE). Note that this type of scatter correction requires only interpolation and subtraction in the projection domain, and thus is less computational demanding than computational SC methods.

Furthermore, the dose reduction can also be achieved by reducing the projection views. In this regard, we compared the equivalent dose scheme: 1) 200 views of 4D CBCT without MB; and 2) 300 views of 4D MB CBCT. The simulation results showed that 4D MB CBCT achieved the similar reconstruction performance, if not better, to 200-view 4D CBCT without MB. Considering the capability of simple SC rendered by MB and the constant switch on-and-off of the X-ray tube current required by the fewer view acquisition, 4D MB CBCT may holds a great potential for both dose reduction and scatter correction purposes. On the other hand, adding a moving blocker to the CBCT system may pose some challenges. Nevertheless, a motor-controlled moving blocker has been demonstrated to be feasible in our previous study [11] due to its lightweight for kilovoltage CBCT. Some optimal conditions for SC have been investigated in our previous work [90] and most results are satisfactory (with CT number error < 50 HU). Thus, there is no strict requirement on the blocker moving speed or style as long as the blocker position is evenly distributed for each phase. For example, another possible blocker motion for the step-and-shoot mode is shown in Figure 4-9, which led the similar satisfactory results to that used in Figure 4-2. In reality, due to the irregularity of patient breath, the blocker motion needs to be controlled to make the distribution of the blocker position for each phase roughly even. Nonetheless, the study of the optimal blocker design, e.g. ratio of blockers, gaps, moving speed, and moving style (continuous or step-and-shoot) and the minimal number of projection views will be important future work to discover their impact on 4D CBCT reconstruction and clinically relevant tasks using more realistic physics modeling or real physical phantom/patient experiments. The effect of sparse sampling due to different view angles and blocker positions

on reconstruction convergence and parameter selection will be investigated and provide the practical guidance for the adaption of such a system.

In this proof-of-concept study, the CT imaging physics is not fully modeled, such as the omission of penumbra effects due to either blocker penetration or limited size of the X-ray source, and the lag effects [125]. These factors may need further investigation to answer whether they will significantly impact the reconstruction performance. However, based on our studies on MB based scatter correction for 3D CBCT using physical phantoms [10, 11, 90, 97], it is reasonable to expect the similar effectiveness for 4D MB CBCT. The current simulation study is sufficient to demonstrate the feasibility of 4D MB CBCT in principle. In addition, the blocker could generate scatter photons that would contribute extra radiation dose to the patient. As a preliminary investigation of this problem, two air scans were performed: one with the moving blocker (blocked region : unblocked region = 1:1) and the other without it using the Varian TrueBeam OBI system (678 projections). The ratio of the intensity (as a surrogate of irradiation dose) of all the projections between that with the blocker and that without the blocker is about 48%, which is slightly less than the expected value of 50%. As the lead strips are embedded on a 5 mm thick acrylic board, the 48% ratio (<50%) can be attributed to that the attenuation of the acrylic board outweighs the contribution of the scatter photons from the blocker.

Furthermore, the radiation dose was measured on an Elekta Versa HD system. The scan was a standard lung protocol with the following scanning parameters: 120 kVp, 2 min nominal rotation time, 264 mAs and the beam collimation of 26.5 cm × 26.5 cm. A 32 cm diameter PMMA CTDI phantom was aligned in the center of the scanning field of view. A 10 cm long pencil chamber was placed in the center or 12 o'clock position. The CTDI was calculated using the CBDI method [15].

$$CTDI_w = \frac{1}{3}D_c + \frac{2}{3}D_p$$

Where *Dc* and *Dp* denote the measured dose in the center and peripheral locations. This de nition is an approximation of average dose along the 10 cm range in the middle of the phantom. CTDI measurements were performed without a blocker and with a blocker (1:3 pitch matching the simulation setting). Three repeated measurements were performed at each position and the averaged value was used. The calculated *CTDIw* was 5.7 mGy without the blocker and 3.5 mGy with the blocker, which is consistent with the pitch of the blocker for 1/3 dose reduction.

On the other hand, the scatter photons generated by the blocker can reach the detector, which could possibly degrade the projection data. However, the scatter photon from the blocker is of lower energy compared to the incident photons. After passing through patients, the probability of the blocker generated scatter reaching the detector would be very small. Although we are not able to separate the blocker generated scatter photons and patient induced photons in our experiments, satisfying scatter correction performance was achieved in our previous studies using physical phantoms [10, 11, 90, 97]. A detailed Monte Carlo simulation study can potentially separate scatter photons from different sources at the detector, which will be investigated in a future study.
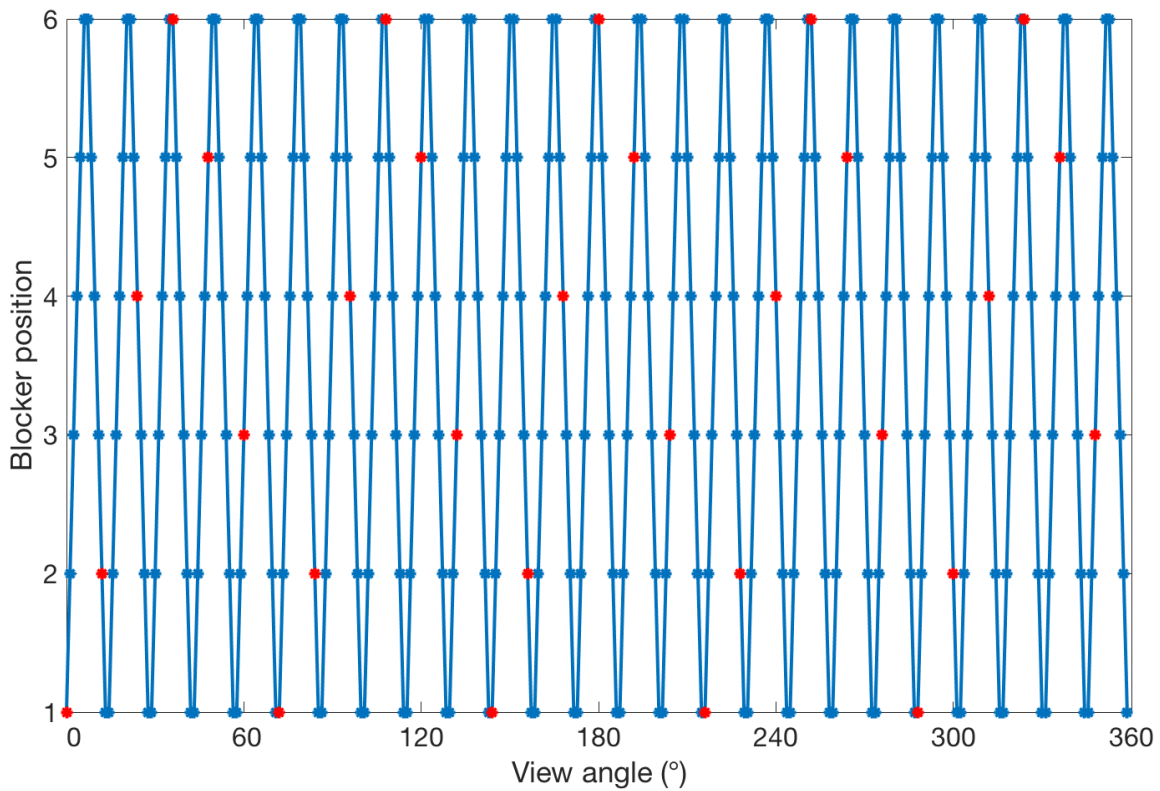
Figure 4-9 The blocker position versus the projection view angle.

Finally, there are several potential improvements of the current study worth mentioning. First, the TV was used to enforce spatial sparsity of image gradient. It works well for images with piece-wise constant features, like NCAT images, but may not be suitable for the real patient data with subtle textures. In future studies, more advanced spatial priors will be investigated, such as normal-dose image induced TV [126], total generalized variation [127], TV-stokes [128], l_0 gradient [129], Haralick texture measures [130]. Second, SMEIR seemed to achieve a large improvement on NCAT phantom data over 3D reconstruction, but only a moderate one on the pseudo real patient data (see Figure 4-8.). One reason is that the complication of the real clinical data deteriorates the image quality of 3D reconstruction, which results in larger errors in the initial DVF estimation. These errors may cause SMEIR to trap into a local optimal, instead of the global optimal. Either better initial DVF estimation by a better initial 3D reconstruction or constrained DVF estimation with a reliable prior model can mitigate

this problem and will be investigated in future. It is also worth looking into the way of estimating motion for two phases far away. In this study, the direct motion estimation for any pair of phases was used. Instead, the motion can be estimated for neighboring phases and that for far-away phases can be derived from the neighboring motion since the motion estimation can deteriorate quickly when the motion is too big. Meanwhile, patient respiration irregularity and hysteresis may cause additional difficulties in 4D MB CBCT and will need to be addressed in future studies. Last, in the future studies of improving the proposed 4D MB CBCT, a task-based performance evaluation, such as tumor motion tracking and organ segmentation for dose calculation, will need to be employed and compared with clinically adapted low-dose CT methods, such as lowering tube current, and other scatter correction methods for its real clinical impact.

4.5 Conclusions

In this work, we proposed a moving blocker based 4D CBCT acquisition (4D MB) and combined motion-compensated image reconstruction method with the moving blocker based scatter correction. In the NCAT simulation study, 4D MB with motion-compensated reconstruction at 2/3 of the regular dose can achieve much higher reconstruction accuracy reflected by image appearance and quantitative measurements, compared with the conventional SMEIR without scatter correction at the regular dose. A synthetic patient study also shows the potential of the proposed method to reduce the radiation dose by 1/3 without compromising the image quality. These promising results encourage more comprehensive studies to use realistic physical phantoms and patient data to interrogate the dose reduction limitation of the proposed 4D MB method using the clinical relevant metrics, e.g. tumor and organ segmentation and CT number for dose calculation. More sophisticated motion estimation methods and advanced spatial priors other than TV are also worth exploring to further improve the performance of this novel method.

Chapter 5 Conclusions and Future Work

The goal of this dissertation work is to develop novel methods to improve the image quality of CBCT. The methods proposed in this dissertation include: 1) using different deconvolution methods to recover true scatter signal in blocked regions; 2) enhancing the scatter estimation accuracy and robustness by using adjacent multiple-view projection images; 3) applying the moving blocker method for 4D CBCT for simultaneous radiation dose reduction and scatter correction purposes. These techniques are demonstrated either by simulations of digital phantoms or real phantom and clinical CBCT data.

First, we proposed several deconvolution methods to improve the accuracy of the scatter correction. The slanted-edge method was used to derive the LSF and PSF using a parametric model. The results of the simulation study showed that with a good PSF estimation, the deconvolution method can significantly alleviate the detector response effect. Therefore, the moving blocker system with deconvolution method can generate high quality CBCT image. The high quality image can improve anatomical visualization and dose calculation accuracy in the treatment position, which are essential for the adaptive radiation therapy.

Second, we investigated the scatter estimation errors caused by single-view SC (SVSC) used in the moving-blocker SC method for the regions with fast scatter signal changes or lack of scatter samples and the blocker detection errors. To address these problems, we proposed a multi-view SC (MVSC) method using several neighboring views. In the regions with fast scatter signal changes or missing scatter samples at the margin, the scatter signal is hard to be recovered accurately with limited sampling points by using just one projection view in SVSC. The MVSC method uses the adjacent projection views, which can provide more information of the scatter signal in different locations along the blocker moving direction because of the blocker movement during the gantry rotation. The scatter estimation and corresponding reconstruction results show that the MVSC method can eliminate the scatter estimation errors in the regions with fast scatter signal changes (Figure 3-6) or lack of scatter

111

samples (Figure 3-10) and maintain the superior scatter correction performance for other regions (Table 3-1). The scatter signal is recovered more accurately with the MVSC method and result in a reconstructed image with reduced artifacts and more accurate quantitative results (CT numbers).

Finally, we demonstrated the working principle of a novel 4D moving blocker method, which is the first time, to our best knowledge, to combine a moving blocker with 4D CBCT to achieve simultaneous dose reduction and scatter correction. In the NCAT simulation study, 4D MB with motion-compensated reconstruction at 2/3 of the regular dose can achieve much higher reconstruction accuracy reflected by image appearance and quantitative measurements, compared with the conventional SMEIR without scatter correction at the regular dose. A synthetic patient study also shows the potential of the proposed method to reduce the radiation dose by 1/3 without compromising the image quality. These promising results encourage more comprehensive studies to use realistic physical phantoms and patient data to interrogate the dose reduction limitation of the proposed 4D MB method using the clinical relevant metrics, e.g. tumor and organ segmentation and CT number for dose calculation.

The further investigation is planned to test the MVSC method on the phantoms, such as the chest and the head, where the bone/lung and body/air interfaces may manifest its benefit. More sophisticated motion estimation methods and advanced spatial priors other than TV are also worth exploring to further improve the performance of 4D moving-blocker based CBCT.

Publications

Journal papers:
1. **Cong Zhao**, Xi Chen, Luo Ouyang, Jing Wang, and Mingwu Jin, "Robust moving-blocker scatter correction for cone-beam computed tomography using multiple-view information", *PLoS ONE* 12(12): e0189620, 2017.
2. **Cong Zhao**, Yuncheng Zhong, Xinhui Duan, You Zhang, Xiaokun Huang, Jing Wang, and Mingwu Jin, "4D cone-beam computed tomography (CBCT) using a moving-blocker for simultaneous radiation dose reduction and scatter correction," submitted, *Phys. Med. Biol.*, 63, no. 11 (2018): 115007.

Conference papers:
1. **Cong Zhao**, Yuncheng Zhong, Jing Wang, and Mingwu Jin, "Modified simultaneous motion estimation and image reconstruction (M-SMEIR) for 4D CBCT," *Biomedical Imaging: From Nano to Macro, 15th IEEE International Symposium on (ISBI)*, accepted, 2018.
2. Mingwu Jin, **Cong Zhao**, Xun Jia, and Lifeng Yu, "Motion-compensated reconstruction for limited-angle multiphase cardiac CT," 10573-110 (8 pages), *SPIE Medical Imaging* 2018.
3. **Cong Zhao**, Yuncheng Zhong, Jing Wang, and Mingwu Jin, "Simultaneous Dose Reduction and Scatter Correction for 4D Cone-Beam Computed Tomography," *IEEE Nuclear Science Symposium and Medical Imaging Conference*, M-16-6, 2017.
4. **Cong Zhao**, Xi Chen, Luo Ouyang, Jing Wang, and Mingwu Jin, "Robust Estimation of Scatter and Primary Signals using Multi-View Information for Moving Blocker-Based Cone-Beam Computed Tomography," *IEEE Nuclear Science Symposium and Medical Imaging Conference*, M-03-059, 2017.
5. **Cong Zhao**, Luo Ouyang, Jing Wang, and Mingwu Jin, "Multi-view scatter estimation for moving blocker scatter correction of CBCT," *IEEE Nuclear Science Symposium and Medical Imaging Conference*, M10D-12, 2016.
6. **Cong Zhao**, Luo Ouyang, Jing Wang, and Mingwu Jin "Blind Deconvolution for Blocker-Based Scatter Correction of CBCT" *IEEE Nuclear Science Symposium and Medical Imaging Conference*, M3CP-209, 2015.
7. Mingwu Jin, **Cong Zhao**, Jaehoon Yu, Wei Chen, Guiyang Hao, Xiankai Sun, and Glen Balch, "Spatial and temporal processing for functional imaging probes," *IEEE Nuclear Science Symposium and Medical Imaging Conference*, M10-66, 2014.
8. Mingwu Jin, **Cong Zhao**, Jaehoon Yu, Wei Chen, Guiyang Hao, and Xiankai Sun, "Acceleration of the Acquisition of Imaging Probes using Spatiotemporal Processing," *IEEE Nuclear Science Symposium and Medical Imaging Conference*, M18-46, 2013.

Conference abstracts:
1. **Cong Zhao**, Yuncheng Zhong, Jing Wang, and Mingwu Jin, "Moving-blocker based 4D cone-beam computed tompography: a phantom study," 132-030, 6th International Workshop on Computational Human Phantom, 2017.
2. **Cong Zhao**, Yuncheng Zhong, Jing Wang, and Mingwu Jin, "4D low-dose CBCT using a moving-blocker," TH-AB-601-1, 59th AAPM Annual Meeting, 2017.
3. **Cong Zhao**, Xi Chen, Luo Ouyang, Jing Wang, and Mingwu Jin, "Multi-view scatter correction for moving-blocker based CBCT," TH-AB-601-9, 59th AAPM Annual Meeting, 2017.
4. **Cong Zhao**, Luo Ouyang, Jing Wang, and Mingwu Jin, "Investigation of deconvolution methods for blocker-based CBCT scatter estimation," 57th AAPM Annual Meeting, 2015.

References

[1] Xing, Lei, et al. "Overview of image-guided radiation therapy." Medical Dosimetry 31.2 (2006): 91-112.

[2] Siewerdsen, Jeffrey H., et al. "The influence of antiscatter grids on soft-tissue detectability in cone-beam computed tomography with flat-panel detectors: Antiscatter grids in cone-beam CT." Medical physics 31.12 (2004): 3506-3520.

[3] Jarry, Geneviève, et al. "Characterization of scattered radiation in kV CBCT images using Monte Carlo simulations." Medical physics 33.11 (2006): 4320-4329.

[4] Li, Heng, Radhe Mohan, and X. Ronald Zhu. "Scatter kernel estimation with an edge-spread function method for cone-beam computed tomography imaging." Physics in Medicine & Biology 53.23 (2008): 6729.

[5] Ning, Ruola, Xiangyang Tang, and David Conover. "X-ray scatter correction algorithm for cone beam CT imaging." Medical physics 31.5 (2004): 1195-1202.

[6] Siewerdsen, J. H., et al. "A simple, direct method for x-ray scatter estimation and correction in digital radiography and cone-beam CT." Medical physics 33.1 (2006): 187-197.

[7] Zhu, Lei, N. Robert Bennett, and Rebecca Fahrig. "Scatter correction method for X-ray CT using primary modulation: Theory and preliminary results." IEEE transactions on medical imaging 25.12 (2006): 1573-1587.

[8] Zhu, Lei, et al. "A patient set-up protocol based on partially blocked cone-beam CT." Technology in cancer research & treatment 9.2 (2010): 191-198.

[9] Yan, Hao, et al. "Projection correlation based view interpolation for cone beam CT: primary fluence restoration in scatter measurement with a moving beam stop array." Physics in Medicine & Biology 55.21 (2010): 6353.

[10] Wang, Jing, Weihua Mao, and Timothy Solberg. "Scatter correction for cone-beam computed tomography using moving blocker strips: A preliminary study." Medical physics 37.11 (2010): 5792-5800.

[11] Ouyang, Luo, Kwang Song, and Jing Wang. "A moving blocker system for cone-beam computed tomography scatter correction." Medical physics 40.7 (2013).

[12] Li, Tianfang, et al. "Four- dimensional cone- beam computed tomography using an on- board imager." Medical physics 33.10 (2006): 3825-3833.

[13] Sonke, Jan- Jakob, et al. "Respiratory correlated cone beam CT." Medical physics 32.4 (2005): 1176-1186.

[14] Bergner, Frank, et al. "Autoadaptive phase- correlated (AAPC) reconstruction for 4D CBCT." Medical physics 36.12 (2009): 5695-5706.

[15] Amer, A., et al. "Imaging doses from the Elekta Synergy X-ray cone beam CT system." *The British journal of radiology*80.954 (2007): 476-482.

[16] Feldkamp, L. A., L. C. Davis, and J. W. Kress. "Practical cone-beam algorithm." JOSA A 1.6 (1984): 612-619.

[17] Andersen, Anders H., and Avinash C. Kak. "Simultaneous algebraic reconstruction technique (SART): a superior implementation of the ART algorithm." Ultrasonic imaging 6.1 (1984): 81-94.

[18] Solberg, T., et al. "Enhancement of 4D cone-beam computed tomography through constraint optimization." Proc of International Conference on the Use of Computers in Radiation Therapy. 2010.

[19] Song, Jiayu, et al. "Sparseness prior based iterative image reconstruction for retrospectively gated cardiac micro- CT." Medical physics 34.11 (2007): 4476-4483.

[20] Gu, Xuejun, et al. "Implementation and evaluation of various demons deformable image registration algorithms on a GPU." Physics in Medicine & Biology 55.1 (2009): 207.

[21] Wang, Jing, and Xuejun Gu. "Simultaneous motion estimation and image reconstruction (SMEIR) for 4D cone- beam CT." Medical physics 40.10 (2013).

[22] Chen, Guang- Hong, Jie Tang, and Shuai Leng. "Prior image constrained compressed sensing (PICCS): a method to accurately reconstruct dynamic CT images from highly undersampled projection data sets." Medical physics 35.2 (2008): 660-663.

[23] Leng, Shuai, et al. "Streaking artifacts reduction in four- dimensional cone- beam computed tomography." Medical physics 35.10 (2008): 4649-4659.

[24] Zheng, Ziyi, et al. "Fast 4D cone-beam reconstruction using the McKinnon-Bates algorithm with truncation correction and nonlinear filtering." Medical Imaging 2011: Physics of Medical Imaging. Vol. 7961. International Society for Optics and Photonics, 2011.

[25] Park, Justin C., et al. "Motion- map constrained image reconstruction (MCIR): Application to four- dimensional cone- beam computed tomography." Medical physics 40.12 (2013).

[26] Jia, Xun, et al. "Four- dimensional cone beam CT reconstruction and enhancement using a temporal nonlocal means method." Medical physics 39.9 (2012): 5592-5602.

[27] Yan, Hao, et al. "A hybrid reconstruction algorithm for fast and accurate 4D cone-beam CT imaging." Medical physics 41.7 (2014).

[28] Mory, Cyril, Guillaume Janssens, and Simon Rit. "Motion-aware temporal regularization for improved 4D cone-beam computed tomography." Physics in Medicine & Biology 61.18 (2016): 6856.

[29] Han, Hao, Hao Gao, and Lei Xing. "Low-dose 4D cone-beam CT via joint spatiotemporal regularization of tensor framelet and nonlocal total variation." Physics in Medicine & Biology62.16 (2017): 6408.

[30] Zhang, Hua, Matthijs Kruis, and Jan-Jakob Sonke. "Directional sinogram interpolation for motion weighted 4D cone-beam CT reconstruction." Physics in Medicine & Biology 62.6 (2017): 2254.

[31] Yang, Yong, et al. "Evaluation of on-board kV cone beam CT (CBCT)-based dose calculation." Physics in Medicine & Biology 52.3 (2007): 685.

[32] Yoo, Sua, and Fang-Fang Yin. "Dosimetric feasibility of cone-beam CT-based treatment planning compared to CT-based treatment planning." International Journal of Radiation Oncology* Biology* Physics 66.5 (2006): 1553-1561.

[33] van Zijtveld, Mathilda, Maarten Dirkx, and Ben Heijmen. "Correction of conebeam CT values using a planning CT for derivation of the "dose of the day"." Radiotherapy and Oncology 85.2 (2007): 195-200.

[34] Siewerdsen, Jeffrey H., and David A. Jaffray. "Cone- beam computed tomography with a flat- panel imager: Magnitude and effects of x- ray scatter." Medical physics 28.2 (2001): 220-231.

[35] Neitzel, Ulrich. "Grids or air gaps for scatter reduction in digital radiography: a model calculation." Medical physics 19.2 (1992): 475-481.

[36] Sorenson, James A., and Jacqueline Floch. "Scatter rejection by air gaps: an empirical model." Medical physics 12.3 (1985): 308-316.

[37] Persliden, Jan, and Gudrun Alm Carlsson. "Scatter rejection by air gaps in diagnostic radiology. Calculations using a Monte Carlo collision density method and consideration of molecular interference in coherent scattering." Physics in Medicine & Biology 42.1 (1997): 155.

[38] Endo, Masahiro, et al. "Effect of scattered radiation on image noise in cone beam CT." Medical physics 28.4 (2001): 469-474.

[39] Wiegert, Jens, et al. "Performance of standard fluoroscopy antiscatter grids in flat-detector-based cone-beam CT." Medical Imaging 2004: Physics of Medical Imaging. Vol. 5368. International Society for Optics and Photonics, 2004.

[40] Boone, John M., and J. Anthony Seibert. "Monte Carlo simulation of the scattered radiation distribution in diagnostic radiology." Medical physics 15.5 (1988): 713-720.

[41] Malušek, Alexandr, et al. "Effect of scatter on reconstructed image quality in cone beam computed tomography: evaluation of a scatter-reduction optimisation function." Radiation protection dosimetry 114.1-3 (2005): 337-340.

[42] Mainegra-Hing, Ernesto, and Iwan Kawrakow. "Variance reduction techniques for fast Monte Carlo CBCT scatter correction calculations." Physics in Medicine & Biology 55.16 (2010): 4495.

[43] Zbijewski, Wojciech, and Freek J. Beekman. "Efficient Monte Carlo based scatter artifact reduction in cone-beam micro-CT." IEEE transactions on medical imaging 25.7 (2006): 817-827.

[44] Spies, L., et al. "Direct measurement and analytical modeling of scatter in portal imaging." Medical physics 27.3 (2000): 462-471.

[45] Rinkel, J., et al. "A new method for x-ray scatter correction: first assessment on a cone-beam CT experimental setup." Physics in Medicine & Biology 52.15 (2007): 4633.

[46] Sun, M., and J. M. Star-Lack. "Improved scatter correction using adaptive scatter kernel superposition." Physics in Medicine & Biology 55.22 (2010): 6695.

[47] Boone, John M., and J. Anthony Seibert. "An analytical model of the scattered radiation distribution in diagnostic radiology." Medical physics 15.5 (1988): 721-725.

[48] Seibert, J. A., and J. M. Boone. "X- ray scatter removal by deconvolution." Medical physics 15.4 (1988): 567-575.

[49] Niu, Tianye, and Lei Zhu. "Scatter correction for full- fan volumetric CT using a stationary beam blocker in a single full scan." Medical physics 38.11 (2011): 6027-6038.

[50] Suri, Roland E., et al. "Comparison of scatter correction methods for CBCT." Medical Imaging 2006: Physics of Medical Imaging. Vol. 6142. International Society for Optics and Photonics, 2006.

[51] Star-Lack, Josh, et al. "Efficient scatter correction using asymmetric kernels." Medical Imaging 2009: Physics of Medical Imaging. Vol. 7258. International Society for Optics and Photonics, 2009.

[52] Liu, Xinming, et al. "An accurate scatter measurement and correction technique for cone beam breast CT imaging using scanning sampled measurement (SSM) technique." Medical Imaging 2006: Physics of Medical Imaging. Vol. 6142. International Society for Optics and Photonics, 2006.

[53] Zhu, Lei, Norbert Strobel, and Rebecca Fahrig. "X-ray scatter correction for cone-beam CT using moving blocker array." Medical Imaging 2005: Physics of Medical Imaging. Vol. 5745. International Society for Optics and Photonics, 2005.

[54] Zhu, Lei, et al. "Scatter correction for cone- beam CT in radiation therapy." Medical physics 36.6Part1 (2009): 2258-2268.

[55] Jin, Jian- Yue, et al. "Combining scatter reduction and correction to improve image quality in cone- beam computed tomography (CBCT)." Medical physics 37.11 (2010): 5634-5644.

[56] Ning, Ruola, Xiangyang Tang, and David L. Conover. "X-ray scatter suppression algorithm for cone-beam volume CT." Medical Imaging 2002: Physics of Medical Imaging. Vol. 4682. International Society for Optics and Photonics, 2002.

[57] Rührnschopf, Ernst- Peter, and Klaus Klingenbeck. "A general framework and review of scatter correction methods in x- ray cone- beam computerized tomography. Part 1: Scatter compensation approaches." Medical physics 38.7 (2011): 4296-4311.

[58] Klingenbeck, Klaus. "A general framework and review of scatter correction methods in cone beam CT. Part 2: scatter estimation approaches." Medical physics 38.9 (2011): 5186-5199.

[59] Ritschl, Ludwig, et al. "Robust primary modulation- based scatter estimation for cone- beam CT." Medical physics 42.1 (2015): 469-478.

[60] Gao, Hewei, Lei Zhu, and Rebecca Fahrig. "Modulator design for x- ray scatter correction using primary modulation: Material selection." Medical physics 37.8 (2010): 4029-4037.

[61] Sidky, Emil Y., and Xiaochuan Pan. "Image reconstruction in circular cone-beam computed tomography by constrained, total-variation minimization." Physics in Medicine & Biology53.17 (2008): 4777.

[62] Candès, Emmanuel J., Justin Romberg, and Terence Tao. "Robust uncertainty principles: Exact signal reconstruction from highly incomplete frequency information." IEEE Transactions on information theory 52.2 (2006): 489-509.

[63] Siddon, Robert L. "Fast calculation of the exact radiological path for a three-dimensional CT array." Medical physics 12.2 (1985): 252-255.

[64] Yu, Hengyong, and Ge Wang. "Compressed sensing based interior tomography." Physics in medicine & biology 54.9 (2009): 2791.

[65] Standard, I. S. O. "Photography-Electronic still-picture cameras-Resolution measurements." (2000).

[66] Masaoka, Kenichiro, et al. "Modified slanted-edge method and multidirectional modulation transfer function estimation." Optics express 22.5 (2014): 6040-6046.

[67] Lazos, Dimitrios, and Jeffrey F. Williamson. "Impact of flat panel- imager veiling glare on scatter- estimation accuracy and image quality of a commercial on- board cone- beam CT imaging system." Medical physics 39.9 (2012): 5639-5651.

[68] Masaoka, Kenichiro, et al. "Modified slanted-edge method and multidirectional modulation transfer function estimation." *Optics express* 22.5 (2014): 6040-6046.

[69] Dong, Xue, et al. "Relationship between x- ray illumination field size and flat field intensity and its impacts on x- ray imaging." Medical physics 39.10 (2012): 5901-5909.

[70] Kimme- Smith, Carolyn, Lawrence W. Bassett, and Richard H. Gold. "Focal spot size measurements with pinhole and slit for microfocus mammography units." Medical physics 15.3 (1988): 298-303.

[71] Russo, Paolo, and Giovanni Mettivier. "Method for measuring the focal spot size of an x- ray tube using a coded aperture mask and a digital detector." Medical physics 38.4 (2011): 2099-2115.

[72] Richardson, William Hadley. "Bayesian-based iterative method of image restoration." JOSA 62.1 (1972): 55-59.

[73] Lucy, Leon B. "An iterative technique for the rectification of observed distributions." The astronomical journal 79 (1974): 745.

[74] Dey, Nicolas, et al. "Richardson–Lucy algorithm with total variation regularization for 3D confocal microscope deconvolution." Microscopy research and technique 69.4 (2006): 260-266.

[75] Laasmaa, Martin, Marko Vendelin, and Pearu Peterson. "Application of regularized Richardson–Lucy algorithm for deconvolution of confocal microscopy images." Journal of microscopy 243.2 (2011): 124-140.

[76] Lee, Ho, et al. "Scatter correction in cone- beam CT via a half beam blocker technique allowing simultaneous acquisition of scatter and image information." Medical physics 39.5 (2012): 2386-2395.

[77] Chan, Heang- Ping, and Yoshiharu Higashida. "Performance of antiscatter grids in diagnostic radiology: experimental measurements and Monte Carlo simulation studies." Medical physics 12.4 (1985): 449-454.

[78] Kyriakou, Yiannis, and Willi Kalender. "Efficiency of antiscatter grids for flat-detector CT." Physics in Medicine & Biology 52.20 (2007): 6275.

[79] Kyriakou, Yiannis, Thomas Riedel, and Willi A. Kalender. "Combining deterministic and Monte Carlo calculations for fast estimation of scatter intensities in CT." Physics in Medicine & Biology 51.18 (2006): 4567.

[80] Zhu, Lei, Jing Wang, and Lei Xing. "Noise suppression in scatter correction for cone- beam CT." Medical physics 36.3 (2009): 741-752.

[81] Zhao, Wei, et al. "A patient-specific scatter artifacts correction method." Medical Imaging 2014: Physics of Medical Imaging. Vol. 9033. International Society for Optics and Photonics, 2014.

[82] Dong, Xue, et al. "Low-dose and scatter-free cone-beam CT imaging using a stationary beam blocker in a single scan: phantom studies." Computational and mathematical methods in medicine 2013 (2013).

[83] Lee, Ho, Benjamin P. Fahimian, and Lei Xing. "Binary moving-blocker-based scatter correction in cone-beam computed tomography with width-truncated projections: proof of concept." Physics in Medicine & Biology 62.6 (2017): 2176.

[84] Xu, Yuan, et al. "A practical cone-beam CT scatter correction method with optimized Monte Carlo simulations for image-guided radiation therapy." Physics in Medicine & Biology 60.9 (2015): 3567.

[85] Zhao, Cong, et al. "Blind deconvolution for blocker-based scatter correction of CBCT." Nuclear Science Symposium and Medical Imaging Conference (NSS/MIC), 2015 IEEE. IEEE, 2015.

[86] Fletcher, Reeves, and Colin M. Reeves. "Function minimization by conjugate gradients." The computer journal7.2 (1964): 149-154.

[87] Sidky, Emil Y., Chien-Min Kao, and Xiaochuan Pan. "Accurate image reconstruction from few-views and limited-angle data in divergent-beam CT." Journal of X-ray Science and Technology14.2 (2006): 119-139.

[88] Lustig, Michael, David Donoho, and John M. Pauly. "Sparse MRI: The application of compressed sensing for rapid MR imaging." Magnetic Resonance in Medicine: An Official Journal of the International Society for Magnetic Resonance in Medicine 58.6 (2007): 1182-1195.

[89] Jia, Xun, et al. "GPU-based fast low-dose cone beam CT reconstruction via total variation." Journal of X-ray science and technology 19.2 (2011): 139-154.

[90] Chen, Xi, et al. "Optimization of the geometry and speed of a moving blocker system for cone- beam computed tomography scatter correction." Medical physics 44.9 (2017).

[91] Star- Lack, J., et al. "SU- FF- I- 04: A fast variable- intensity ring suppression algorithm." Medical Physics 33.6Part2 (2006): 1997-1997.

[92] Brenner, David J., and Eric J. Hall. "Computed tomography—an increasing source of radiation exposure." New England Journal of Medicine 357.22 (2007): 2277-2284.

[93] Kalender, Willi A. "Dose in x-ray computed tomography." Physics in Medicine & Biology 59.3 (2014): R129.

[94] Yu, Lifeng, et al. "Radiation dose reduction in computed tomography: techniques and future perspective." Imaging in medicine 1.1 (2009): 65.

[95] McCollough, Cynthia H., et al. "Strategies for reducing radiation dose in CT." Radiologic Clinics 47.1 (2009): 27-40.

[96] Hsieh, Jiang. "Computed tomography: principles, design, artifacts, and recent advances." Bellingham, WA: SPIE, 2009.

[97] Zhao, Cong, et al. "Robust moving-blocker scatter correction for cone-beam computed tomography using multiple-view information." PloS one 12.12 (2017): e0189620.

[98] Ren, Lei, et al. "Feasibility study of a synchronized- moving- grid (SMOG) system to improve image quality in cone- beam computed tomography (CBCT)." Medical physics 39.8 (2012): 5099-5110.

[99] Keall, Paul J., et al. "The management of respiratory motion in radiation oncology report of AAPM Task Group 76 a." Medical physics 33.10 (2006): 3874-3900.

[100] Pretorius, P., Karen Johnson, and Michael King. "Respiratory motion compensation in Tc-99m cardiac perfusion SPECT/CT stress acquisitions: Experience from 150+ patients." Journal of Nuclear Medicine 55.supplement 1 (2014): 149-149.

[101] Kriminski, Sergey, et al. "Respiratory correlated cone-beam computed tomography on an isocentric C-arm." Physics in Medicine & Biology 50.22 (2005): 5263.

[102] Lu, Jun, et al. "Four- dimensional cone beam CT with adaptive gantry rotation and adaptive data sampling." Medical physics34.9 (2007): 3520-3529.

[103] Blume, Moritz, et al. "Joint reconstruction of image and motion in gated positron emission tomography." IEEE transactions on medical imaging 29.11 (2010): 1892-1906.

[104] Gilland, David R., et al. "Simultaneous reconstruction and motion estimation for gated cardiac ECT." IEEE Transactions on nuclear science 49.5 (2002): 2344-2349.

[105] Gravier, Erwan, et al. "Fully 4D motion-compensated reconstruction of cardiac SPECT images." Physics in Medicine & Biology 51.18 (2006): 4603.

[106] Jacobson, Matthew W., and Jeffrey A. Fessler. "Joint estimation of respiratory motion and activity in 4D PET using CT side information." (2006).

[107] Jin, Mingwu, et al. "A quantitative evaluation study of four-dimensional gated cardiac SPECT reconstruction." Physics in Medicine & Biology 54.18 (2009): 5643.

[108] Li, Ruijiang, et al. "Real- time volumetric image reconstruction and 3D tumor localization based on a single x- ray projection image for lung cancer radiotherapy." Medical physics37.6Part1 (2010): 2822-2826.

[109] Li, Tianfang, Albert Koong, and Lei Xing. "Enhanced 4D cone- beam CT with inter-phase motion model." Medical physics34.9 (2007): 3688-3695.

[110] Li, Tianfang, et al. "Model- based image reconstruction for four- dimensional PET." Medical physics 33.5 (2006): 1288-1298.

[111] Qiao, Feng, et al. "A motion-incorporated reconstruction method for gated PET studies." Physics in Medicine & Biology51.15 (2006): 3769.

[112] Rit, Simon, et al. "On- the- fly motion- compensated cone- beam CT using an a priori model of the respiratory motion." Medical physics 36.6Part1 (2009): 2283-2296.

[113] Staub, David, et al. "4D Cone- beam CT reconstruction using a motion model based on principal component analysis." Medical physics 38.12 (2011): 6697-6709.

[114] Zhang, Qinghui, et al. "Correction of motion artifacts in cone- beam CT using a patient- specific respiratory motion model." Medical physics 37.6Part1 (2010): 2901-2909.

[115] Tang, Qiulin, et al. "A fully four- dimensional, iterative motion estimation and compensation method for cardiac CT." Medical physics 39.7Part1 (2012): 4291-4305.

[116] Taguchi, Katsuyuki, and Hiroyuki Kudo. "Motion compensated fan-beam reconstruction for nonrigid transformation." IEEE transactions on medical imaging 27.7 (2008): 907-917.

[117] Gao, Hao, et al. "4D cone beam CT via spatiotemporal tensor framelet." Medical physics 39.11 (2012): 6943-6946.

[118] Segars, W. Paul, et al. "Extension of the 4D NCAT phantom to dynamic x-ray CT simulation." Nuclear Science Symposium Conference Record, 2003 IEEE. Vol. 5. IEEE, 2003.

[119] Segars, W. Paul, and Benjamin MW Tsui. "Study of the efficacy of respiratory gating in myocardial SPECT using the new 4-D NCAT phantom." IEEE Transactions on Nuclear Science 49.3 (2002): 675-679.

[120] Wang, Jing, et al. "Penalized weighted least-squares approach to sinogram noise reduction and image reconstruction for low-dose X-ray computed tomography." IEEE transactions on medical imaging 25.10 (2006): 1272-1283.

[121] Wang, Zhou, et al. "Image quality assessment: from error visibility to structural similarity." IEEE transactions on image processing 13.4 (2004): 600-612.

[122] Zhu, Lei. "Local filtration based scatter correction for cone- beam CT using primary modulation." Medical physics 43.11 (2016): 6199-6209.

[123] Muckley, M., et al. "Regularizer Performance for SparseCT Image Reconstruction With Practical Subsampling." Fully3D, Xi'an, China (2017).

[124] Koesters, Thomas, et al. "SparseCT: interrupted-beam acquisition and sparse reconstruction for radiation dose reduction." Medical Imaging 2017: Physics of Medical Imaging. Vol. 10132. International Society for Optics and Photonics, 2017.

[125] Siewerdsen, J. H., and D. A. Jaffray. "Cone- beam computed tomography with a flat- panel imager: Effects of image lag." Medical physics 26.12 (1999): 2635-2647.

[126] Huang, Jing, et al. "Iterative image reconstruction for sparse-view CT using normal-dose image induced total variation prior." PloS one 8.11 (2013): e79709.

[127] Niu, Shanzhou, et al. "Sparse-view x-ray CT reconstruction via total generalized variation regularization." Physics in Medicine & Biology 59.12 (2014): 2997.

[128] Liu, Yan, et al. "Total variation-stokes strategy for sparse-view X-ray CT image reconstruction." IEEE Trans. Med. Imaging33.3 (2014): 749-763.

[129] Yu, Wei, and Li Zeng. "ℓ0 gradient minimization based image reconstruction for limited-angle computed tomography." PloS one 10.7 (2015): e0130793.

[130] Zhang, Hao, et al. "Texture-preserving Bayesian image reconstruction for low-dose CT." Medical Imaging 2016: Physics of Medical Imaging. Vol. 9783. International Society for Optics and Photonics, 2016.

Biographical Information

Cong Zhao received his Bachelor of Science degree in Electric Science and Technology at the Huazhong University of Science and Technology, China in 2013. He received his Master of Science degree in Physics at The University of Texas at Arlington in 2015. After that, he continues working towards his Doctor of Philosophy degree under the advisement of Dr. Mingwu Jin.

His major research contribution is the development of robust scatter correction methods and novel 4D reconstruction methods for cone-beam computed tomography (CBCT) to achieve the high image quality with reduced radiation dose. He also has first author publications in PLOS One and Physics in Medicine and Biology. He has presented his research both nationally, at the AAPM Annual Meetings, and internationally, at the IEEE Nuclear Science Symposium and Medical Imaging conference.